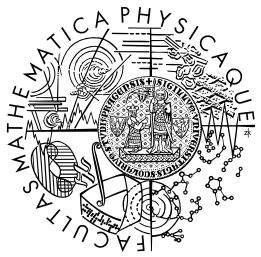

FACULTY
OF MATHEMATICS
AND PHYSICS
Charles University

MASTER THESIS

Alžběta Oplištilová

Spectroscopic and photometric investigation of selected hot stars

Astronomical Institute of Charles University

Supervisor of the master thesis: prof. RNDr. Petr Harmanec, DrSc.

Study programme: Physics

Study branch: Astronomy and Astrophysics

Prague 2021

I declare that I carried out this master thesis independently, and only with the cited sources, literature and other professional sources. It has not been used to obtain another or the same degree.

I understand that my work relates to the rights and obligations under the Act No. 121/2000 Sb., the Copyright Act, as amended, in particular the fact that the Charles University has the right to conclude a license agreement on the use of this work as a school work pursuant to Section 60 subsection 1 of the Copyright Act.

In ..... date ....

Author's signature

I would like to thank, first and foremost, my supervisor, prof. RNDr. Petr Harmanec, DrSc. I am really grateful for his help, comments, suggestions, patience, and support. My special thanks go to dr. Hrvoje Božić, dipl. ing. for giving guidance to me at Hvar Observatory and providing light curves. I also thank Drs. Thomas Rivinius and Dietrich Baade for providing reach data sets from CES, HEROS, and FEROS, to BRITE Team for providing BRITE data, to Drs. Herbert Pablo and Andrzej Pigulski, who carried the initial reduction of BRITE data, to observers from Ondřejov Observatory for measuring spectra, and to Dr. Coralie Neiner, who offered me to use the Narval and Espadons series of spectra. I am grateful to authors whose useful programs I used – Juraj Jonák (`dynspec`), Petr Hadrava (`KOREL`), Adam Harmanec (`reSpefo`), Petr Harmanec (`hec` programs, `efem`), Jana Nemravová (`Pyterpol`), Andrej Prša and his team (`PHOEBE 1`). I also express my deep gratitude to my family that support me during my studies and to my friend who read some parts and pointed out language mistakes.

Title: Spectroscopic and photometric investigation of selected hot stars

Author: Alžběta Oplištilová

Institute: Astronomical Institute of Charles University

Supervisor: prof. RNDr. Petr Harmanec, DrSc., Astronomical Institute of Charles University

Abstract: To rigorously study hot stars, we need to determine their properties as accurately as possible. This thesis focuses on improving the accuracy of parameters of two hot stars and contributes to the collection of stars with more known parameters. While photometric and spectroscopic data sets on hot stars δ Ori A and ω CMa are plentiful, the former is a triple star that suffers from having a faint spectrum of the secondary, which complicates its analysis, and the latter is a Be star, the origin, formation, and long-term variability of whose gaseous envelopes (veils) remain unexplained. Using mathematical techniques (Fourier transforms) and modelling software `PHOEBE 1`, properties of δ Ori A are determined, and conjecture on the presence of a circumstellar envelope in δ Ori A might be true by considering the shape changes of the H_α line. A conjecture that period changes of ω CMa correlate to the mass of the circumstellar envelopes seems to be proved true by considering variations of radial velocities, V/R ratio, and determining profile line asymmetry.

Keywords: massive hot stars - Be stars - timescales of variations

Contents

Introduction

Hot stars of the main sequence are very massive, and therefore live for only a relatively short time (about 10^6–10^7 years on the main sequence), but their influence on the universe outlasts their lives. First, their relatively rapid nuclear reactions in their interiors produce the chemical elements up to iron; they are the most important contributors (through stellar winds and supernova explosions) to the interstellar concentration of these elements. Understanding the evolution of hot stars may help us to understand the chemical composition of galaxies. Second, their evolution usually ends as core-collapse supernovae, powerful and incredibly luminous events in the universe, giving birth to neutron stars and black holes.

According to several researches, for instance, Abt [1983], Raghavan et al. [2010], Duchêne and Kraus [2013], and Moe and Di Stefano [2017], the majority of hot stars originate in binary or even multiple systems. Why this should be the case still eludes explanation; understanding why hot stars are not usually born as single stars would represent a significant advance in the general theory of the origin of stars. Multiple star systems are very numerous, accounting for more than 50% of stars in our solar neighbourhood (within about 5 pc of the Sun) and 20% of all stars observable by optical as well as non-optical instruments. Hot stars, usually included in multiple systems, are also appropriate objects for accurate determination of stellar parameters. They help with the determination of properties of more intricate stars, meaning those for which the distance is not known reliably and are not a part of a detached, non-interacting binary system.

A special type of multiple star systems is eclipsing binaries, two stars orbiting around their common centre of gravity. They are particularly useful since firstly, the line of sight is favourably aligned with the orbital plane, and secondly, the motion of the components in a binary is governed by the basic principles of classical dynamics. These two facts reduce the determination of principal parameters to a tractable geometric and dynamical problem. This unique property makes eclipsing binaries the key calibrators of stellar properties and distance estimates. Such a convenient star system is, for instance, the multiple star system δ Ori A, which is one of the objects chosen to study.

There are only about 50 O-type binaries in the Milky Way and Magellanic Clouds, for which individual stellar characteristics have been established, as they are detached and non-interacting. Therefore, the evolution of O stars is little understood. The main open questions in massive star evolution are, for instance [Meynet et al., 2013]:

(i) why massive stars are usually born in multiple star systems, as mentioned above;

(ii) what is the origin of slowly rotating, non-evolved, nitrogen-rich stars;

(iii) what is the evolutionary status of α-Cygni variables (these stars should be red supergiant stars according to their pulsations properties);

(iv) a question concerning various supernova types which are the endpoint of the evolution of stars with initial masses between 18 and 30 $M_{\odot}$.

To understand the evolution of the most massive stars and the questions above, it is necessary to determine their stellar parameters. Unfortunately, the transfer of their mass to their companions at certain phases of their nuclear evolution may complicate their analyses. The best candidates for such an analysis are multiple systems with minimal mass loss, and δ Ori A is one of them.

The multiple star system δ Ori A has three components, one of which is a massive O star, which is rare due to its short lifetime. In this study, I will focus on the accurate determination of physical elements and estimation of their errors using spectroscopy and photometry. I have a large collection of red spectra for δ Ori A that might indicate a presence of circumstellar material around the star: this hypothesis can be tested by analysing the changes of the shapes of H_{α} lines to detect possible weak H_{α} emission associated with the primary.

The goals of a new study of δ Ori A are the following:

- advanced analyses of the system's physical properties using programs `KOREL` [Hadrava, 1995, 1997], `Pyterpol` [Nemravová et al., 2016], etc.;
- solving the inverse problem in `PHOEBE 1` [Prša and Zwitter, 2005];
- verifying the conjecture about the presence of circumstellar material around the star by analysing changes of shapes of H_{α} lines.

Among all hot stars, the Be stars present the most challenges. Be stars are of spectral class B exhibiting time-variable emission in the Balmer lines and also in some metallic lines. It is their statistically much higher rotational velocity that distinguishes Be stars from B stars. There is a general agreement that the Be stars' emission lines are formed in extended flattened envelopes around them. A convincing proof of this fact provided, for instance, Quirrenbach et al. [1997] by the infrared and optical interferometry of seven Be stars. The appearance and disappearance of these emission lines in the spectra of Be stars are known as the Be phenomenon.

The mechanism of such behaviour remains unknown in spite of the enormous effort of many investigators. Therefore, a detailed study of the variability of a Be star such as ω CMa could help find the physical cause for these flattened envelopes. Specifically for this star, it has been conjectured by Harmanec [1998]

that there are small cyclic changes in the period of 1.37 days, which correlate with the extent of the circumstellar envelopes that causes the presence of emission lines in the spectrum of this star. I will test this conjecture by measuring a rich series of spectra, studying the variation of radial velocities (RVs), the V/R ratio, the strength of H_α emission line, and determining the asymmetry of profile lines with the period of 1.37 days. If the conjecture is true, then the period of 1.37 days is related to a corotating structure in the inner parts of the envelope and any intrinsic changes in the exact value of the 1.37 days period depend on the presence or absence of the emission in the star's spectrum.

Regarding the Be star ω CMa, the objectives are:

- studying the variations of RVs, the V/R ratio, the strength of H_α emission line, and the determination of line profile asymmetry;
- verifying the conjecture that period changes of the star correlate to the extent of the circumstellar envelopes.

1. Hot stars

Hot stars, which can be found in the upper left corner of the Hertzsprung-Russell diagram (HRD), are characterised by effective temperature greater than 10 000 K; thus, their colour is blue. They are also very luminous, massive, and therefore, short-lived (they live on the order of millions or tens of million years on the main sequence), as the time that a star spends on the main sequence is inversely proportional to its mass. Since stars spend roughly 90% of their lives on the main sequence burning hydrogen into helium, we can extrapolate the time spent on the main sequence to the lifetime of the star. Massive stars are younger than less massive stars, which fuse their hydrogen into helium much more slowly. The following approximation quantifies this relationship of mass to lifetime:

$$\frac{t_{\mathrm{MS}}}{t_{\odot}} \approx \left(\frac{M}{\mathcal{M}_{\odot}}\right)^{-2.5}, \tag{1.1}$$

where t_{MS} stands for the time that a considered star spends on the main sequence; $t_{\odot}$, for the time that the Sun spends on the main sequence; M, for the mass of a considered star; and $\mathcal{M}_{\odot}$, for the mass of the Sun.

Historically, hot stars correspond to early stars and refer to O, B, and possibly A stars. These types should have been hotter than the Sun, and therefore, younger than the Sun. On the other hand, late stars (or cooler stars) should have been older and cooler, compared to the Sun. This classification is still used in spectroscopy, although there is no doubt that the evolution of stars happens in another way. The number of hot stars is less than the number of cooler ones, as HRD including stars near the Sun shows. The fact that massive stars constitute only a negligible fraction ($\approx 0.1\%$) of the stellar population of stars in Solar neighborhood was demonstrated also by Ledrew [2001]. Nevertheless, they play a key role in the evolution of the universe, since they provide the main source of UV radiation and heavy chemical elements.

We can find spectral lines He II, He I, H I, O III, C III, N III in specta of O main sequence stars. These are often defined by the presence of ionized helium He II. Their temperatures are usually higher than 30 000 K, their masses range from 15 $\mathcal{M}_{\odot}$ to more than 60 $\mathcal{M}_{\odot}$; thus they become supernovae in the end of their lives. Their radii include 6 $\mathcal{R}_{\odot}$ and may exceed 10 $\mathcal{R}_{\odot}$.

The most prominent spectral lines in spectra of main sequence B stars are He I and H I; also, O II, C II, N II, Fe III, and Mg II are present while the He II lines are missing. Their masses fall into the interval from 2.2 to 15 $\mathcal{M}_{\odot}$; therefore, they can end their lives either as supernovae ($M \geq 8\mathcal{M}_{\odot}$) or as white dwarf ($M \leq 8\mathcal{M}_{\odot}$). Their radii range from 2.1 to 6 $\mathcal{R}_{\odot}$, and their temperatures are between 9 400 K and 30 000 K [Harmanec and Brož, 2011].

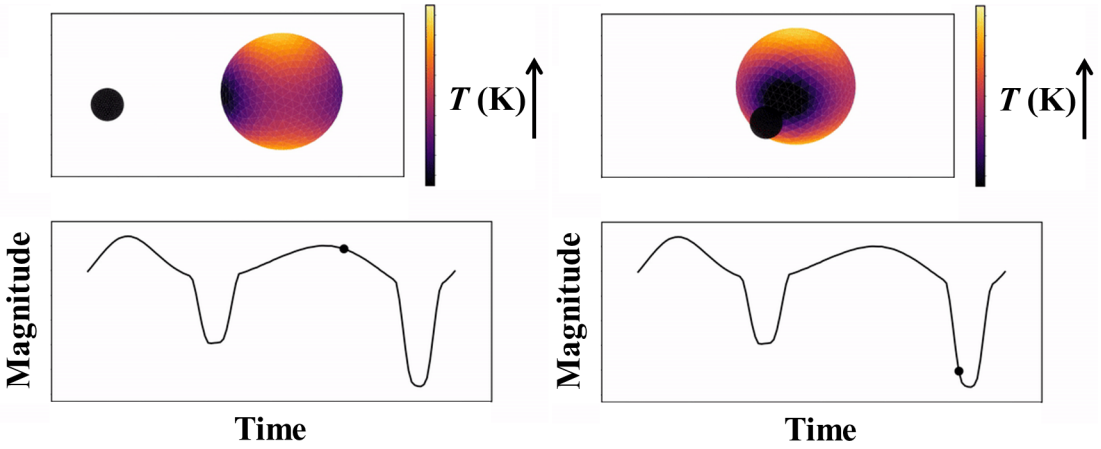

Figure 1.1: The signal coming to us from the eclipsing binaries demonstrated on the eclipsing binary δ Orionis. The distribution of the temperature on the surface is caused by eclipses and the non-spherical shape of the primary. The figure is based on the forward model from `PHOEBE 2`.

1.1 Multiple star systems and eclipsing binaries

The majority of hot stars originate as binaries or even multiple systems (a small number of stars that orbit each other, bound by gravitational attraction), as concluded, for instance, byAbt [1983], Raghavan et al. [2010], Duchêne and Kraus [2013], and Moe and Di Stefano [2017] in their studies. Their frequency of occurence offers a way to probe the star formation processes, since they offer the possibility of precise determination of their properties.

To understand stars, it is necessary to determine their properties as accurately as possible. Ideal objects to attain this objective are the mentioned multiple star systems, namely, eclipsing binaries, star systems consisting of two stars orbiting around their common centre of gravity. When the stars are eclipsing, the light signal coming to us is periodically dimmed, as you can see from Fig. 1.1.

For instance, to determine the mass of a star, we need to measure the gravitational interaction between that star and at least one another object. The only possibility in practice is to measure the interaction between the star of interest and its companion star. In the case of a star and a planet, we would reach an impasse because of the high luminosity of the star. Measuring the gravitational interaction between two galaxies is also impossible due to the large distances and time scales involved.

According to the observational method, we distinguish the following types of binaries:

- *Visual binaries*, which can be identified by eye and belong to the class of the

spatially-resolved binaries. Their angular distance in the sky is on the order of tenths arcseconds. If we assume the circular orbit and spherical shape of components, then visual binaries satisfy the following inequality:

$$\cos i < \frac{R_1 + R_2}{a}, \tag{1.2}$$

where i stands for inclination, R_1 and R_2 denote radii of components, and a is a major axis. Considering an eccentricity e, we can rewrite the inequality as

$$\cos i < \frac{(R_1 + R_2)(1 \pm e \sin \omega)}{a(1 - e^2)}, \tag{1.3}$$

where ω is an argument of periapsis.

- *Astrometric binaries*, which consist of the directly observable primary (the brighter component) and the secondary, the presence of which is evident only from periodic changes in its position in the sky caused by gravitational force.
- *Spectroscopic binaries*, which cannot be resolved by the present-day telescope – they look like a point source of light. The components of this type of binaries are identified in radial velocity (RV) changes due to orbital motion.
- *Eclipsing binaries*, which have an almost 90° inclination of their orbital axes, which means that an observer sees their periodic eclipses – regular variability of their brightness. This type of binary is the most useful because observers can gather information from both light curves (i.e., plots of flux against time) and RV curves, which together provide more information about the system than each type of curve by itself.

Roughly speaking, we can determine all fundamental parameters of a binary using various kinds of observations. Henry Norris Russell, an American astronomer, called this procedure the "royal road" of eclipsing binaries [Struve, 1957]:

> *"From immemorial antiquity, men have dreamed of a royal road to success – leading directly and easily to some goal that could be reached otherwise only by long approaches and with weary toil. [...] There is probably no better example of this than eclipses of the heavenly bodies."*
>
> *—Henry Norris Russell, 1946*

First, from RVs, one obtains $M_1 \sin^3(i)$, $M_2 \sin^3(i)$, i.e., minimal masses. From absolute astrometry one obtains the mass ratio. Adding photometry (light curves), one determines the system's geometry including inclination and determines the

radii of both components and masses from the known inclination and $M_1 \sin^3(i)$, $M_2 \sin^3(i)$. Then, from spectra or colour indices (meaning that measurements from more passbands are available), one obtains effective temperatures. Finally, with a known distance, extinction, and magnitude, one can figure out luminosities and all the remaining fundamental parameters of eclipsing binaries (the period, argument of periastron, inclination, eccentricity, etc.)

1.2 Be stars

Be stars are main-sequence stars of spectral type B (B-type stars) whose optical spectra include or have included at least one Balmer emission line. In examining successive spectra of Be stars secured over time intervals, we find that Balmer emission lines appear and disappear. This is called the *Be phenomenon*, and it might be caused by episodic ejections of mass into flattened circumstellar gaseous envelopes (veils) that exceed the radius of the star by at least ten times. Approximately 20% of B-type stars are Be stars. In young clusters, even 60–70% of B-type stars show the Be phenomenon.

The mechanism causing stellar materials to be ejected out of a Be star into its orbit is not fully understood, but is likely to be related to the star's rotational velocity. Most Be stars rotate very rapidly, velocities at their equators being probably quite close to their stability limit. Their much higher rotational velocity is an additional feature distinguishing Be stars from other B-type stars. Also, both ground-based spectroscopy [Rivinius et al., 1998] and space-based photometry [Baade et al., 2016] demonstrate that stellar pulsations are involved in the Be phenomenon. These observations of rotational velocities and stellar pulsation suggest that Be envelopes are a result of rotational instability, a radial outflow of matter via stellar wind facilitated by non-radial stellar pulsation, or mass transfer between binaries (see, e.g., Harmanec [1983c] and Rivinius et al. [2013]).

Be stars are the important source of ultraviolet photons and ionize the neighbourhood of stars as well as a vast circumstellar environment (in order of hundreds of parsecs). Thus, they heat the gas in the spiral arms of our galaxy.

1.2.1 Circumstellar envelope

A circumstellar envelope (or shell) is an approximately spherical part of a star outside the star's atmosphere. The material – usually formed from the dense stellar wind – is not gravitationally connected to the core of a star and much cooler than the star. The typical size of such an envelope is several times that of the stellar radius. The circumstellar envelope and the outer layers of the atmosphere differ in energy-momentum balance and geometry, despite there being no strict separation

between the two parts. Sometimes, a circumstellar envelope is present before the formation of a star.

The circumstellar envelopes of Be stars seem to be responsible for emission lines in the optical range of spectra. The envelope is present temporarily, which the emission lines indicate. They also alter the radial velocity variations.

1.2.2 Variations in time

Be stars are characterised by extreme spectral and photometric variabilities in time ranging from hours to decades. For the purposes of interpretation, variations in the spectra and brightness of a Be star are divided according to time scale into the following three groups [Harmanec, 1983b]:

- long-term variations (from years to decades),
- medium-term variations (from weeks to months),
- short-term variations (from tenths of days to a few days).

Long-term variations

Of all variations one sees in Be stars, it is the long-term spectral variation (including the transient appearance of emission lines) that is the most pronounced. In quiescence phases without Balmer emission lines, the spectra are similar to the classical spectra of B-type stars. In phases of strong emissions, additional absorption lines known as *shell lines* appear. These lines originate in the circumstellar envelopes, and if we observe their radiation from the equator of the star, we usually find that the lines are double-peaked. The double-peak also appears if the star rotates and the absorption from an envelope is negligable. This happens because the envelopes rotate, and we observe radiation both from the part of the envelope that approaches us and from the part that recedes from us. The two peak intensities are denoted by V and R. The first peak is shifted to the violet optical range, the second to the red. To observe cyclic variations lasting a few years, we investigate the change of V/R, the ratio of peak intensities. These cycles are not periodic, in contrast to medium-term and short-term variations. Moreover, the amplitudes of variations vary in each cycle. On average, cycles take 7 years. As the ratio V/R changes, so does the RV measured in the wings of an emission line. The luminosity and colour of the star change as well.

The strength of Balmer emission lines and the brightness and colors of a star are either *positively correlated* or *inversly correlated* [Harmanec, 1983a, 1994, 2000]. In the former case, emission lines slowly appear, and the formation of a veil is followed by an increase in the luminosity of the star, which moves from the main

sequence to a supergiant star in colour diagram $U-B$ with respect to $B-V$. In other words, $B-V$ becomes redder and $U-B$ bluer. Briefly, the stronger the Balmer emission, the brighter the star appears to us. In the latter case, also known as inverse correlation, the formation of a veil is followed by a decrease in the star's luminosity, and the star moves along the main sequence to a cooler subclass in the colour diagram $U-B$ with respect to $B-V$. Both $U-B$ and $B-V$ get redder. Thus, in this case the stronger the Balmer emission, the fainter the star appears to us.

The correlation between Balmer emission lines and brightness for a given star is observed to be always positive or always inverse, across all emission phases. For example, a positive correlation has been observed for γ Cas [Pollmann, 2021], π Aqr [Nazé et al., 2017], ω CMa [Harmanec, 1998], and μ Cen [Rivinius et al., 1998], while an inverse correlation has been observed for 28 Tau [Tanaka et al., 2007], V1294 Aql [Ballereau and Chauville, 1989], TW Dra [Božić et al., 2013], and 88 Her [Kriz and Harmanec, 1975]. Hence, the existence of two types of correlation is a consequence of geometry. On the one hand, an inverse correlation arises for a star when we observe light from its equator as forming a cooler envelope that overshadows the star in our direction. On the other hand, if we observe the light from a star's pole, optically thick inner parts of an envelope make the star's radius larger from our view.

Medium-term variations

The temporary presence of a circumstellar envelope also accounts for medium-term variations of Be stars. Here, though, the envelope is weak; thus, the changes in spectra last only the order of weeks or months, their amplitudes are smaller, and the interval of shell lines is shorter. Non-periodic changes also belong to this group.

Because a secondary component has been found for so many systems with medium-term variations, it is usually considered that the cause of these variations is the binarity of the stars in question. Binarity also explains the periodic nature of the changes in RVs, the ratios V/R, the intensities of spectral lines, and the brightness of these stars. Sometimes, there are wild cases of long-term emission-style changes.

Short-term variations

Short-term variations of Be stars, those lasting from tenths of days to three days, are not easily interpretable. They have been studied only since the 1970s [Baade, 1982a, Balona et al., 1987, Percy et al., 1992]. The typical period of about one day causes a problem when making observations – it is not possible to observe

a complete change by a single instrument; these cycles are too long to be captured in one night but too short to be captured over successive nights.

On this timescale, changes are represented by asymmetries of spectral line profiles and by small spectral waves moving from the violet optical range to the red one. Importantly, changes in profiles are periodic or even multiperiodic. Changes of brightness are also usually periodic, and their periods are close to the rotational periods of the given Be star corresponding to the given Be star. Amplitudes of changes in brightness are less than 0.1 mag; they are often not visible at all. The light curves are not sinusoidal, and their amplitudes, as well as their shapes, constantly change. Even though the star is in a quiescence phase (no Balmer emission lines in a spectrum), short-term variations are still observable, in contrast to long-term and medium-term variations. The origin of these variations is not clear. There are two current interpretations: some researchers consider them a consequence of non-radial pulsations [Briot, 2004], while others think that they are a consequence of a corotating structure in the gas above the photosphere of a star.

1.3 Selected objects and the structure

This thesis focuses on two hot stars: Delta Orionis A and Omega Canis Majoris, multiple star system and Be star, respectively. The thesis is divided into two main parts. The first one deals with the eclipsing binary δ Ori A, while the second one with the Be star ω CMa. Both parts include basic information about the star, the theoretical background of used methods, data, analysis, and results. Throughout this thesis, I will use the abbreviated form for heliocentric Julian dates RJD = HJD-2400000.0.

2. Delta Orionis A

δ Ori A (Delta Orionis A, HD 36486, HIP 25930, HR 1852) is a triple-star subsystem of the multiple-star system Delta Orionis also called Mintaka (ADS 4134) in the constellation of Orion. It consists of six stars. A primary triple star system, δ Ori A ($V_{\mathrm{A}} = 2.23$ mag, $\alpha_{\mathrm{J2000}} = 5^{\mathrm{h}}32^{\mathrm{m}}00.40009^{\mathrm{s}}$, $\delta_{\mathrm{J2000}} = -00°17'56.7424''$), is gravitationally connected to δ Ori B ($V_{\mathrm{B}} = 14$ mag, $\alpha_{\mathrm{J2000}} = 5^{\mathrm{h}}31^{\mathrm{m}}58.745^{\mathrm{s}}$, $\delta_{\mathrm{J2000}} = -00°18'18.65''$), which is only known from spectroscopic measurements, and a binary system known as δ Ori C ($V_{\mathrm{C}} = 6.85$ mag, $\alpha_{\mathrm{J2000}} = 5^{\mathrm{h}}32^{\mathrm{m}}00.406^{\mathrm{s}}$, $\delta_{\mathrm{J2000}} = -00°17'04.38''$). The primary consists of an eclipsing binary Aa1 + Aa2 (V_{Aa1} = -5.4 mag, V_{Aa2} = -2.9 mag) with the orbital period of 5.732436 days with slightly eccentric orbit and a slow apsidal motion, and a distant tertiary called Ab (V_{Ab} = -4.2 mag) with an orbital period of several thousands of days (see Fig. 2.1). The summary of properties of δ Ori A is provided in Tab. 2.1. Fig. 2.2 depicts the position of the Delta Orionis on the sky.

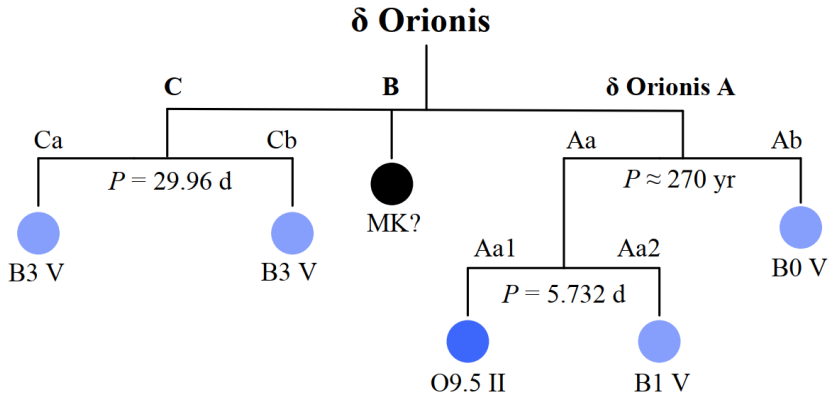

Figure 2.1: The structure of the multiple star system δ Orionis.

The object has been studied in by many researchers since the end of 19th century. From now on, the Aa1 stands for the primary; Aa2, for the secondary; and Ab, for the tertiary. Vogel and Scheiner [1892] determined the orbital period $P = (5.7325 \pm 0.0002)$ d; Koch and Hrivnak [1981] reached the acceptable masses $M_1 = 23\ \mathcal{M}_\odot$ and $M_2 = 9\ \mathcal{M}_\odot$; Harvey et al. [1987] obtained a sideral period of $P = (5.732403 \pm 0.0002)$ d, eccentricity $e = 0.087$, and amplitude $K = 100$ km/s. Harvin et al. [2002] carried out a tomographic separation of UV and optical spectra into two systems of spectral lines, interpreted as the lines of the primary and secondary of the eclipsing subsystem, and concluded that the components have unexpectedly low masses ($M_1 = 11.2\ \mathcal{M}_\odot$ and $M_2 = 5.6\ \mathcal{M}_\odot$). However, Mayer et al. [2010] pointed out that the second system of spectral lines in Harvin's study

belongs actually to the tertiary Ab. They concluded that the system has normal masses and estimated a mass ratio of 0.4. Harmanec et al. [2013] reported a similar mass ratio detecting the secondary in the He I 6678.151 Å line. The binary was studied in a series of four papers published by Corcoran et al. [2015], Nichols et al. [2015], Pablo et al. [2015] and Shenar et al. [2015].

I studied Delta Orionis A in my bachelor thesis [Oplištilová, 2019] and an account of the study was presented and then published in a conference contribution Oplištilová et al. [2020]. I disentangled the very week spectral lines of the secondary in the blue parts of the optical spectrum and derived mass ratio. Then, I used a light-curve solution based on photometry from artificial Earth satellites to obtain improved physical elements of the system. Finally, I analysed residuals between the theoretical model and observed light curves and found that these physical variations could be periodic, with a period of either ≈ 90 or 5.4 days.

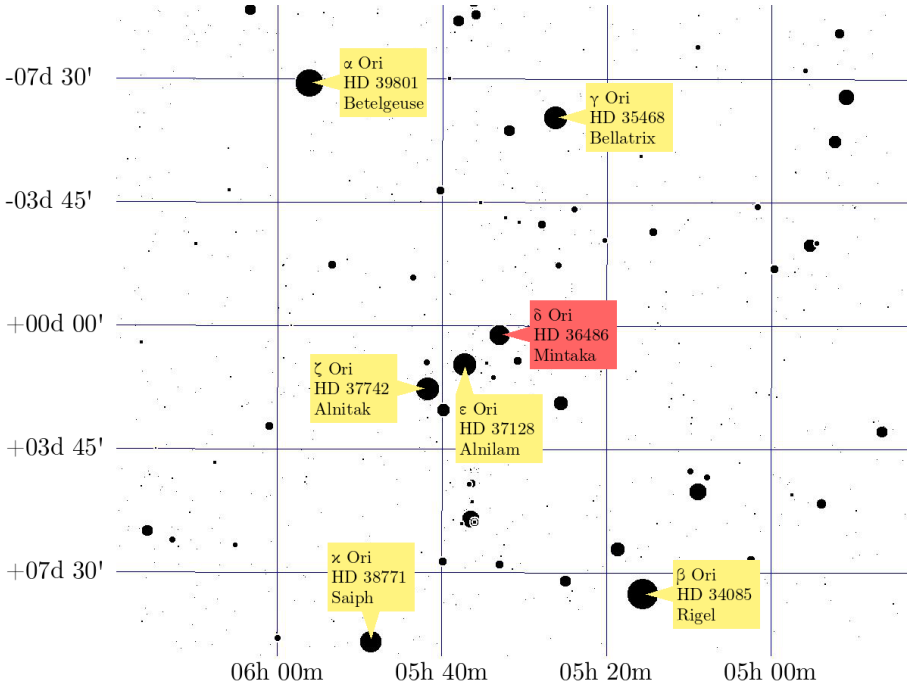

Figure 2.2: The star Delta Orionis in the constellation of Orion is marked by the red tag. The most famous stars from these constellations are labelled with yellow tag. There are proper names, Bayer designation (1603)[1], and Henry Draper Catalogue (1918–1924)[2] displayed in the figure. Source of the maps: TheSky (astronomy software)[3].

[1]Stars are identified by a lower-case Greek letter (or Latin letter) and by its parent constellation frequently abbreviated to three-letter form.
[2]Stars are denoted by HD and a number.
[3]Copyright© 1984–1996 by Software Bisque

Table 2.1: The summary of physical properties of δ Ori Aa from published studies.

Q	[1]		[2]		[3]	[4]			[5]
	PHOEBE LC, RV		PoWR analysis	Solution from LC and RV	CCF	Low mass model	Medium mass model	High mass model	KOREL PHOEBE LC, RV
	II	III							
$P_{\rm sidereal}$ [days]	5.732436* [Mayer et al., 2010] used in all cases								
$T_{\rm min}$ [RJD--54000]	1.966(4)	1.966(4)	2277.790(24)		3040.938				2691.23
e [ ]				0.1133(3)	0.1124*	0.1124	0.1124	0.113	0.07583
ω [°]	144.2(21)	140.0(18)		141.3(2)	144.2*	141.2119	141.43	141.0834	148.7(15)
$\dot{\omega}$ [°/d]				0.00397(10)					0.00422*
K_1 [km s^{-1}]					104.6(16)	96.02(60)	96.02(20)	96.02(60)	106.80
K_2 [km s^{-1}]					266(20)				250
a [$\mathcal{R}_\odot$]	44.2(3)	44.0(3)		43.1(17)	43.0(24)*	42.97	43.14	44.86	41.91(18)
i [°]	67.6(4)	73.6(3)		76.5(2)		76.39	77.23	76.74	78.1(3)
$T_{\rm ef_1}$ [kK]	30*	30*	29.5(5)	30*		30*	30*	30*	31.401
$T_{\rm ef_2}$ [kK]	24*	24*	25.6	24.1		24.149	24.039	23.835	25.442
Ω_1 [ ]	3.156	3.328(34)							2.9
Ω_2 [ ]	4.008(81)	5.065							2.5
$q = \frac{M_2}{M_1}$	0.4147	0.3962	0.35	0.35714	0.39056	0.35867	0.35331	0.33599	0.41549
M_1 [$\mathcal{M}_\odot$]	25*	25*	24	23.8	23.3(31)*	23.81	24.20	27.59	21.1
M_2 [$\mathcal{M}_\odot$]	10.4	9.91	8.4*	8.5	9.1(10)*	8.54	8.55	9.27	8.8
R_1 [$\mathcal{R}_\odot$]	16.8	15.6	16.5(9)	15.1		15.12	15.34	16.08	13.6
R_2 [$\mathcal{R}_\odot$]	7.0	4.8	6.5	5.0		5.00	4.92	5.17	3.7
V_γ [km s^{-1}]	21.77(51)	21.74(50)		15.5(7)	21.1(16)	15.51	15.71	15.34	21.96(33)

Remark: Numbers in brackets correspond to errors of last displayed digits.
* denotes fixed parameters in the given solution.

[1] Mayer et al. [2010]; [2] Corcoran et al. [2015]; [3] Richardson et al. [2015]; [4] Pablo et al. [2015]; [5] The results of this thesis.

2.1 The theoretical background

For the data analysis of δ Ori (solving the inverse problem), I used the following programs: `PHOEBE 1`[1] [Prša and Zwitter, 2005], `KOREL`[2] [Hadrava, 1995, 1997], `PYTERPOL`[3] [Nemravová et al., 2016], `reSPEFO2`[4] (written by Adam Harmanec), `HEC26`[5], `HEC27`[6], and `HEC35D`[7] (all three written by Petr Harmanec) and others.

2.1.1 Inverse problem

To rigorously study stars, we need to determine their properties as accurately as possible. Properties of stars are quantified by geometrical and physical parameters. Geometrical parameters include quantities expressing spatial arrangements such as inclination i, the major axis a, and the argument of periapsis ω, etc. Physical parameters provide intrinsic information about objects, for instance, their temperature T, mass M, and radius R. To determine stellar parameters and the uncertainties of their values due to measuring errors and sampling errors, we need to use several programs and mathematical procedures explained in this chapter.

We can obtain information about stars from the observational data. The most common kinds of data are the light curves and RV curves. The former is ordered pairs of observed magnitudes and the corresponding times of observations. The latter are components' RVs as a function of time reduced to the barycentre of the solar system.

To represent what a star at an enormous distance from us looks like, we use a model consisting of many equations, ranging from basic ones such as Kepler's Third Law to advanced formulae such as Einstein's field equations and equations describing the stellar structure. This model also includes more than 100 geometrical and physical parameters. One convenient tool for constructing a model of a star is the well tested modelling software `PHOEBE 1`.

The task of the model is to use the input parameters and compute a theoretical curve. This is referred to as the forward (direct) problem: given the set of parameters, the theoretical curves (light curves in requested passbands, RV curves, spectral line profiles, etc.) are uniquely determined.

Nevertheless, in practice, we need to do the exact opposite. Given the observed data, we need to determine the set of parameters for which the model yields the

[1] http://phoebe-project.org/
[2] http://www.asu.cas.cz/ had/korel.html
[3] https://github.com/chrysante87/pyterpol/wiki
[4] https://astro.troja.mff.cuni.cz/projects/respefo/
[5] https://astro.troja.mff.cuni.cz/ftp/hec/HEC26/
[6] https://astro.troja.mff.cuni.cz/ftp/hec/HEC27/
[7] http://astro.troja.mff.cuni.cz/hec/HEC35

best match of the observed curves. This is called the inverse problem. As opposed to the direct problem, due to data noise and parameter correlation, many combinations of parameters yield indistinguishable theoretical curves within a given accuracy. That means the inverse problem may not have a unique solution, and the right combination of the wrong parameters may fit the observed data exceptionally well (see Fig. 2.3). The difficulty lies in the complexity of the parameter space. The solution may end in a local minimum instead of the global one and is influenced by the choice of parametrization and parameter correlations. To solve the inverse problem, fitting methods are used.

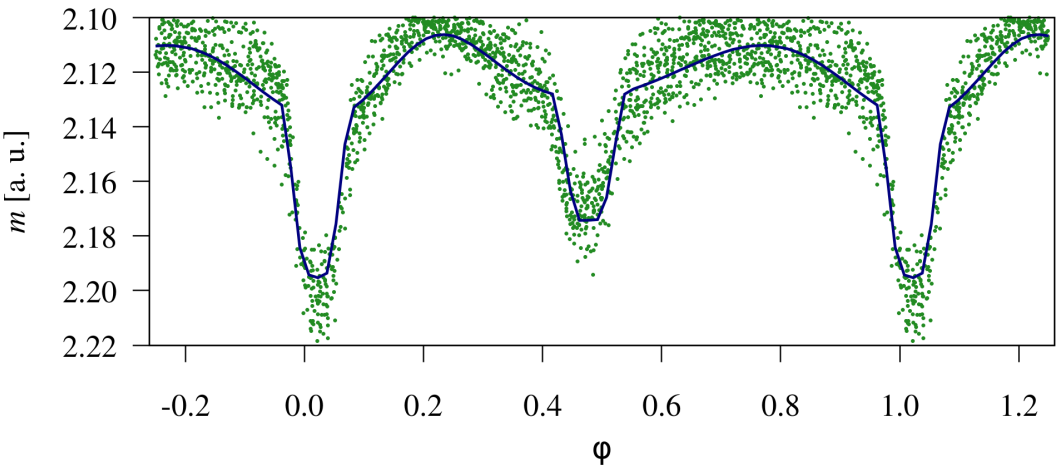

Figure 2.3: Solution to an inverse problem that is not unique.

2.1.2 Determining parameters of stars in PHOEBE

The properties of each binary component and their mutal orbit are characterised by many quantities: parameters or elements. There are 34 parameters in `PHOEBE 1`. The principle of them are, for instance: semi-major axis a, eccentricity e, argument of pericentre ω, rotational parameters F_1 and F_2, phase shift φ, γ velocity, inclination i, exponents of the gravitational limb darkening g_1, g_2, surface temperatures T_1, T_2, bolometric albedos, surface potentials, mass ratio q, reference epoch, time change of the period, rate of apsidal advance, and limb darkening. Some of them are shown in Figs. 2.4 and 2.5).

2.1.3 PHOEBE

`PHOEBE 1`, also called legacy, (PHysics Of Eclipsing BinariEs) is the Eclipsing Binary Modeling Software developed by Prša and Zwitter [2005]. It is based on

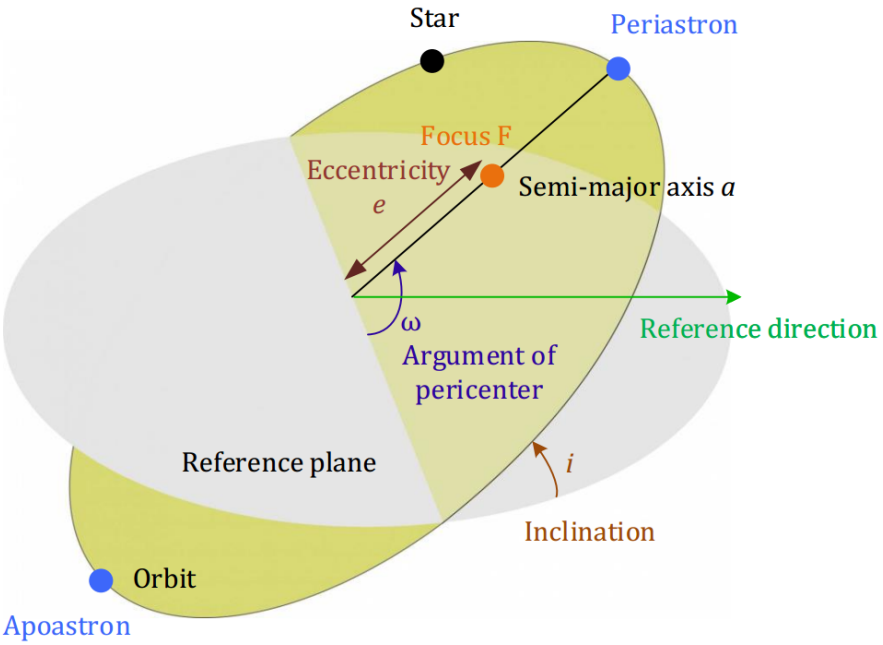

Figure 2.4: The main parameters.

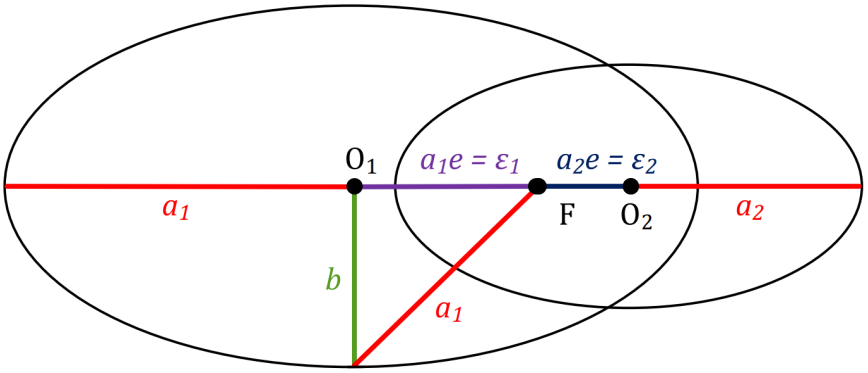

Figure 2.5: The geometrical parameters of a binary system.

Wilson-Devinney binary star modeling program (WD)[8] from 1971 written in FORTRAN as the core of `PHOEBE` and add manually anything needed beyond the core. Wilson's and Deviney's program is well tested, debugged, free, still under develop-

[8]Other alternatives for eclipsing binary modeling programs are, for instance, `FOTEL` [Hadrava, 1990, 2004], `JKTEBOP` [Southworth, 2012], `EBOP` [Nelson and Davis, 1972, Etzel, 1981], `LIGHT2` [Hill and Rucinski, 1993], `ellc` [Maxted, 2016], `Nightfall` [Wichmann, 1998], `WINK` [Wood, 1971], and `WUMA` [Ruciński, 1973]

ment, extremely fast, efficient, and the authors are responsive. On the other hand, the code is difficult to read, modifying or extending the code is a daunting task, and adding fundamentally different functionality is essentially impossible. `PHOEBE` adds to the WD code, for example, graphical user interface, new algorithms, and the possibility of scripting. The license is free, the program is public on github[9], and every user is allowed to edit it according to his/her needs.

Now, there are two versions: `PHOEBE 1`, also called legacy (the first version of `PHOEBE` (0.20) was released in 2003), and `PHOEBE 2` (its development began in 2011, the version 2.0 was released in 2017). The latter is considered to be the most powerful tool in these days, since it aims to calculate the most precise solutions as possible. However, more time is required for the computation, compared to the previous version `PHOEBE 1`. The next crucial difference between these two versions is in the grid used and the physics involved (see Fig. 2.6). To increase the precision, triangle elements were chosen in `PHOEBE 2` instead of trapezoids used in `PHOEBE 1` or WD code, and thus the whole surface of stars was covered entirely. The basic principle is that each element of the mesh is populated with local properties (e.g. temperatures) and from the eclipsing algorithm it is determined, which element is visible, which is partialy visible and which is not visible at all. The total flux is obtained by integration over all elements. The `PHOEBE 2` is actively developed in these days (new features and possibility are added), while the `PHOEBE 1` is only fixed for bugs. I have done some attempts to use `PHOEBE 2`, but in this thesis, I will use `PHOEBE 1`, whose reliability has been verified by other users for many years.

[9]https://github.com/phoebe-project

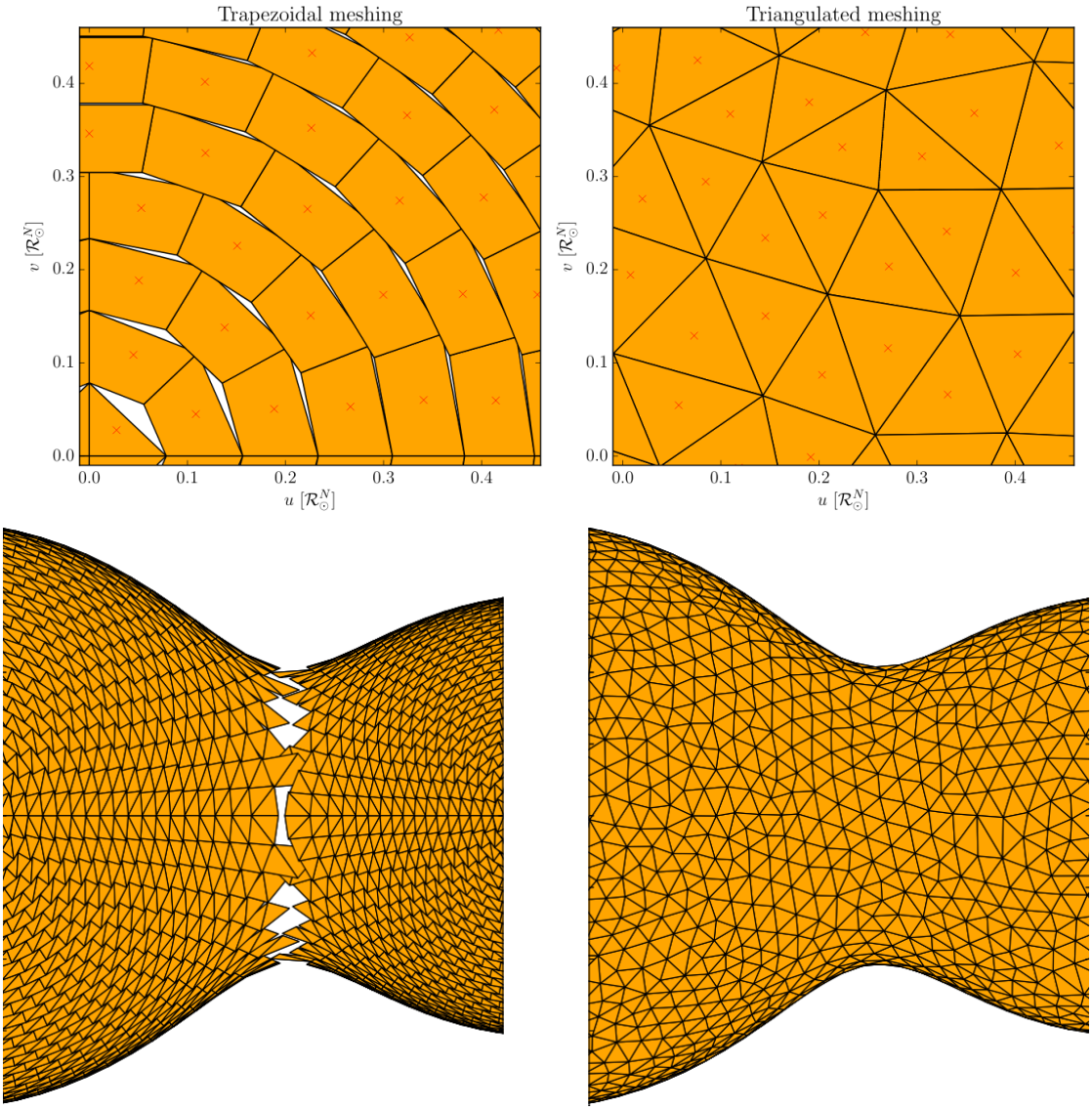

Figure 2.6: The trapezoidal discretization (left) used in `PHOEBE 1` vs. triangular discretization (right) used in `PHOEBE 2`. Source: Prša et al. [2016].

2.2 Data – δ Ori A

Thanks to their brightness, hot stars are easily observable despite their often large distances from us. δ Ori is a naked-eye system; therefore, I have at my disposal a rich collection of spectroscopic and photometric data. The combination of these types of observations enables us to determine all physical parameters.

2.2.1 Photometric data

Photometry is the most accessible data acquisition method. It provides a measurement of the amount of light intercepted by a detector, called a light curve (observed magnitudes/flux with respect to phased time/time). Important points of a light curve are the primary minimum and the secondary minimum. The former is the time when the less luminous component eclipses the brighter one. The latter means the opposite eclipse. The phase difference of these minima depends on the eccentricity of the system. If the orbit is circular or eccentric with $\omega = 90°$ or $\omega = 270°$, then the phase difference corresponds to $0.5P$.

Regarding δ Ori A, I used space-based photometric data from the microsatellite MOST (Microvariability and Oscillations of STars) and nanosatellites BRITE[10] (BRIght Target Explorer) – information about satellites are in Tab. 2.2. The data from MOST, and BRITE cover the periods of 2012–2019 as shows Fig. 2.7. Light curves used for the solution in `PHOEBE` are in Fig. 2.8. The data are primarily influenced by components Aa1 and Aa2; the contribution of Ab was calculated as the third light.

Also, TESS data for this star exists. However, it is strongly influenced by δ Ori C (HD 36485). If the data was used after some reduction, it would increase the uncertainties of the resulting parameters. Thus, I omitted TESS data from my analysis.

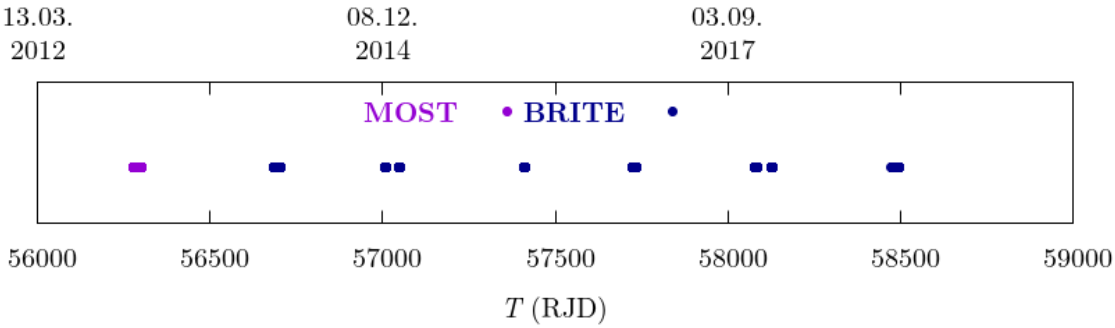

Figure 2.7: The distribution of photometric data in time.

[10]Based on data collected by the BRITE Constellation satellite mission, designed, built, launched, operated and supported by the Austrian Research Promotion Agency (FFG), the University of Vienna, the Technical University of Graz, the University of Innsbruck, the Canadian Space Agency (CSA), the University of Toronto Institute for Aerospace Studies (UTIAS), the Foundation for Polish Science & Technology (FNiTP MNiSW), and National Science Centre (NCN).

Table 2.2: Satellites - Pablo et al. [2016], Kieran et al. [1998]

Satellite	Altitude [km]	Inclination [°]	Period [min]	Period [d]
MOST	785	98.7	101.4	0.07041
UBr (UniBRITE)	775 – 790	98.6	100.4	0.06972
BAb (BRITE-Austria)	775 – 790	98.6	100.4	0.06972
BLb (Lem)	600 – 890	97.7	99.6	0.06917
BTr (BRITE-Toronto)	620 – 643	97.9	98.2	0.06819
BHr (Heweliusz)	612 – 640	98.0	97.1	0.06743

Each BRITE nanosatellite has an aperture of 3 cm, whilst MOST microsatellite's aperture is 15 cm. BTr, BHr, and UBr are equipped with a red filter (the mean wavelength is 620 nm); BAb and BLb have a blue filter (the mean wavelength is 420 nm); and MOST covers the visible range of the spectrum (350–750 nm). All instruments expose at a cadence of less than 100 minutes.

2.2.2 Spectroscopic data

Spectroscopic data (spectra) are coupled pairs of wavelength and flux. From spectra, we can obtain RV curves (RVs with respect to phase), where radial velocities (RVs) are components of the star's velocity reduced to the centre of the heliocentric RVs.

The spectroscopic data sets are composed of all electronic spectra covering the blue, green, and red spectral region (RJD between 50031 and 58405) obtained at the Ondřejov 2-m reflector. These were complemented by spectra from the Haute Provence Observatory Elodie echelle spectrograph and the ESO La Silla Feros echelle spectrograph. Dr. Coralie Neiner offered me to use the Narval and ESPaDOnS series of spectra, which she obtained. The Narval data are from October 2008 and the ESPaDOnS data from November 2014 and March 2016. The RV curve of the component Aa1 used for the solution in `PHOEBE` is in Fig. 2.9.

2.3 Analysis

Several main computer programs were used to the analysis. The normalization, removal of residual cosmics and RV measurements of all spectra were carried out with the program `reSPEFO2`. The rebinning of the spectra to a scale linear in RV, that is needed as the input for `KOREL`[11], which uses the observed spectra and derives both orbital elements and disentangled spectra of all components, was carried out with the program `HEC35D`. The variable quality of individual spectra was taken

[11] http://www.asu.cas.cz/ had/korel.html

Table 2.3: Journal of the electronic spectra.

Time interval (RJD)	No. of spectra	Detector (Observatory)	Wavelength range (Å)
53613.62–56003.35	70	Site-5 CCD (Ondřejov)	4753–5005
55836.57–58405.57	65	Site-5 CCD (Ondřejov)	4270–4523
50031.68–50435.40	4	Elodie (Haute-Provence)	4000–6800
54136.58–54953.46	6	FEROS (European Southern)	4000–8000
56967.92–57449.83	428	ESPaDOnS (Midi-Pyrénées)	optical range
54763.49–54764.56	43	Narval (Midi-Pyrénées)	optical range

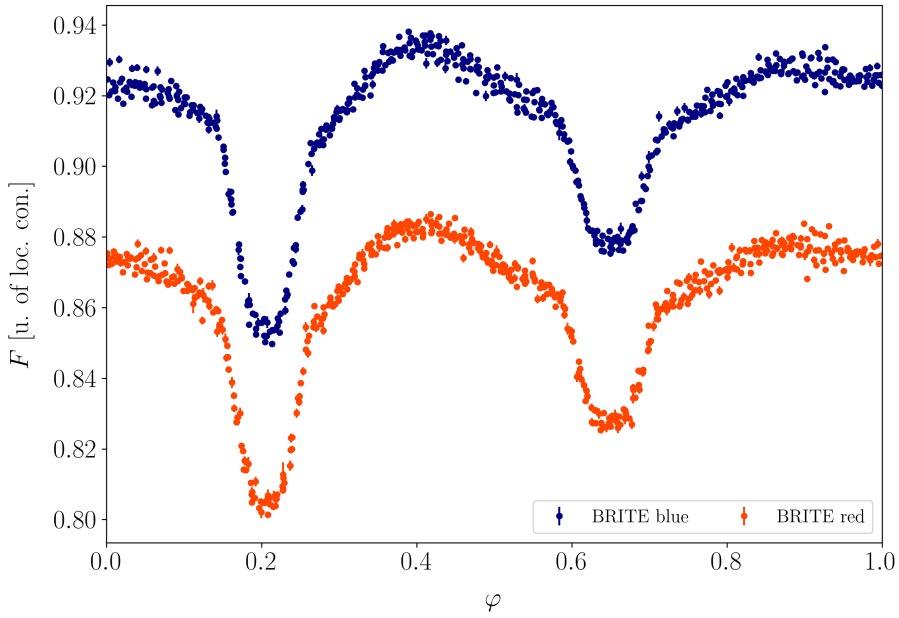

Figure 2.8: Light curves used for the solution in `PHOEBE`.

into account by measuring their signal to noise ratio S/N in the line-free regions. Thus, each spectrum had a weight according to this formula

$$w = \frac{(S/N)^2}{(S/N_{\mathrm{mean}})^2}, \tag{2.1}$$

where the denominator denotes the mean signal to noise ratio of all spectra.

The use of `KOREL` for this system included several problems that made the task of finding the optimal solution more complicated. The rotationally broadened

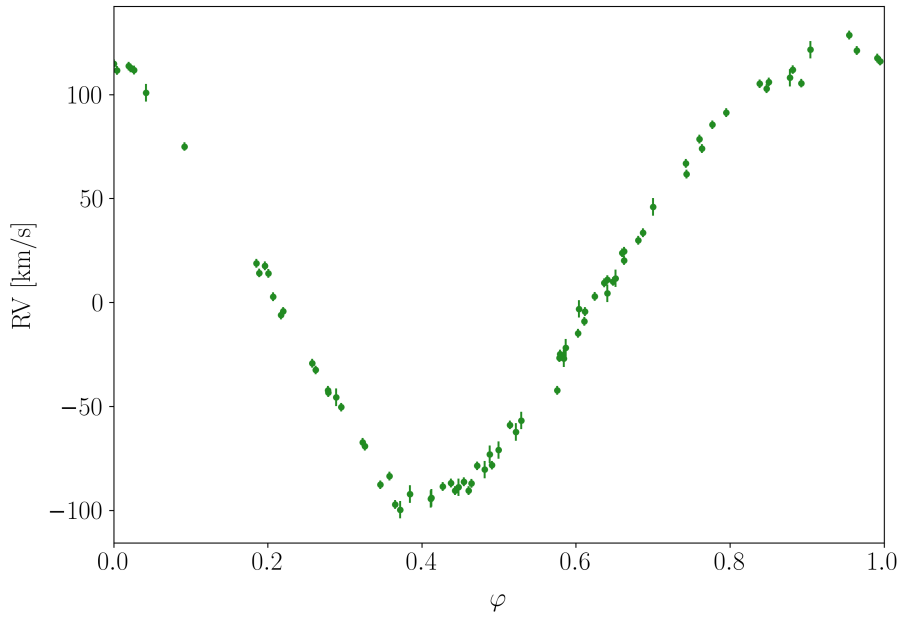

Figure 2.9: RV curve of the primary Aa1 used for the solution in `PHOEBE 1` [Mayer et al., 2010].

spectral lines of the primary and tertiary are heavily blended with each other in all orbital phases and altogether dominate the line spectrum. Consequently, the contribution of a very faint secondary spectrum to the resulting sum of squares of residuals is almost comparable to the noise of the spectra. What is more, the dependence of sum of squares on q is flat over a large range of values.

The detection of the secondary in blue spectra was achieved by using the method of spectral disentangling in two steps. The approach to the problem in this method is such that in the first step the spectra of primary and tertiary were disentangled. Then the residuals for all individual spectra after disentangling in the first step were increased by one and were used as the input for `KOREL` in the second step, this time searching for the lines of the secondary only.

To derive more precise orbital elements, I used blue and green spectral regions. A contour graph of χ^2 values with Python program `KORELMAP` was created (see Fig. 2.10) and according to this graph and an appropriate continuum of disentangled spectra, I chose the optimal values of initial parameters for a file controlling `KOREL`.

In the next step, I looked for an orbital solution using `KOREL` in chain using controlling file `korel.par` in Att. A.1. The program KOREL started the process considering the primary and tertiary with variable intensities. The converged parameters for the orbit of a close pair were the time of periastron passage, ec-

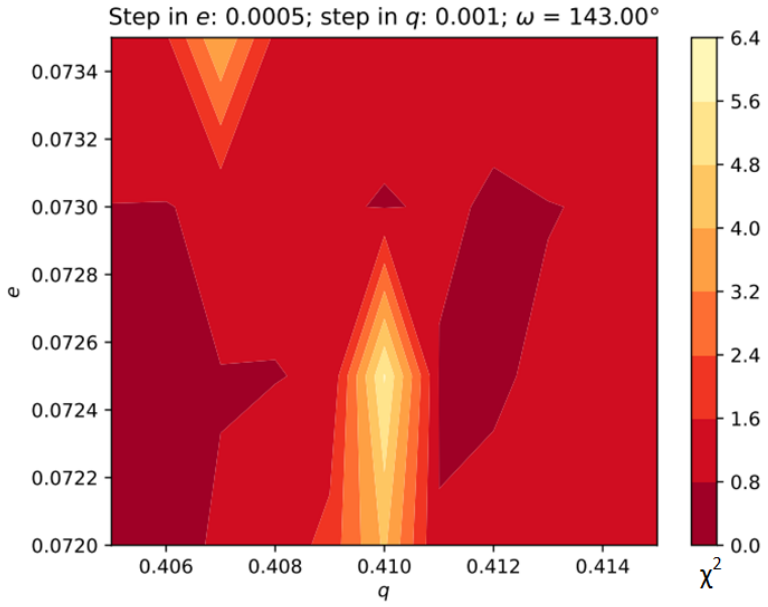

Figure 2.10: A contour graph dosplaying χ^2.

centricity, periastron longitude, and semiamplitude of the RV. For the outer orbit it was: time of periastron passage and the semiamplitude of radial velocity. In the following step, the program continued with the solution of the primary and tertiary with constant intensities and the secondary with variable intensity converging the time of periastron passage and mass ratio. In the last step, `KOREL` found the solution for all three components with constant intensities fixed from previous step. The solution for the lowest value of χ^2 leads to the determination of this mass ratio $q = 0.41549$ and eccentricity $e = 0.0758$.

Then, I used the disentangled blue spectra to estimate the radiative properties like the effective temperatures, logarithms of gravity accelerations, $v \sin i_{\rm rot}$ values, and relative luminosities $L_{\rm R_i}$ with the program `PYTERPOL`. Metalicities of both components were fixed to the value for the Sun (0.0196). The program uses observed spectra and a large grid of synthetic spectra and finds the appropriate fit between them and interpolated model spectra using a simplex minimization technique. The results of the calculation in `PYTERPOL` are summarised in Tab. 2.4 and the comparison of disentangled spectra with the synthetic ones are in Fig. 2.11. The faint secondary contributes only a few per cent of the total flux.

To obtain the final solution, I used the program `PHOEBE 1`[12] [Prša and Zwitter, 2005] that is able to combine photometry and spectroscopy. However, first of all, my intention was to improve the homogenisation of photometric data. I created

[12]http://phoebe-project.org/1.0

Table 2.4: Parameters derived by PYTERPOL.

Parameters	Primary Aa1	Secondary Aa2
$\chi^2_{\rm N}$	2.562	1.769
$T_{\rm eff}$ [K]	31401	25442
log g [cgs]	3.549	3.476
$v \sin i_{\rm rot}$ [km s^{-1}]	114.280	89.506
$L_{\rm R_3}$	0.692	0.035
RV [km s^{-1}]	26.25	36.44

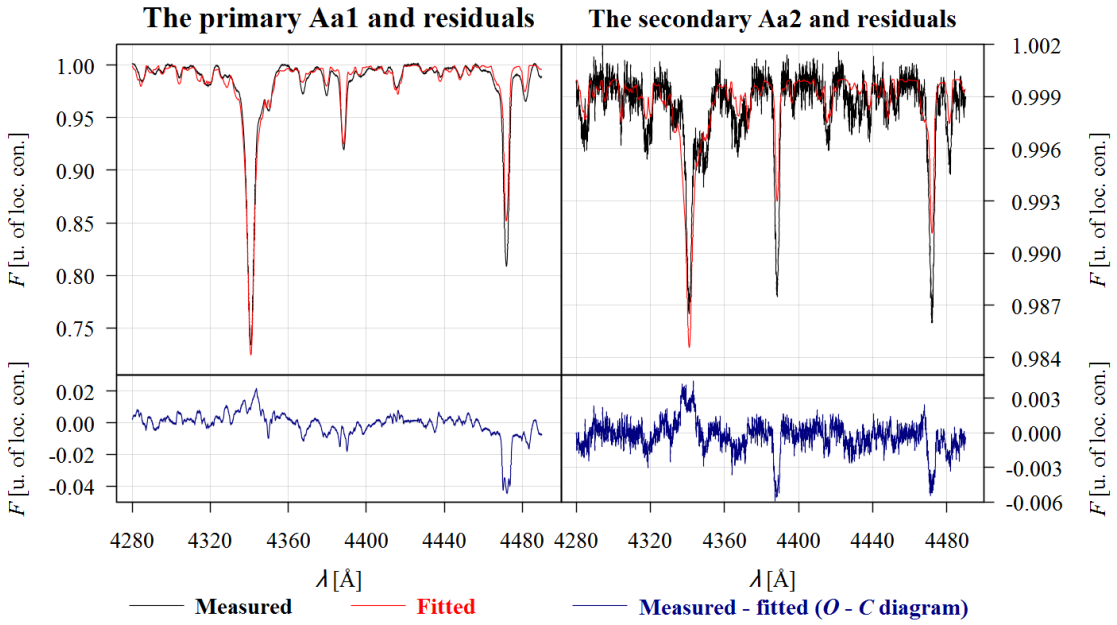

Figure 2.11: The comparison of disentangled spectra of the primary and secondary with the best-fit synthetic spectra found by Pyterpol. The range from 428 to 449 nm was used for the disentangling, and the step in RV was set as 0.1 km.

normal points over the orbital periods of the satellites to eliminate possible residual instrument effects, and omitted normal points with rms errors larger than average rms.

All BRITE normal points are plotted in Fig. 2.12. There is an obvious trend, that caused a problem during the solution in PHOEBE. Thus, I interpolated maxima of light curves by Hermite polynomial. Fig. 2.13 shows what the result of homogenization of BRITE data looks like.

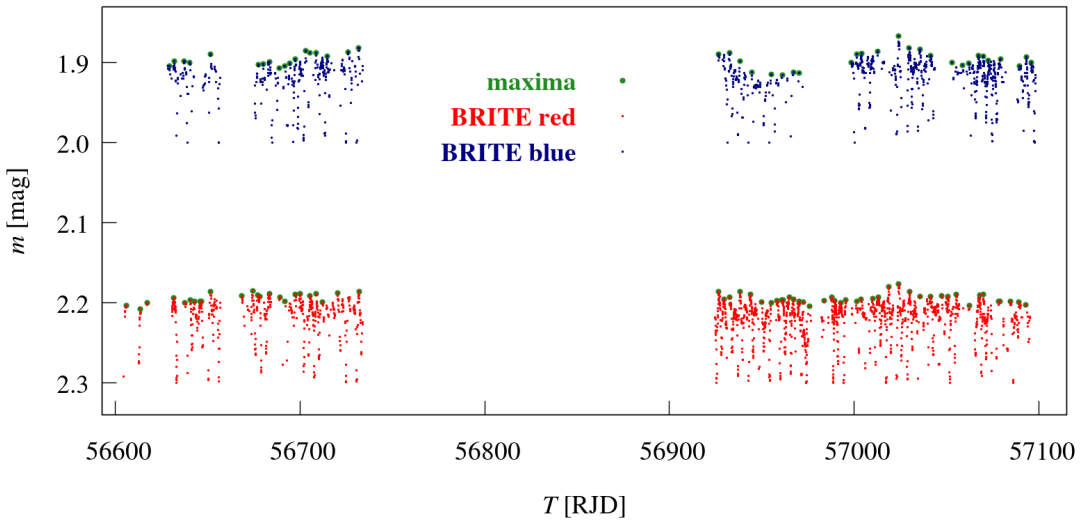

Figure 2.12: All BRITE points with marked maxima.

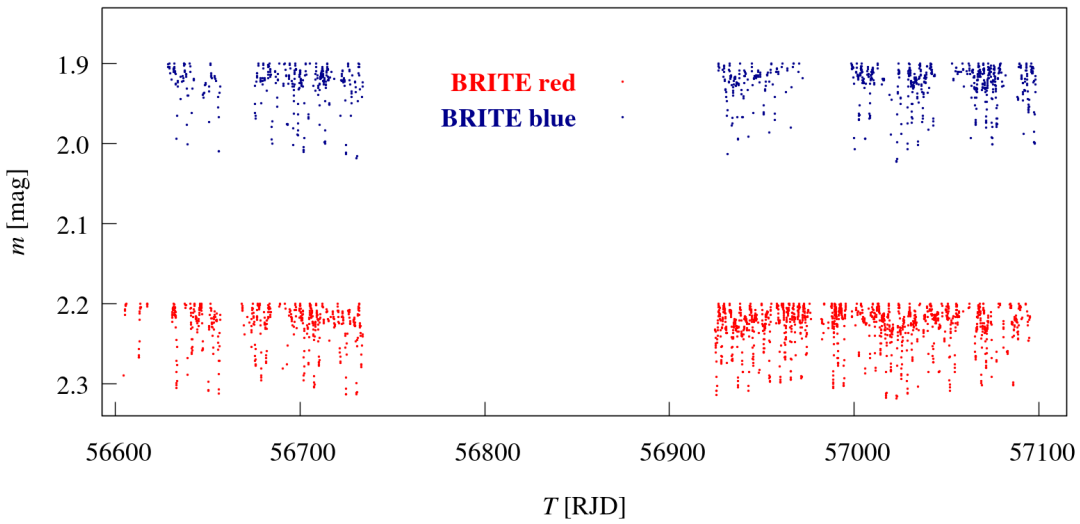

Figure 2.13: BRITE data homogenised by Hermite polynomial.

Parameters that were kept fixed are in the right part of Tab. 2.5. The linear limb darkening for each filter was used for the solution in `PHOEBE`. It follows Andrej Prša's model, computed effective temperatures for the logarithms of gravity darkening. The exponent of gravity darkening was set as $\beta = 1$ (effective temperatures of both components are greater than 10 000 K) according to Claret [1998, Fig. 7] or Claret [2001, Fig. 7] showing the relation between the gravity darkening and

effective temperature.

After each iteration, synchronicity parameters F (that is the ratio of the orbital and rotational period) were re-calculated using this formula [Koubský et al., 2019]

$$F_{\rm k} = P_{\rm orb} \frac{v_k \sin i}{50.59273 R_k^{\rm e} \sin i} \tag{2.2}$$

where k denotes the component number and R its equatorial radius in nominal units[13]. The constant of 50.59273 also corresponds to nominal units; the orbital period is in days and the rotational velocity v_k in km/s. The resulting values are in Tab. 2.5 (left part).

2.3.1 Presence of circumstellar material

To verify whether there is some observable circumstellar material around the star, I analysed the changes of shapes of H_α lines. To this, I used the high-resolution Narval data from October 2008 and the ESPaDOnS data from November 2014 and March 2016, which include many spectra secured during each night. I computed the average spectra in each night, subtracted then from individual spectra in each night series and plotted the residuals spectra. The most pronunced changes were seen in the Nov. 5, 2014 series (Fig. 2.14), but it is still not sufficient to say this conjecture to be true. Whether this is an indication of variable amount of circumstellar material or evidence of rapid line-profile changes (also reported by Kholtygin et al. [2006]), remains to be investigated in the future.

2.4 Results and discussion

Tab. 2.6 shows a comparison of the final values of the component masses and radii obtained in this study with the compilation of normal masses and radii published by Martins et al. [2005] (calibration of O-stars' stellar parameters) and Harmanec [1988] (formulae based on fitting observed data[14]). The agreement is good for the primary and satisfactory for the secondary. Rapid microvariability of the high-resolution H_α line profiles was formed but not convincing evidence of the H_α emission was documented.

[13] Nominal units were the outcome of the International Astronomical Union (IAU) resolution B3 in 2015.

[14] $X = \log T_{\rm eff}$
$4.62 \geq \log T_{\rm eff} \geq 3.425$
$\log \frac{M}{M_\odot} = [(1.771141X - 21.46965)X + 88.057]X - 121.6782$
$\log \frac{R}{R_\odot} = [(2.166639X - 26.91528)X + 112.1089]X - 156.117$

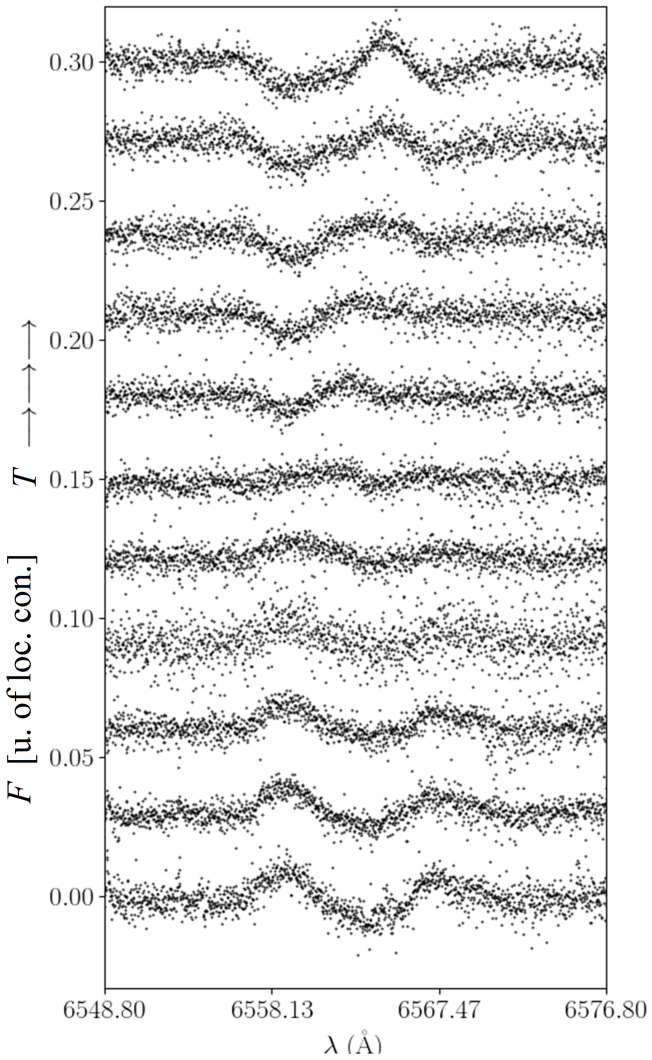

Figure 2.14: The difference of the average spectrum and individual spectra. Each 10th spectrum of the night was plotted.

The theoretical values for the primary are related to the spectral type and the theoretical values for the secondary are computed as a function of the effective temperature, so the difference of values indicates bigger inaccuracy of the effective temperature of the secondary derived by `PYTERPOL`. On the other hand, the resulting mass corresponds to the radius considering this spectral type. The solution was stable and gives reasonable masses and radii for the primary and the secondary.

The results for verifying the conjecture about the presence of circumstellar

Table 2.5: Solution to δ Orionis from `PHOEBE 1`.

Parameters	Values
a [$\mathcal{R}_\odot$]	41.91 ± 0.18
ω [°]	148.73 ± 1.49
γ [km/s]	21.96 ± 0.33
i [°]	78.1 ± 0.3
M_1 [$\mathcal{M}_\odot$]	21.1
M_2 [$\mathcal{M}_\odot$]	8.8
R_1 [$\mathcal{R}_\odot$]	13.6
R_2 [$\mathcal{R}_\odot$]	3.7
M_{bol_1} [mag]	-8.28
M_{bol_2} [mag]	-4.55
L_{R_1}	0.690
L_{R_2}	0.037
$\log g_1$ [cgs]	3.50
$\log g_2$ [cgs]	4.24
F_1	0.958
F_2	2.763
χ^2_{N}	11.389

Fixed param.	Values
P [d]	5.732 436*
$\dot{\omega}$ [°/d]	0.004 220*
$q = M_2/M_1$	0.415 49**
e	0.075 83**
T_{eff_1} [K]	31401***
T_{eff_2} [K]	25442***
L_{R_3}	0.273***

* Mayer et al. [2010]

** from `KOREL`

*** from `Pyterpol`

material around the star by analysing changes of shapes of H_α lines remind fast variability of the profile discovered by Kholtygin et al. [2006]. This series of spectra would be worth studying as dynamical specra. The profile variations are probably due to non-radial pulsations (NRPs) in O stars.

Table 2.6: The comparison of results (red) with theorethical values.

	Star	Spectral type	M ($\mathcal{M}_\odot$)	R ($\mathcal{R}_\odot$)
BRITE, MOST	del Ori Aa1	O 9.5 II	21.1	13.6
Martins et al. (2005)		O 9.5 III	21.04	13.37
BRITE, MOST	del Ori Aa2	B 1 V	8.8	3.7
Harmanec [1988]			10.41	4.75

3. Omega Canis Majoris

ω CMa (Omega Canis Majoris, 28 CMa, HD 56139, HIP 35037, HR 2749) in the constellation of Canis Majoris (see Fig. 3.1) belongs to the class of bright B2e stars. Its brightness varies between 3.52 and 4.18 mag in the visual passband. This star has been well observed since 1903; thus, numerous data sets with various observational techniques are available. Many studies have been devoted to this star, especially after Baade [1982a,b, 1984] discovered its very pronounced radial-velocity (RV), line asymmetry, and V/R changes with a remarkably stable period of (1.36673 ± 0.00005) days. It became one of the first of the early-type line-profile variables to be systematically studied. Baade [1984] has shown that the outer wings of the absorption lines lead only to little or no RV changes. Then, contradictory results about its periodic variability were published – see Tab. 3.1.

Harmanec [1998] analysed all available spectroscopic and photometric data and found at least three, possibly four, different time scales of variability of the star. He concluded that the period of the line-profile and RV changes is 1.371906 d instead of 1.36673 d derived by Baade [1982a]. Moreover, he found that the period is not constant on a long-term basis, but varies cyclically. He discovered slow and smooth $O-C$ residuals of this period from a linear ephemeris and made a conjecture that the strength of the Balmer emission and the star's brightness varies in a cycle of thousands of days. These long-term changes could be explained as consequences of the formation and gradual dispersal of a gaseous envelope that is flattened and seen rather pole-on. During each episode, the envelope grows from an optically thick pseudophotosphere to a more extended and optically thin envelope. He noted that the $O-C$ residuals of the local epochs of RV maxima from a linear ephemeris show variations in time. The period is shorter when the star is brightest as the envelope begins to grow. The $O-C$ residuals could be reconciled with a period of 34.675 d as well. Some evidence of this period could also be recognised in photometry and amplitude of the 1.37 RV changes. He also used simulated data to show that the smooth, slight cyclic variation of the 1.372 d period can be misinterpreted for multiperiodicity with several close periods if Fourier period analysis is applied to the observed RVs. He was also the first to note that the visual magnitude of the star outside the cyclic brightening is secularly decreasing.

Štefl et al. [1999, 2003a,b,c] obtained new spectroscopic (275 He I 6678 line profiles) and photometric (Strömgren and Geneva) observations of the star and carried out an analysis of these and previously-secured data covering 16 years. They concluded that two periods of 1.37 d and 1.49 d are present in the observed variations of the star in addition to the long-term changes. They confirmed earlier findings that the amplitude of the rapid photometric variations is larger at emission phases when the mean optical brightness of the star is higher.

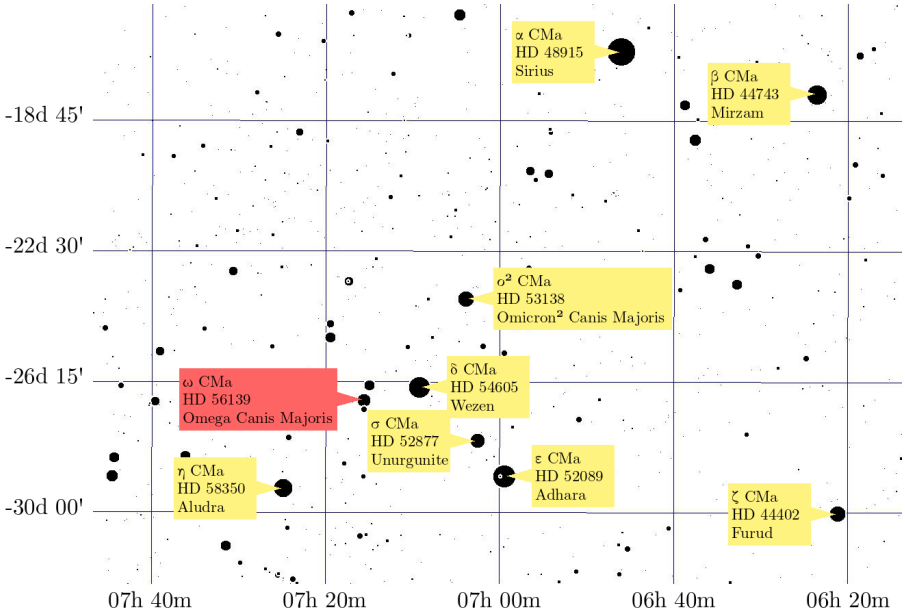

Figure 3.1: The map as in Fig. 2.2 but for the bright southern Be star Omega Canis Majoris in the constellation of Canis Majoris. Source: TheSky (astronomy software).

Ghoreyshi [2018] devoted his research to quasi-regular outbursts that ω CMa exhibits more or less every 8 years. 3 or 4 years after these outbursts, a new disk is formed. In the range of 4 and 6 years, the disk dissipates. He has a numerous dataset from March 1964 onward, including spectroscopy, photometry, polarimetry, and interferometry. This data documents several outbursts and quiescence phases allowing him to investigate how disks grow and dissipate.

The aforementioned studies of spectral, radial-velocity and line-profile variability or secular photometric changes indicated at least three or four timescales of variability. While the asymmetry of profiles of absorption lines, the RVs of emission lines, and their V/R ratios vary with a period of 1.37 days, the strength of the Balmer emission varies on a timescale of several thousand days. Furthermore, the star's brightness outside emission episodes is secularly decreasing over the time covered by observations. Finally, there exists a suggestion that small cyclic changes in the exact value of the 1.37 d period could be correlated with the presence or absence of the emission. An attempt to proove or disprove this conjecture is one of the goals of this thesis.

Table 3.1: Contradictory resulting periods found for ω CMa.

Paper	Conclusions
Baade [1982a]	RVs, line asymmetry, and V/R changes with the period of (1.366673 ± 0.00005) d.
Baade [1982b] *uvby* photometry	The light variations indicate a shorter period, 0.435 d, than the spectroscopic period.
Stagg [1987] UBV photometry	The spectroscopic period of 1.365 d was confirmed in photometric measurements; the period of 0.435 d was claimed as an alias of the spectroscopic period.
Balona et al. [1987] *b* observations	A monotonic decrease of the brightness over one year noted. The period of 1.471 d was determined from 1986–87 data when the star was relatively stable and about 0.3 mag fainter than at the beginning of 1985–86 season.
Clarke [1990] polarimetry and Hβ scans	The period of variations is twice the spectroscopic period, 2.7335 d.
Mennickent et al. [1994] *uvby* photometry	Long-term brightness variations and the presence of quasiperiodic light changes with a cycle of about 25 d at the phases of increased brightness are reported.
Balona et al. [1998] high-resolution spectra	The presence of 1.37 d period in the line He I 6678 is confirmed.
Štefl et al. [1998] HEROS spectra	Two periods are present, the stable period of 1.37 d and the transient period of 1.49 d. The second one was found only in the lines affected by the circumstellar emission.
Harmanec [1998] is RV data and photometry	The mean period of the RV and line-profile changes 1.371906 d. This period could vary with the period of 34.675 d. Values of 34.675 d or 1.35 d might correspond to $O-C$ deviations of the local epochs of RV maxima from a linear ephemeris for the 1.371906 d period.
Štefl et al. [2003a,b,c] Spectroscopy and photometry	Two periods of 1.37 d and 1.49 d are present in the observed variations of the star in addition to the long-term changes.

3.1 The theoretical background of used methods

For measuring quantities such as radial velocities RV, V/R ratio, the strength of emission line or bisector velocity span BVS, programs `reSpefo` (written by Adam Harmanec) and `The_bisector_method` (I have created it for measuring BVS) were used. To determine the period, Stellingwerf's method implemented in `hec27` (written by Petr Harmanec) was used. To estimate the uncertainty of the determined period, I implemented the bootstrap method in the simple `bash` script. The correlation of RV with BVS was determined by `The_bisector_method`. For the $O-C$ diagram, the program `efem` from Petr Harmanec was used.

3.1.1 The Stellingwerf method

The method introduced by [Stellingwerf, 1978] is phase dispersion minimisation method (PDM), one of the folding techniques, in which data sets are divided into bins that can be statistically analyzed to determine whether the entire data set is periodic according to the statistic θ. This technique is appropriate for data sets with irregularly spaced observations and non-sinusoidal time variations. These features of data do not allow us to use Fourier techniques, which associates a function of position by time with a function of frequency. However, the Fourier transform requires that the original function have a representation as a Fourier series, which in turn requires that the original function be periodic. However, that is what we do not know, so we cannot assume it. Moreover, Stellingwerf's method does not assume there is a phase curve. Instead it allows the investigator to test various proposed phase curves to determine the likelihood that any of the proposals match the data; thus, it is very general.

The basic idea of this method is the following: If the time-sequence data is folded by the correct period P, then the result shows minimal scatter (dispersion) within all bins in phase. The method tries a sequence of periods, binning the data by the length of each period and comparing the sum of the variance of the bins to the variance of the overall data. The period most likely to be the closest to the actual period is the one that gives a sum variance closest to the overall variance. For uneven data with gaps, one can use adaptive binning. Thus, several trial periods are tested, and the period with the smallest sum of dispersion smallest sum over the dispersion from each bin is theoretically the best period.

Let us assume observations with respect to time (T_i, O_i), where i runs from 1 to the total number of observations N. The sum of dispersion is given by

$$\sigma^2 = \frac{\sum_i (O_i - \overline{O})^2}{(N-1)}, \tag{3.1}$$

where

$$\overline{O} = \sum_i \frac{O_i}{N} \tag{3.2}$$

is the mean of the measured variable O. For any subset O_i we define the sample variance s^2 as in Eq. (3.1). If we choose M distinct samples containing n_j data points and having variances s_j^2, where j runs from 1 to M, then the overall variance for all the samples is

$$s^2 = \frac{\sum_j s_j^2 (n_j - 1)}{\sum_j n_j - M}. \tag{3.3}$$

To find the best period, one needs to minimise the overall variance given by Eq. (3.3).

This method picks M samples from O in such a way that all chosen samples have a similar phase. Thus, the entire phase interval (0, 1) is divided into bins with a fixed size, known as phase bins, and samples are chosen to satisfy the criterion. It is not necessary to assign each point to an interval and to choose every point. The way to divide the phase interval is called representation. Assume that a representation includes five phase bins of size 0.2 covering the phase from 0 to 1, then another representation is, for example, five intervals of the same size covering the phase from -0.1 to 0.9.

The goodness of the period is given by Θ statistic

$$\Theta = \frac{s^2}{\sigma^2}, \tag{3.4}$$

where s^2 and σ^2 are computed according Eqs. (3.3), (3.1), respectively. If the period is not acceptable, $\Theta \approx 1$, i.e., $s^2 \approx \sigma^2$. If the period is satisfactory, Θ is near zero and reaches a local minimum.

The method is implemented in the program `HEC27` written by Petr Harmanec[1]. The program's run is controlled via a file including several parameters, for instance, the number of phase bins, the number of representations, the range of period values, and a step in this range. The input data is a time sequence and a variable associated with time points.

3.1.2 Randomness and its use in the bootstrap method

Randomness in one of its manifestations is the quality in the limit of a sequence of numerical measurements, for which any particular measurement cannot be reliably determined from any pattern in the previous measurements even if you know how the measurements were taken. It is impossible to predict the following

[1] Available at https://astro.troja.mff.cuni.cz/ftp/hec/HEC27/

number in the sequence and reiterate the outcome. What outcome we obtain one time has no effect on what we obtain the next time. Random also means it is very unlikely that the same pattern will be observed in repeated trials. In the limit, a random sequence of measurements represents the actual distribution of values of the phenomenon being measured.

Since it is difficult to produce a sequence that is truly random, we use a deterministic algorithm to generate sequences that retain some of the properties of random sequences. We drop the requirement that we do not know how they are generated. Pseudorandomness is the phenomenon of a deterministic sequence possessing the statistical properties of a random sequence (at least for a long time – they may be periodic). Pseudorandom sequences are generated from a seed value deterministically (so they a repeatable given the same seed). Pseudorandom generators produce numbers that seem random, but they are not.

Historically, pseudorandom numbers were used to make calculations for the Manhattan Project, which was seeking to devise a nuclear fission bomb, predating the H-bomb by a decade. For this computation, random number sequences that looked like a random sequence that could be reproduced were needed. In this era, the first pseudorandom numbers were generated by an algorithm known as the middle-square method:

1. Select a seed as a target number.
2. Multiply the target number by itself.
3. Select the middle digits of the product as the output and make this the new target number.
4. Go to step 2.

Such a sequence of numbers is dependent only on the initial seed. If Step 3 produces a target equal to the seed, then the sequence repeats and so cannot be random. Pseudorandom sequences are deterministic as opposed to non-deterministic random sequences.

We can visualise a random sequence by plotting a path changing direction according to each number. We obtain what is known as a random walk. The lack of pattern is obvious. Let us consider the same plot for a pseudorandom sequence. To a certain extent, the corresponding walk seems similar to a random walk. Nevertheless, after a long time, the pseudorandom sequence must eventually repeat as the algorithm reaches the initial seed. The number of steps before the pseudorandom sequence starts to repeat is called the period. The size of the period depends on the number of seed's digits. For two-digit, three-digit, and four-digit seeds, the algorithm produces a cycle not exceeding 100, 1000, and 10000

numbers before repeating, respectively. As far as a large-digit seed is concerned, the sequence can expand into an arbitrarily long sequence before repeating. The advantage of using pseudorandomness is its speed. Pseudorandom generators are usually very much faster than truly random number generators. Hence, when we need random numbers, we have to use pseudorandom numbers. The next advantage is that after doing research, we can publish our pseudorandom generator and the seed to allow everyone to verify our results. With a random generator, we would publish results without the possibility of verification.

Pseudorandomness is used in various methods of statistical analysis. It often happens that there is missing information about measurements. This is not a problem thanks to randomness or pseudorandomness, which can generate the missing information. For instance, random numbers are necessary for methods for estimating deviations (bootstrap), searching for periods in a noisy signal, for Monte Carlo methods, and various simulations. In this thesis, I will use the bootstrap method for estimating the uncertainties.

The bootstrap method

The bootstrap method is used to guess deviations of parameters of a model from measurements that are not repeatable. Except for bootstrap, other methods for estimating deviations work in the following way: Let us denote by $\mathcal{D}_T$ the true measurement. Randomly-generated noise is added to them. Thus, we obtain a set of k simulated measurements, out of which we have k values of parameter. From these, we plot a histogram, which approximates the shape of the probability density function of the measured value of the parameter as k tends to infinity. Finally, we choose a confidence interval and get the deviations. The amount of added noise nonetheless influences the results.

The bootstrap method, which was developed by Australian statistician John Hartigan [Hartigan, 1969], does not need added noise. It estimates the errors directly from the measured data; thus, it is more objective, compared with the other methods. We have a set of measurements $\mathcal{D}_0$ consisting of N elements. Using randomness, a program chooses N elements uniformly at random from $\mathcal{D}_0$ with repetition. There are $\binom{2N-1}{N}$ multisets of size N on a set of N elements. In selecting uniformly at random N elements one at a time from an N-element set, each element has a $1/N$ choice of being selected each time; thus, the probability of not being selected each time is $1 - \frac{1}{N} = \frac{(N-1)}{N}$. It follows that the probability of a specific entry not being chosen during N choices is $\left(\frac{N-1}{N}\right)^N$. As N tends to infinity, we get the limit

$$\lim_{N\to\infty}\left(\frac{N-1}{N}\right)^N = \frac{1}{e} = 0.368. \tag{3.5}$$

Thus, it holds that duplicates of original data will replace approximately 36.8% of entries. This method investigates the sensitivity of parameters to data.

3.1.3 Asymmetry of spectral line profiles studied with the bisector method

Both the line asymmetry and RVs of the star ω CMa vary with a period of 1.37 days. The star's circumstellar envelope causing the emission line in the star's spectrum varies cyclically on a time scale of years. Harmanec [1998] conjectured that the extension of this circumstellar envelope is correlated with the variation in luminosity and RV. To test this conjecture, I use the bisector method, which is effective in detecting spectral line profile asymmetries and provides, together with the RV measurements in the program `reSPEFO` the necessary data to test the conjecture. This subsection gives the necessary theoretical background to the bisector method and statistical correlation. The latter is used to assess the results of the bisector method and measured RVs.

Spectral line profiles give light intensity I (or flux F) as functions of wavelength λ (or frequency ν). They are parts of electromagnetic spectra that stars emit. Changes of intensity are caused by the transitions of atoms or molecules from one energy level to another. We distinguish two types of spectral line profile in the visible part of the spectrum – the absorption line profile and the emission line profile. The former occurs when a photon with an energy equal to the difference between two energy levels is absorbed. This causes an electron to be excited to a higher energy level. The latter occurs when the excited electron returns to the ground state. According to quantum mechanics, a transition between energy levels will produce a spectral line at a discrete wavelength (or frequency); nevertheless, there are many processes leading to a broadening of the lines, such as natural broadening due to the Uncertainty Principle. By this principle, the energy levels are not infinitely sharp, and thus we observe a spectral distribution $I(\lambda)$ or $I(\nu)$ in the neighbourhood of a wavelength value called central wavelength λ_0 (or central frequency ν_0) where the molecular transition occurs. The central wavelength is proportional to the energy difference between two levels of molecular transition. This distribution is called the spectral line profile. The fundamental quantity characterising a spectral line profile is the full-width at half-maximum (FWHM). This is defined as the wavelength interval $|\lambda_2 - \lambda_1|$ between the two wavelengths λ_1 and λ_2 satisfying $I(\lambda_1) = I(\lambda_2) = \frac{1}{2}I(\lambda_0)$, or equivalently, the two frequencies ν_1 and ν_2 satisfying $I(\nu_1) = I(\nu_2) = \frac{1}{2}I(\nu_0)$. The spectral region from λ_1 to λ_2 is called the core of the line and the regions outside, meaning $\lambda < \lambda_1$ and $\lambda > \lambda_2$, are called the line wings.

A star whose spectral line profile is being measured belongs to an environment

whose physical conditions affect the shape of this profile. In this way, spectral line profiles can be used to investigate these physical conditions in the environment of the star as well as to identify the atomic and molecular components of the star itself. None-moving sources not influenced by external fields would have symmetric spectral line profiles, while other sources with an external electric field or moving at a high speed have asymmetric profiles. The asymmetry is called the thermal Doppler effect. Excluding asymmetry, this effect leads also to broadened spectral lines. The Doppler effect describes the shifts and deformations that arise from the movement of radiation sources, including those under consideration here, namely stars composed of plasma. When a source moves towards us, the light gets extra energy; thus, its wavelengths are shifted to shorter wavelengths corresponding to higher frequencies. For visible light, shorter wavelengths are at the bluer end of the spectrum; therefore, we say the light is blueshifted. Similarly, a redshift occurs when the source moves away from us. Based on the colours of the spectrum, the left part of the spectral profile is known as blue; the right, as red. The following equation defines the Doppler shift:

$$\frac{\lambda - \lambda_0}{\lambda_0} = \frac{v_\mathrm{r}}{c}, \tag{3.6}$$

where $\lambda - \lambda_0$ stands for the difference between the wavelength λ of the light emitted by a moving object and the wavelength λ_0 emitted by an identical, stationary object; c, for the speed of light; and v_r, for the RV (the velocity of the star in the direction towards the observer). The difficulty in investigation of physical condition is that different parts of the spectral line profile arise from different parts of the stellar's atmosphere, each at different heights. For example, the wings are formed in the inner part of the atmosphere, while the line core is produced in an upper one. Moreover, different layers may move with different radial velocities; thus, they differ in their shift.

Bisectors

The bisector method provides a complete description of asymmetry in the spectral line profile. Let x be the distance from the central wavelength λ_0 of a spectral line measured in units of velocity, i.e., the shift in wavelength based on the Doppler effect, which Buonaura (1982) defined as Eq. 3.6 for $v_\mathrm{r} = x$.

Fig. 3.2 displays the variable x given by wavelength λ and a line profile $I(x)$ is the intensity given as a function $I(x)$ of x instead of wavelength λ. A bisector $\overline{x}$ is defined to be the midpoint of the horizontal line segment connecting the closest points of equal intensity to the blue (left) and red (right) sides of the profile. The bisector line is a curve connecting bisectors ranging from the core towards the

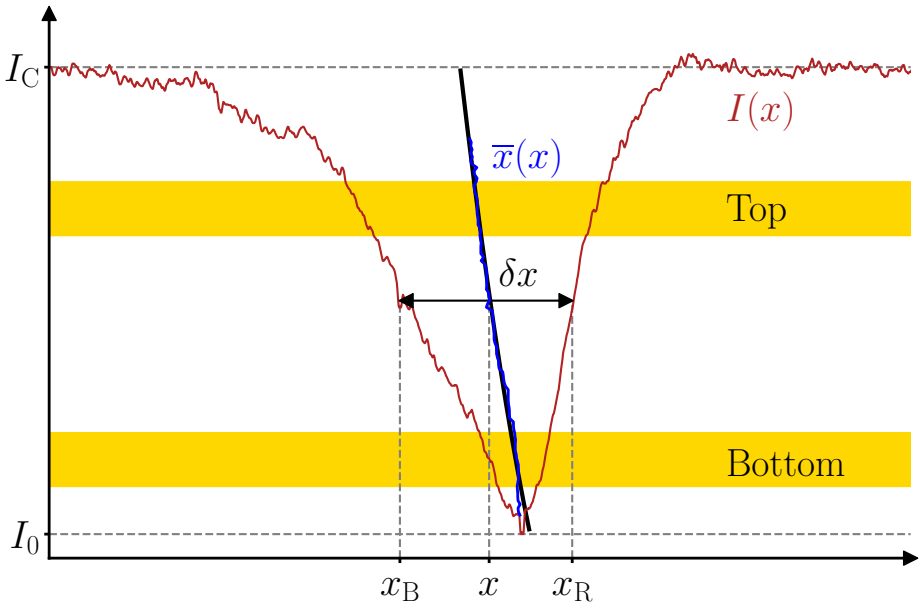

Figure 3.2: A spectral line profile. Notation is as introduced in the text.

profile's wings, i.e., from the intensity I_0 to I_C. The bisector can be expressed as

$$\overline{x} = \frac{x_B + x_R}{2}, \tag{3.7}$$

where x_B and x_R are distances related to a value of intensity I from x with the same intensity and belonging to blue and red parts of the profile, respectively (see blue curve in Fig. 3.2). Points constituting the bisector correspond to the velocities of the plasma movement in which the part of the profile is formulated as the plasma velocity influences the asymmetry of the spectral line profile.

The bisector method is widely used thanks to its simplicity. Nevertheless, the following problems arise from this method:

(i) The causes of observed asymmetries are not identified. The method does not distinguish between the case in which emission of radiation is from layers moving away from the observer or the case in which absorption is from layers moving towards the observer.

(ii) The method requires the spectral line profile not to be too flat; there must be prominent local extremes near the central wavelength.

Therefore, it is not obvious in what direction the layers of atmosphere producing the spectral lines are moving after applying this method. Nevertheless, we can find out this piece of information by measuring the RV corresponding to line's cores and line's wings. Considering the second shortcoming, we need to identify the spectra that are not appropriate for this method, i.e., the profiles that are too flat and reject them from the analysis.

To quantify the asymmetry in a spectral line profile, it is necessary to introduce *the bisector velocity span* [Toner and Gray, 1988]. The top part of the profile near the wings and the bottom part close to the line's core represent essential regions to study the bisector line's velocity. These regions can be arbitrarily chosen for the whole set of spectra as parts including the bisectors near the lowest intensity and the highest intensity (see Fig. 3.2). Denoting the average values of velocities in the top and bottom zones by V_{T} and V_{B}, respectively, their difference $V_{\mathrm{T}} - V_{\mathrm{B}}$ is called the bisector velocity span (BVS). We can now determine the linear correlation between BVS and RV for the star ω CMa by plotting bisector velocity span against RV.

Correlation

To study the relationship between the bisector velocity span (BVS) and the radial velocity (RV), it is convenient to use correlation, which refers to the degree to which a pair of variables are linearly related. The correlation coefficient is defined as

$$\rho_{x,y} = \mathrm{corr}(x,y) = \frac{\mathrm{cov}[x,y]}{\sigma_x \sigma_y}, \tag{3.8}$$

where

$$\mathrm{cov}[x,y] = \mathrm{E}[(x - \mu_x)(y - \mu_y)], \tag{3.9}$$

cov means covariance; μ_x, the mean of x, i.e., $\mu_x = E(x)$; E stands for the expected value operator; σ_x is the standard deviation of x, i.e., the square root of the variance $E(x^2) - E(x)^2$; and equivalently for y. Specifically for observations (x_i,y_i) of the pair of random variables (x,y), $i = 1, \ldots n$, the observed value of the correlation coefficient $\rho_{x,y}$ is denoted by r, and is given by

$$r = \frac{\sum_{i=1}^{n}(x_i - \overline{x})(y_i - \overline{y})}{\sqrt{\sum_{i=1}^{n}(x_i - \overline{x})^2}\sqrt{\sum_{i=1}^{n}(y_i - \overline{y})^2}}, \tag{3.10}$$

where $r \in [-1,1]$ and $\bar{x}$ stands for the observed value of the mean of x, i.e., $\bar{x} = \frac{1}{n}\sum_{i=1}^{n} x_i$ (and equivalently $\bar{y}$). The correlation is positive if both values

increase together or negative if one value increases as the other decreases. If $r = 0$, two variables are uncorrelated; and if $r = \pm 1$, the perfect positive or negative linear correlation exists. The correlation coefficient is symmetric

$$\mathrm{corr}(x,y) = \mathrm{corr}(y,x). \tag{3.11}$$

Fig. 3.3 depicts examples of values showing how good the correlation is and whether it is positive or negative.

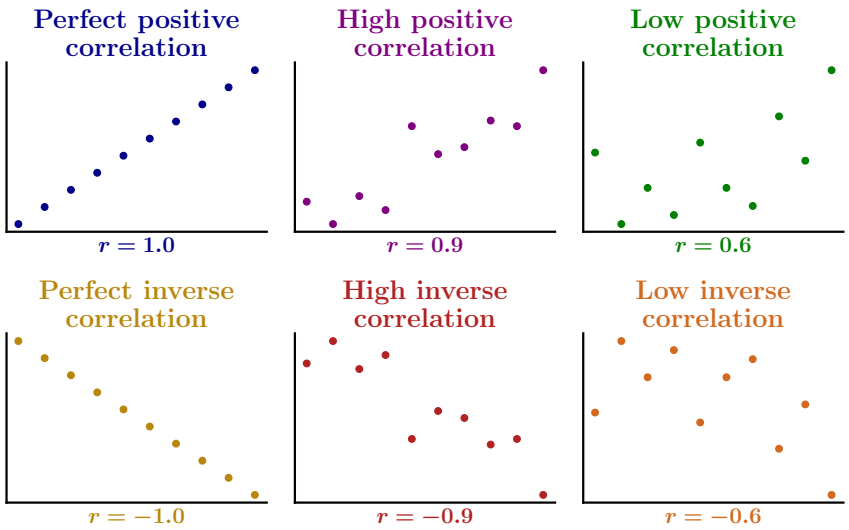

Figure 3.3: Basic types of correlation.

Application of the bisector method

The conjecture about ω CMa that the variation in the line asymmetry and RV correlates to the extent of the circumstellar envelopes was also tested by computing BVS and measuring RV. After determining these quantities, it was possible to study the trends between spectral line shapes, or bisectors, and RVs with the aim to search for a correlation between them. The higher correlation would be determined, the more likely the conjecture would be true.

I implemented the bisector method in the program `The_bisector_method.pro`[2] using the IDL programming language. The program displayed in Fig. 3.4 calculates bisector lines and the corresponding bisector velocity spans (for an individual data file with plotting or for multiple data files with saving to an output file), allows the inclusion of measured RVs, and determines the correlation coefficient between

[2] Available at https://github.com/BetkaOpl/The-bisector-method

BVS and RVs (see Fig. 3.5). The user has to choose relatively (in percentages – for instance, 80% and 20%) the top and bottom zone placement, the relative width of zones, and the central wavelength.

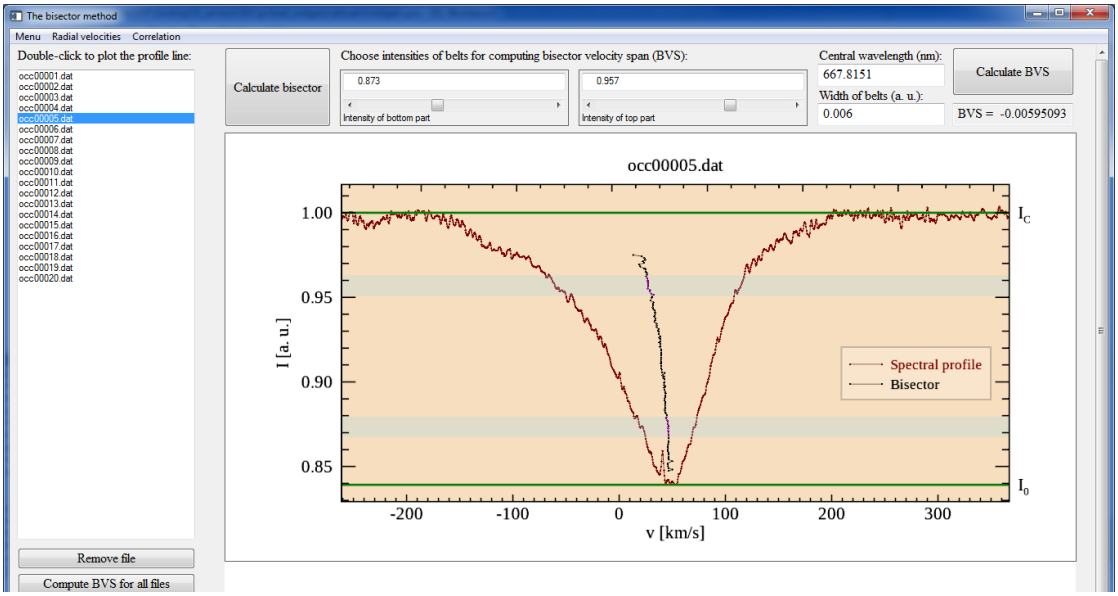

Figure 3.4: The program `The_bisector_method`.

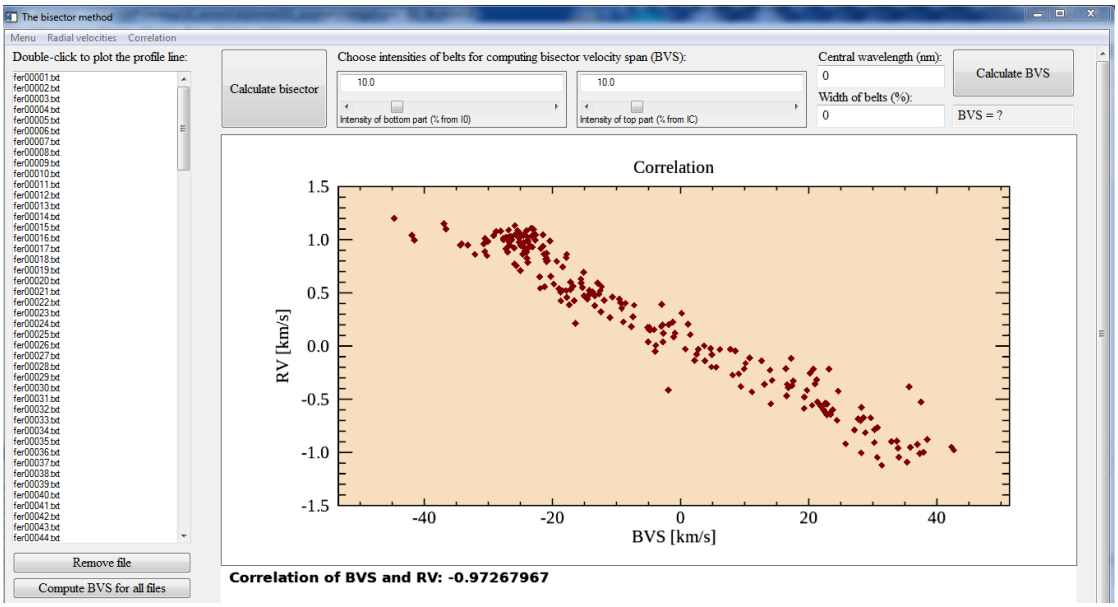

Figure 3.5: The computaion of correlation in the program `The_bisector_method`.

3.2 Data

For the analysis of the star ω CMa, I used spectroscopic data. Tab. 3.2 lists RVs adopted from the literature. Tab. 3.3 shows spectra including two spectral lines: He I 6678.515 Å and H_α 6562.79 Å, from which I derived several quantities. These spectra were kindly provided by Drs. Thomas Rivinius and Dietrich Baade. 275 CES red spectra obtained at ESO (La Silla) between 11th September, 1994 and 18th January, 1996, were studied byŠtefl et al. [2000] and published in JAD. Then, he put this data at the disposal of astronomical community. The time distribution of observations is shown in Fig 3.9. Some details about instruments, observatories, and measurements follow.

Table 3.2: The journal of RVs for ω CMa.

Instrument	**Observatory**	**Time**	**Number of RVs**
1.52-m reflector	ESO La Silla	1970–1983	79
coudé feed 1.0-m	Kitt Peak National Observatory	1975–1976	17
1.23-m telescope	Catar Alto	1977	14
1.4-m CAT	ESO La Silla	1982–1983	20

Table 3.3: The journal of spectra for ω CMa.

Instrument	**Observatory**	**Time**	**Number of spectra**	**Lines**
CES/CAT	ESO La Silla	1994–1996	275	He I
HEROS	ESO La Silla	1996–1997	224	He I, H_α
FEROS	ESO La Silla	1999–2002	228	He I, H_α
RETICON	Ondřejov	Feb. 2000	1	He I, H_α
2.1-m telescope	San Pedro Mártir	Oct. 2001	4	H_α

Table 3.4: The journal of the strength of the H_α emission line and its equivalent width.

T [RJD]	$(V+R)/2$ [u. of loc. con.]	EW [Å]	Source
45226.5	3.745	-	Hanuschik et al. [1988]
44923.5	-	-7.17	Dachs et al. [1986]
44951.5	-	-10.6	
45029.5	-	-11.8	
45394.5	-	-9.98	
43540.5	-	-14.2	Dachs and Wamsteker [1981]
43813.5	-	-12.9	
45195.5	3.6	-	Slettebak et al. [1992]
47806.5	5.1	-	
46835.5	5.5	-19.2	Dachs et al. [1992]
44921.8	2.6	-	Hanuschik et al. [1996]
45413.6	3.4	-	
46835.7	5.54	-	
47533.5	5.9	-	
48633.5	3.3	-	
49095.5	3.2	-	
51230.0	6.75	-18.6	Banerjee et al. [2000]

The 1.52-m reflector, ESO

The 1.52-m reflector, La Silla, was decommissioned in October 2002. It was a twin of the 1.5-m telescope at the Observatory de Haute Provence in France. It was mounted in an English cradle. The reflector was replaced by The Boller & Chivens spectrograph and by the FEROS spectrograph.

The radial velocities were originally published by van Hoof [1975] and remeasured by Baade [1982a]. The dispersion of measurements is 12.3 Å/mm.

The coudé feed 1.0-m, Kitt Peak National Observatory

Founded in 1958, the Kitt Peak National Observatory (KPNO) in Arizona in the Sonoran Desert is one of the largest assembles of astronomical instruments in the Northern hemisphere (more than twenty optical telescopes and two radio telescopes). These RVs were published by Abt and Levy [1978] and have a dispersion of 16.9 Å/mm.

The 1.23-m telescope, The Calar Alto Observatory

The Catar Alto Observatory in Spain on Calar Alto was established in 1970. The 1.23-m telescope is one of the four main telescopes of the observatory and was the first telescope of this observatory. RVs from this telescopes were published by Baade [1982a]. The spectra have a dispersion of 42 Å/mm.

CES, ESO

The ESO Coudé Echelle Spectrometer (CES) is attached to the alt-alt mounted 1.4-m Coudé Auxiliary Telescope (CAT) located at La Silla Observatory in Chile. It was housed in a smaller dome and fully computer-controlled. The linear dispersion is 1.91 Å/mm, and the signal to noise ratio was usually between 320 and 420.

All spectra [Štefl et al., 2000] were obtained by remote control from ESO Headquarters in Garching bei München and reduced with the standard ESO-Midas software package. The data set includes 11 spectra from 1994, November 11-15, and 264 spectra from 1996, January 11-18. In 1994, a Loral 2048 × 2048 pixel CCD with a spectral resolution of 60 000 and the length of the spectral interval 59 Å were used. In 1996, the CAT used a Loral 2680 × 512 pixel CCD, which had spectral resolution of 65 000 and a spectral interval length of 74 Å.

HEROS, ESO

An echelle spectrograph HEROS (Heidelberg Extended Range Optical Spectrograph) with resolving power of $R = \lambda/\Delta\lambda \approx 20000$ was used in HEROS Be Star Campaigns [Štefl and Rivinius, 2000]. The 0.5-m telescope at the La Silla observatory in Chile was attached.

Usually, one to ten spectra per night were obtained depending on the importance of the phase. Observations were obtained in 1996, January–May; 1997, January, March, and April; and one spectrum is from May 1999.

RETICON, The Ondřejov Observatory

RETICON was an electronic detector with a linear dispersion of 17 Å/mm attached to the 2.0-m reflector (Perek telescope) at the Ondřejov Observatory (established by Josef Jan Frič in 1898). It was provided by the Lick Observatory and installed in 1992. In 2000, the detector was replaced by the HEROS spectrograph.

The data set includes only one spectrum from RETICON obtained on 1st February 2000. It was observed by P. Harmanec and M. Tlamicha.

FEROS, ESO

The FEROS instrument [Kaufer et al., 1999] – the Fiber-fed Extended Range Optical Spectrograph – is a an astronomical Échelle spectrograph with high-resolution $R = \lambda/\Delta\lambda = 48000$ working from October 1998. It was attached to the 1.52-m telescope located at ESO's La Silla Observatory in Chile. In October 2002, the spectrograph was installed on the 2.2-m telescope.

Several spectra were obtained in January 1999; January 2000; two spectra in October 2001; 127 spectra from January 3-4, 2002; and three spectra from the remainder of 2002.

The 2.1-m telescope, National Astronomical Observatory (Mexico)

The 2.1-m telescope on Sierra de San Pedro Mártir mountain was constructed by Owens-Illinois, Inc at the end of the 60s. It has been in use since 1979. The Manchester Echelle spectrometer (denoted by MES-SPM) is attached to the telescope.

In the data set, there are four spectra from October 2001. They were measured with the spectrometer having a grid with 31.6 slits per mm.

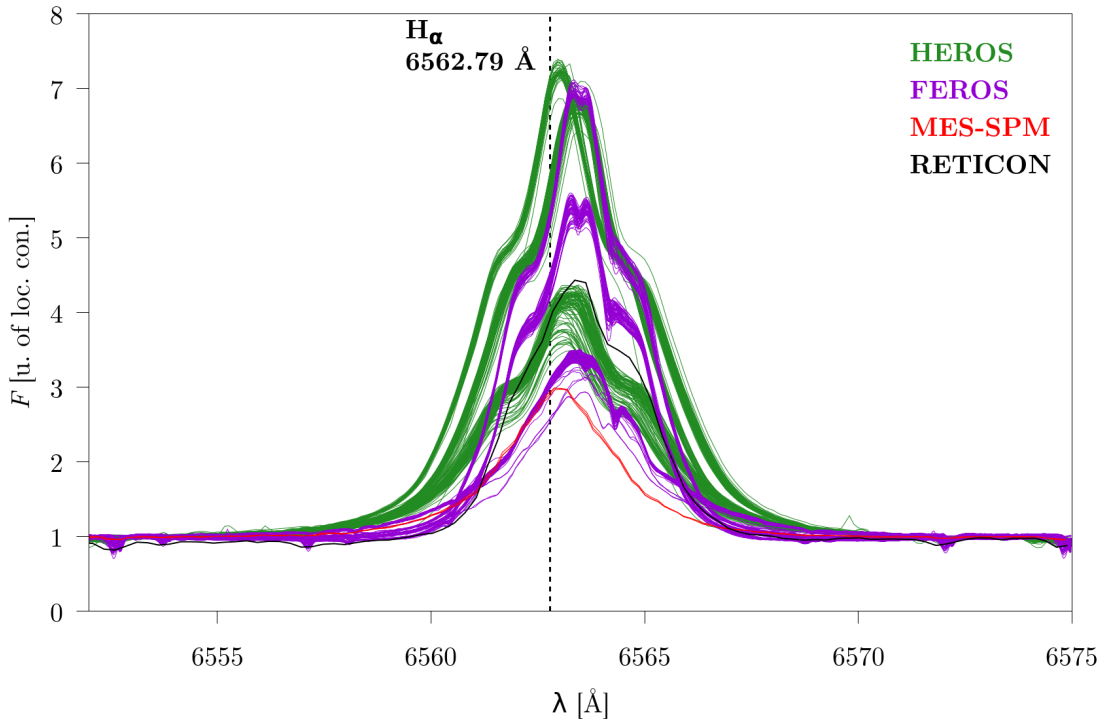

Figure 3.6: All H_α emission lines of ω CMa.

3.3 Spectral analysis of the star ω CMa

As already mentioned in Chapter 3, [Harmanec, 1998] conjectured that the exact local value of the 1.37 d period correlates with the extent of the circumstellar envelope. In order to verify it, I investigated the RV variations, line profile asymmetry, emission strength, and V/R ratio. To this purpose, I used two spectral lines from the red optical region: the absorption line He I 6678.151 Å and the emission line H_α 6562.817 Å. The former allows us to detect variations in RVs and asymmetry of line profiles. The latter originates in the circumstellar envelope and allows us to estimate the extend of the circumstellar envelope through its intensity. The line can be characterized by the strength of emission and by the V/R ratio. To analyse the variations in RV and line asymmetry described by BVS, I used the $O-C$ method and for BVS also the bisector method. The strength of H_α line and the V/R ratio can be measured directly from spectral line profiles.

With a wavelength of 6562.817 Å, the H_α line in the Balmer series appears as a line in the red portion of the visible spectrum. It appears when a hydrogen

electron passes from the third to the second energy level[3]. This line is the brightest hydrogen line in the visible electromagnetic spectrum. For Be stars, the H_α line profile often shows a double-peaked structure (see Fig. 3.7). In this case, we can measure the ratio of violet to red intensity peaks, V/R.

The emission line He I 6678.151 Å originates from the transition of an electron from a higher energy level $n > 2$ down to the $n = 2$ energy level. The energy of this line is close to that of the H_α line emission in the Balmer series; thus, it represents an important spectral line indicating many features of stars. For this reason, Be type stars can exhibit He I quite strongly, and the He I 6678.151 Å line is likely to be one of the strongest lines one can observe. Therefore, changes in RVs and line asymmetry are quite pronounced.

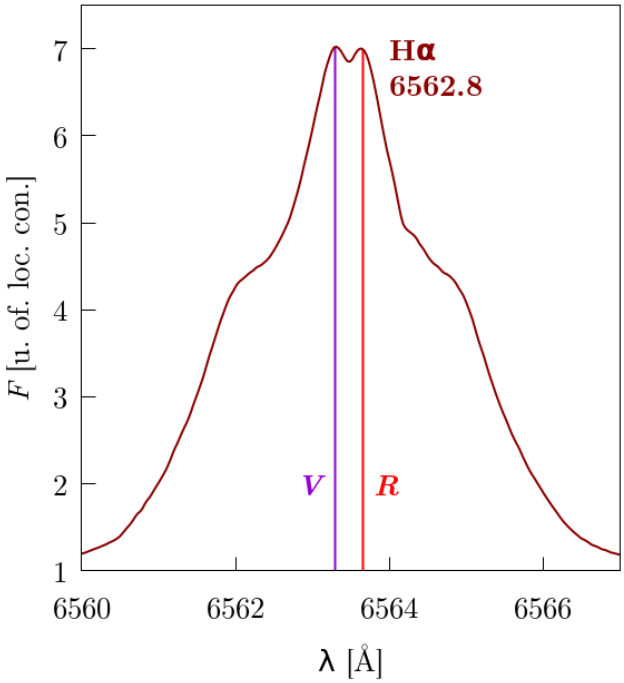

Figure 3.7: A H_α line with a double peak.

[3]Assuming the Bohr model of the atom, quantised energy levels around the atom's nucleus are characterised by the principal quantum numbers n. The Balmer series is the set of transitions from $n \geq 3$ to $n = 2$. The first lines are called H_α, H_β, H_γ, etc. for transitions from $n = 3$ to $n = 2$, $n = 4$ to $n = 2$, $n = 5$ to $n = 2$, etc., respectively. Likewise, the Lyman series is the set of transitions from $n \geq 2$ to $n = 1$, and they are denoted by Greek letters in a similar way: Lyman-alpha stands for the transition from $n = 2$ to $n = 1$; Lyman-beta, for $n = 3$ to $n = 1$, etc.

I have the following data sets at my disposal:

- 130 published RVs measured at the core of the He I 6678.151 Åfrom 1970 to 1983, [Harmanec, 1998]
- 728 RVs of He I 6678.151 Åfrom electronic spectra (CAT, HEROS, FEROS, and RETICON) observed from 1994 to 2003 that I measured using the program `reSPEFO2`[4],
- 453 spectra from HEROS, FEROS, and RETICON covering the H_α line
- 4 spectra from OAN[5] obtained with the 2.1-m telescope covering the H_α line.

For more information about the data, see Chapter 3.2. First of all, I rectified the spectra in the vicinity of all used lines. From H_α line, I have measured the intensity of the spectra in double peak V/R – the violet and red parts – and the strength of the H_α emission line as $(V + R)/2$. From He I 6678.515 Å, I have measured RVs at the core of the line. All these measurements were accomplished using the program `reSPEFO2`. For He I 6678.515 Å, I have also investigated assymetry for all lines using the program `The_bisectror_method` for the determination of bisector velocity span BVS.

Variations in RV and the $O - C$ method

I measured RVs at the core of He I 6678.151 Å using the program `reSpefo2` and also used the RVs from Harmanec [1998] (see Fig. 3.8). I first determined the mean period of RV changes using the phase dispersion minimisation method (PDM) described in Chapter 3.1.1. As Fig. 3.8 shows, there are obvious systematic shifts in phase for data from various data sets. To investigate this on a quantitative basis using the standard $O-C$ analysis, I grouped RVs into local subsets covering usually about 7 days (see table in Att. A.3). The group 17, which consists of only 5 RV points and which gives heigher uncertainty than other groups. Also, this group does not give a reasonable phase curve with the period of 1.372094 d. For each group, I determined the epoch of the maxima of the RVs, amplitude K, and γ velocity) using the program `SPEL` (SPectroscopic ELements)[6] with $e = 0$, $\omega = 0$, and fixed period. Since the amplitude of the 1.37 d RV changes may undergo real secular changes and also depends on the spectral resolution of different

[4]The program `reSPEFO2` was written by Adam Harmanec and is available along with a user manual at https://astro.troja.mff.cuni.cz/projects/respefo/

[5]The National Astronomical Observatory (*Observatorio Astronómico Nacional de San Pedro Mártir*), Baja California, Mexico

[6]The program was written by Dr Jiří Horn and used, for example, in Horn et al. [1994, 1996]

spectrographs used, I normalized all RVs from the interval $(K-\gamma, K+\gamma)$ to the interval (-1, 1) using the program `hec13` written by Petr Harmanec.

The time plot of normalised RVs shown in Fig. 3.9 uses data which span an interval over thirty years. The error bars in the figure for $T > 47500$ RJD are those determined by the program `reSPEF02` – root mean square defined as

$$x_{\mathrm{RMS}} = \sqrt{\frac{1}{n}(x_1^2 + x_2^2 + x_3^2 + \cdots + x_n^2)}, \tag{3.12}$$

where x_i stands for measurements and n for the number of measurements. Each value was measured independently three times, i.e. $n = 3$. The RV curve from HEROS has the most significant measured uncertainties because of lower resolution, compared to the points from CAT and FEROS. The error bars for $T < 47500$ RJD are estimated according to weights assigned by observers and listed in paper Harmanec [1998]. For 858 measured coupled pairs of time (40607.5399–52339.5096 RJD) and normalised RV, I applied the PDM method implemented in program `hec27`. Five phase bins and two representations were used for searching a period in the range from 1.3 to 1.5 with phase difference 0.1. To determine the uncertainty, I apply the bootstrap method described in Chapter 3.1.2. The Stellingwerf method (the program `hec27`) was used 50 000 times for 858 randomly chosen samples – the `bash` script enabling this is in Att. 2. The resulting value of the period is $P = (1.372094^{+0.000015}_{-0.000010})$ d, where the uncertainty is the confidence interval of 95% from the histogram. Figs. 3.10, 3.11, and 3.12 display $\Theta(f)$ resulting from the Stellingwerg method, the histogram from the bootstrap method, and all RV points against phase with the determined period, respectively.

Then, I carried out the same procedure (applying Stellingwerf's method and the bootstrap method) with RVs measured for $T < 47500$ RJD and $T > 47500$ RJD. The dashed line indicates these two parts on Fig. 3.9. Figs. 3.13, 3.14, and 3.15 display theta statistics resulting from the Stellingwerg method, histograms from the bootstrap method, and all RV points against phase with the determined period, respectively. The older data sets indicate a period of $(1.371938^{+0.000044}_{-0.000092})$ d, which differs by about 0.000032 d (within the uncertainty) from the period

$$P = 1.371906 \pm 0.000013$$

d determined by Harmanec [1998], who carried out the analysis on almost the same data. The newer data sets indicate a longer period of $(1.372049^{+0.000023}_{-0.000053})$ d, which is shorter than the period determined from all data sets. RV curves against phase on Fig. 3.15 are almost in anti-phase, which means that the mean period for all data is slightly different.

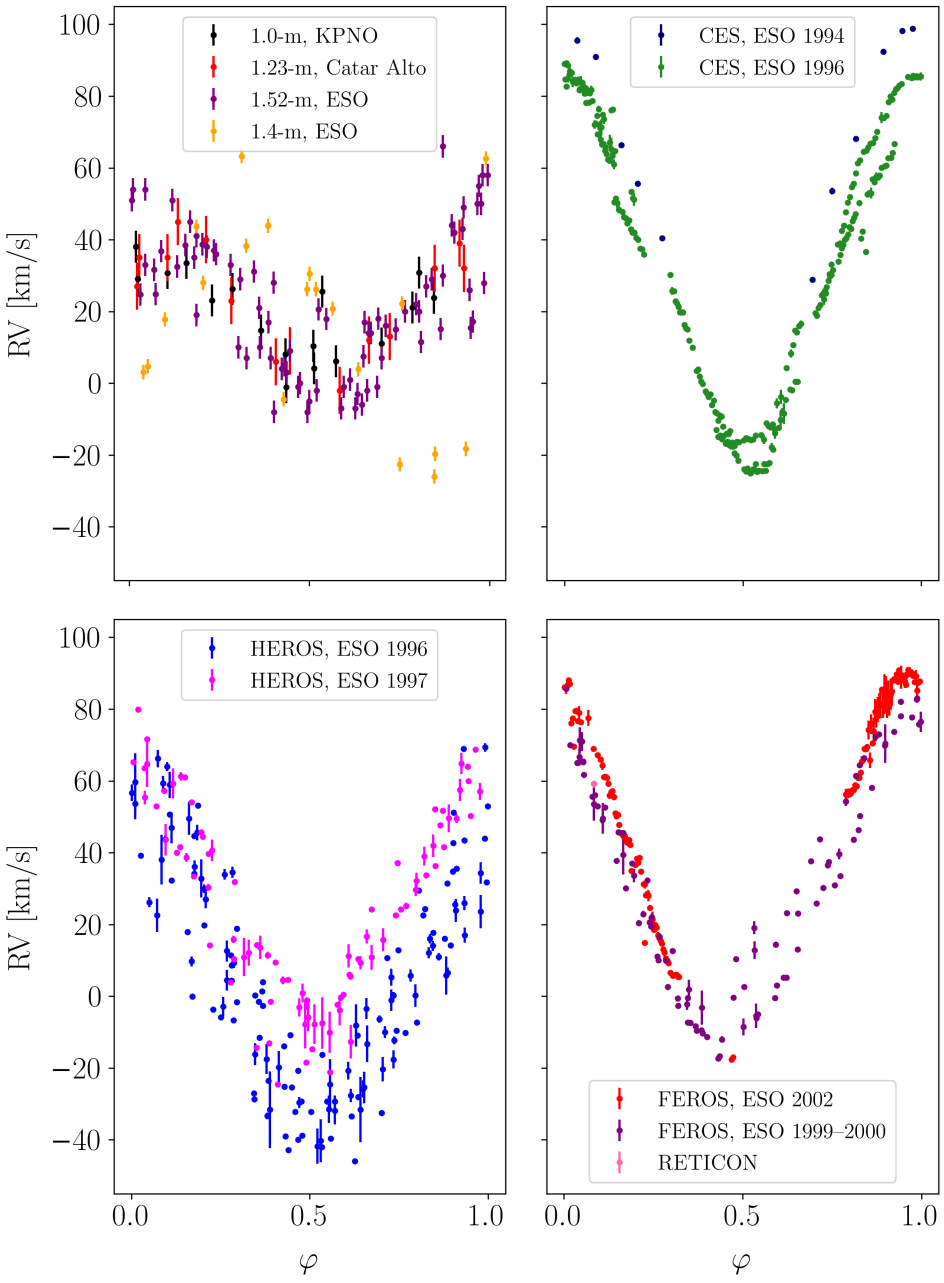

Figure 3.8: RV points from the literature (left top panel), measured RVs from CES (right top panel), measured RVs from HEROS (left bottom panel), and measured RVs from FEROS and RETICON (right bottom panel). All these phase curves are constructed with the mean determined period $P = 1.372094$ d.

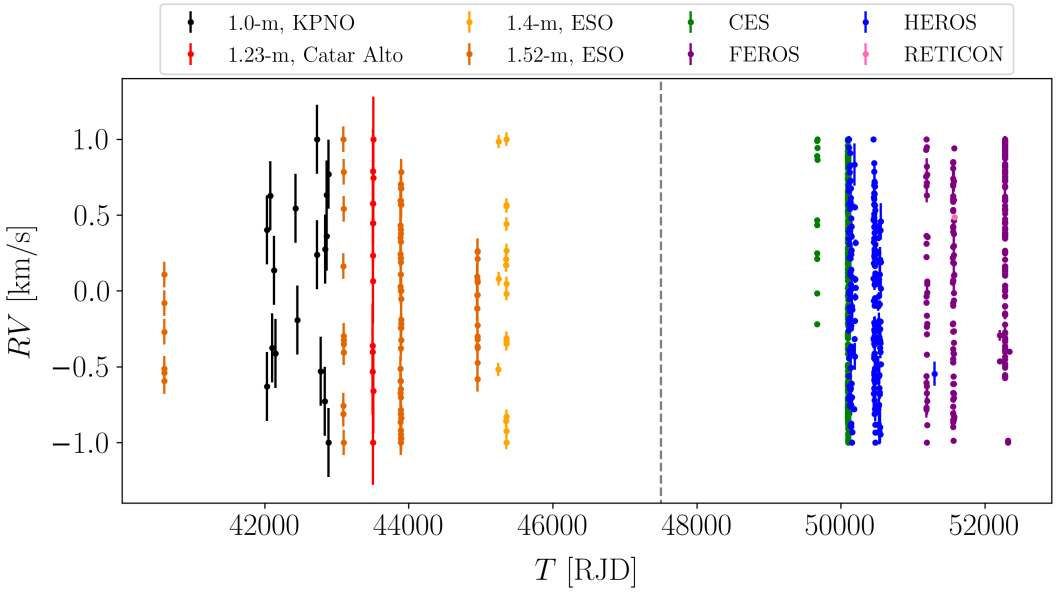

Figure 3.9: Normalized RV points against time.

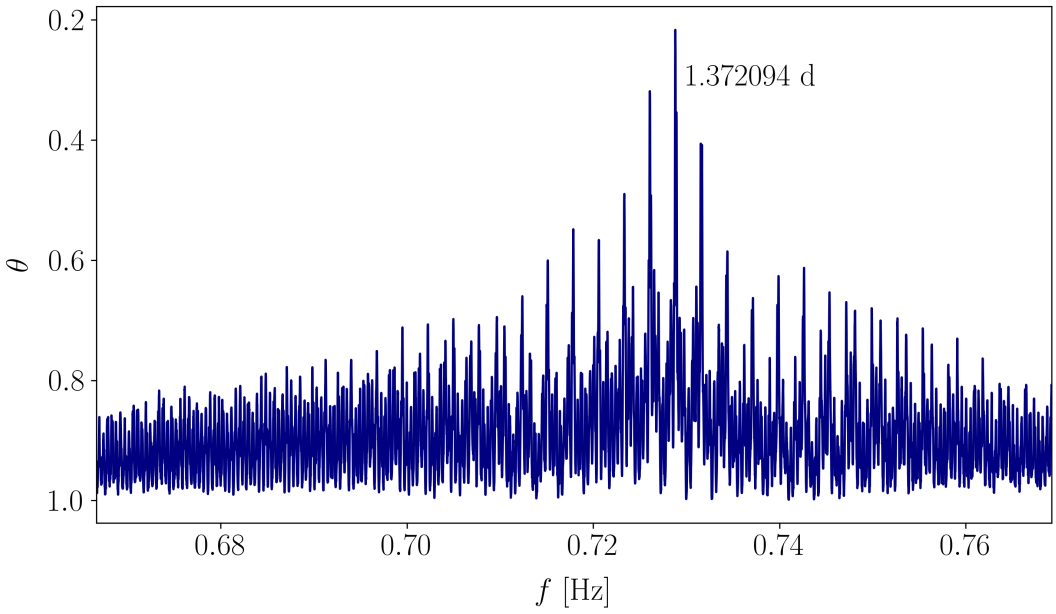

Figure 3.10: The periodogram from all RV points.

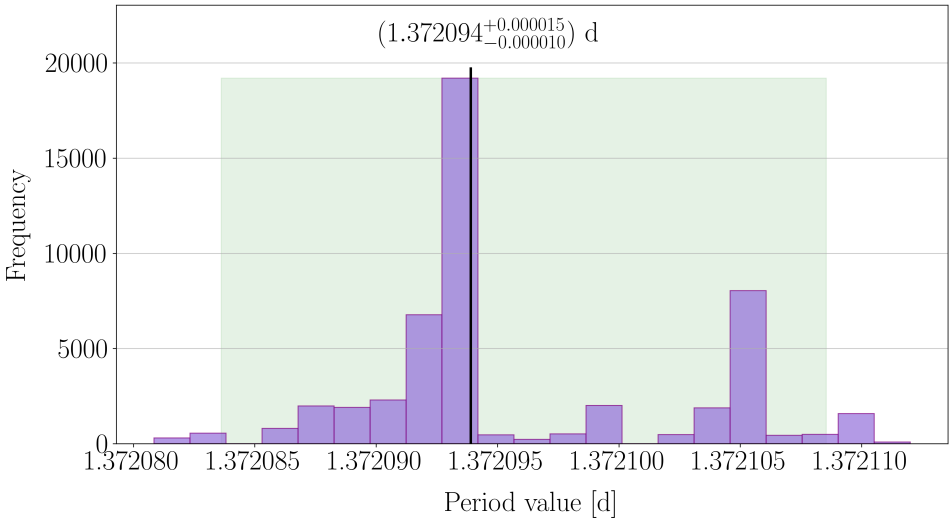

Figure 3.11: The histogram (20 bins) shows the results of the bootstrap method for the determination of an uncertainty of the mean period of RV changes. The green region is 95% confidence interval.

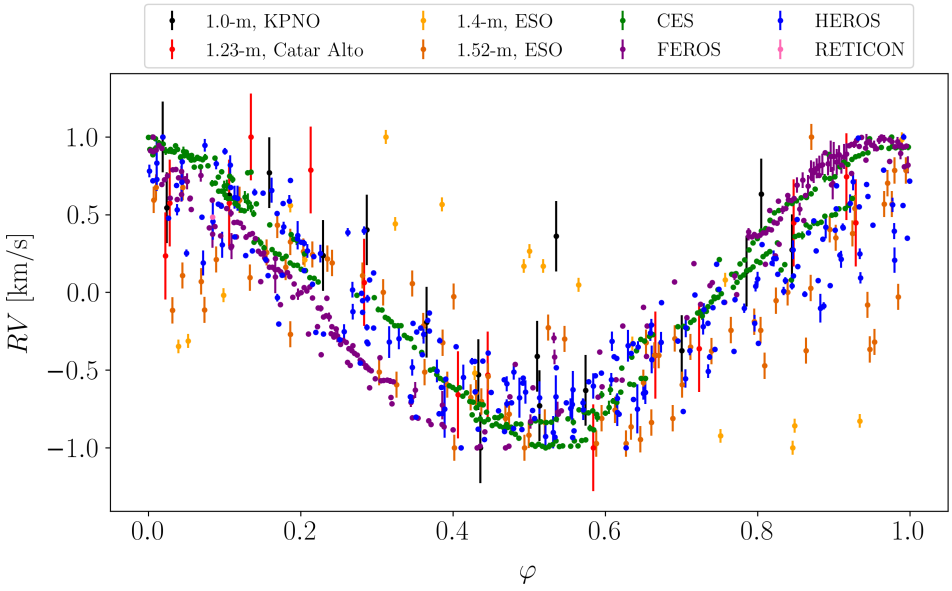

Figure 3.12: All RV points against phase ($P = 1.372094$ d).

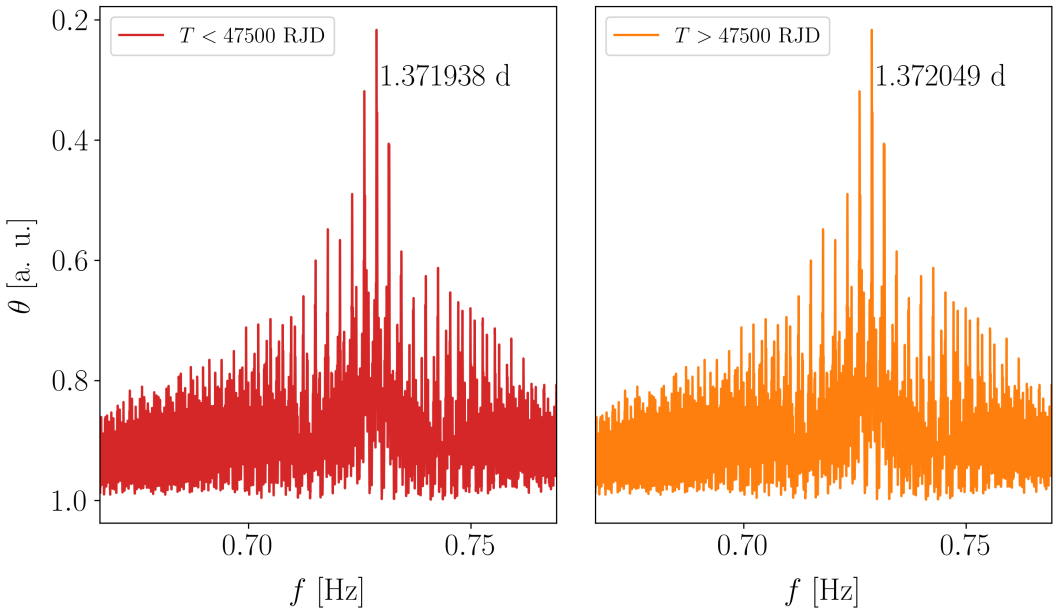

Figure 3.13: Periodograms for $T < 47500$ RJD and $T > 47500$ RJD.

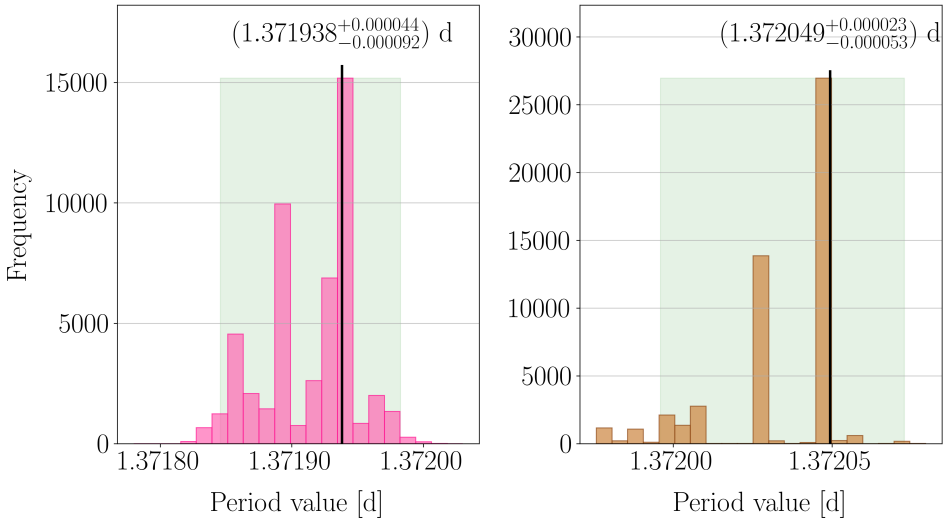

Figure 3.14: Histograms (20 bins) show the results of the bootstrap method for the determination of the uncertainties of the mean period for data $T < 47500$ RJD (left) and $T > 47500$ RJD (right). The green regions are 95% confidence intervals.

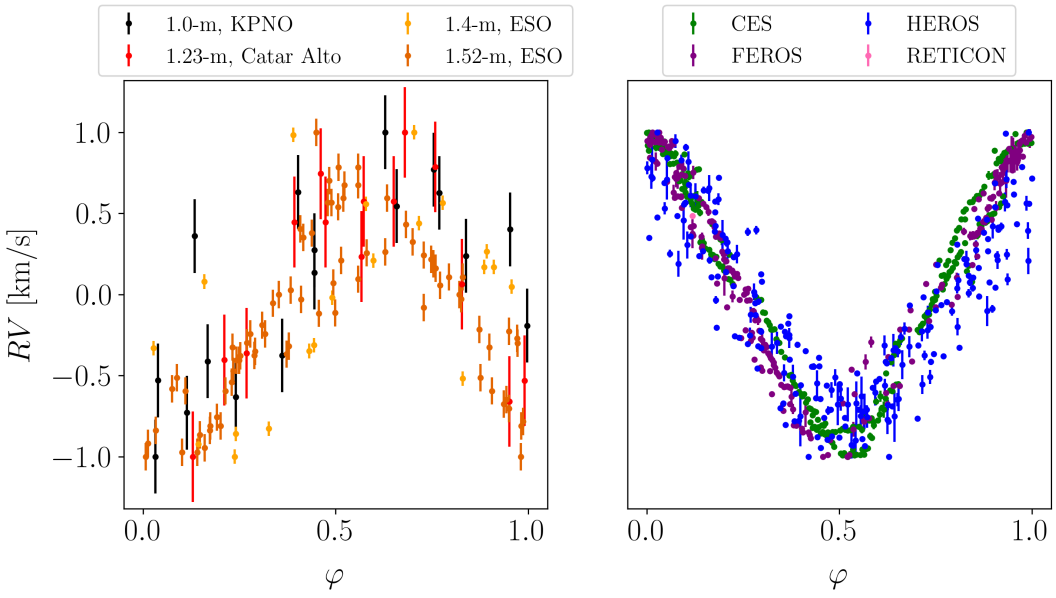

Figure 3.15: RV points determined for $T < 47500$ RJD and $T > 47500$ against phase with the period from periodogram 3.13.

To investigate the variations in RVs, I used the $O - C$ method, the classical method of accurately determining periods or estimating their values more accurately based on a previous, less accurate value. An early reference for this method is Gould [1882], who used it on the period of variable star R Hydrae. The method is described in detail by, for instance, Hoffmeister et al. [1985] and Percy et al. [1992]. The $O - C$ method is appropriate in this case since the time series of observations include gaps in time and the measurement errors of measurements are more significant than autocorrelation, which is discussed by Lombard [1998].

The $O-C$ method uses an $O-C$ diagram of observed minus calculated values. Here, in order to determine whether there are variations in the RV in addition to the assumed periodic variation, we subtract *observed* local epochs of RV extreme and *calculated* linear ephemerides. If we assume an approximate value for the period, then the $O - C$ diagram can tell us about the true period in the following ways:

- If the $O - C$ points lie on a line parallel to the horizontal, then the assumed period is stable and accurate enough, and the true value of the period corresponds to the one assumed.
- If the $O - C$ points lie on a line with a negative or positive slope, then the

true period is stable and not equal to the assumed period. If the slope is negative, the assumed period should be less than the period assumed for constructing the $O-C$ diagram. If the slope is positive, the assumed period should be greater than the period assumed.

- If the $O-C$ points lie on a parabola with the axis parallel to the vertical axis, the assumed period is changing with time. If the parabola's minimum occurs at the reference epoch, the real period is increasing. If the parabola's maximum occurs at the reference epoch, the real period is decreasing.
- The $O-C$ points can also be fitted with a third- or higher-degree polynomial; however, the meaning is debatable. While such a polynomial fit may correspond with the recorded observations, a physical interpretation is lacking.
- If the $O-C$ points fit a periodic function, then a third object is present, or there is a changing eccentric orbit.
- If the $O-C$ points show low correlation, the true period changes erratically because of, for instance, eruptive processes, loss of mass, or mass transfer between companion stars.

For local solutions, I used again the program `SPEL`. The input to the program was the groups of around 7 consecutive days of observations. The period ($P = 1.372094$ d), eccentricity ($e = 0$), amplitude ($K = 1$ km/s), and argument of periastron ($\omega = 0°$) were fixed, while the epoch of the maximum of RV and the gamma velocity γ were adjusted to ensure that the equations relating the parameters are satisfied by the values of the parameters. The program derived the local circular-orbit solution at the epoch of the maximum of a velocity curve with a period of 1.372094 d. The result was a local epoch for all groups. In the next step, I computed $O-C$ deviations of these local epochs from the linear ephemeris of RV maxima T_{maxRV}, which satisfies the formula

$$T_{\mathrm{maxRV}} = T_0 + PE, \tag{3.13}$$

where T_0 stands for the reference epoch when the event – maximum of RV – occurred in the past; P for the period; and E for the number of times the event recurred. To obtain an estimate a number of times the event recurred, I used

$$\hat{E} = \mathrm{int}\left(\frac{T_{\mathrm{now}} - T_0}{P}\right). \tag{3.14}$$

Then, the O − C deviations can be computed as follows:

$$\mathrm{O-C} = T_{\mathrm{maxRV}} - T_0 - P\hat{E}. \tag{3.15}$$

The method is implemented in program `efem` written by Petr Harmanec. I used period $P = 1.372094$ d and $T_0 = 50095.8251$ RJD as the reference epoch for the maximum of the RV curve; this value comes from CES data, since this RV curve is completely covered and has good resolution. For all the maxima of the RV curves, I obtained the $O - C$ diagram displaying $O - C$ points with respect to time (see Fig. 3.26). The diagram clearly shows cyclic changes of the period.

Variations in the V/R ratio and the strength of the emission line

The next changes are in the V/R ratio and in the strength of the H_α emission line. To measure these quantities, I used the program `reSPEFO2` (see Fig. 3.16), which gives values of intensities for the violet peak V and the red peak R. From these values, the ratio V/R and strength of emission $\frac{V+R}{2}$ are determined. Some of the spectra have insufficient resolution to resolve the two peaks, especially the HEROS spectra. In this case, I measured only the strength of the emission. Fig. 3.25 depicts the measured V/R ratio and the strength of emission line $\frac{V+R}{2}$. The strength of the H_α emission line changes in the long-term time scale. To extend the time span, the strength of emission lines from literature were collected (see Tab. 3.4).

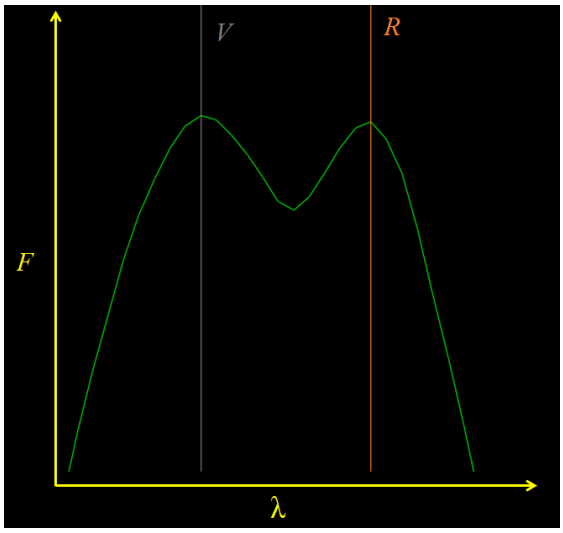

Figure 3.16: The ratio V/R measured in `reSPEFO2` using H_α line (FEROS spectrum).

Fig. 3.17 shows the V/R ratios plotted against phase from five nights that were sufficiently covered by measurements. The V/R ratio changes periodically in the same way as an absorption profile. The intensity of one wing is decreasing while the intensity of the other one is increasing. Then they switch roles.

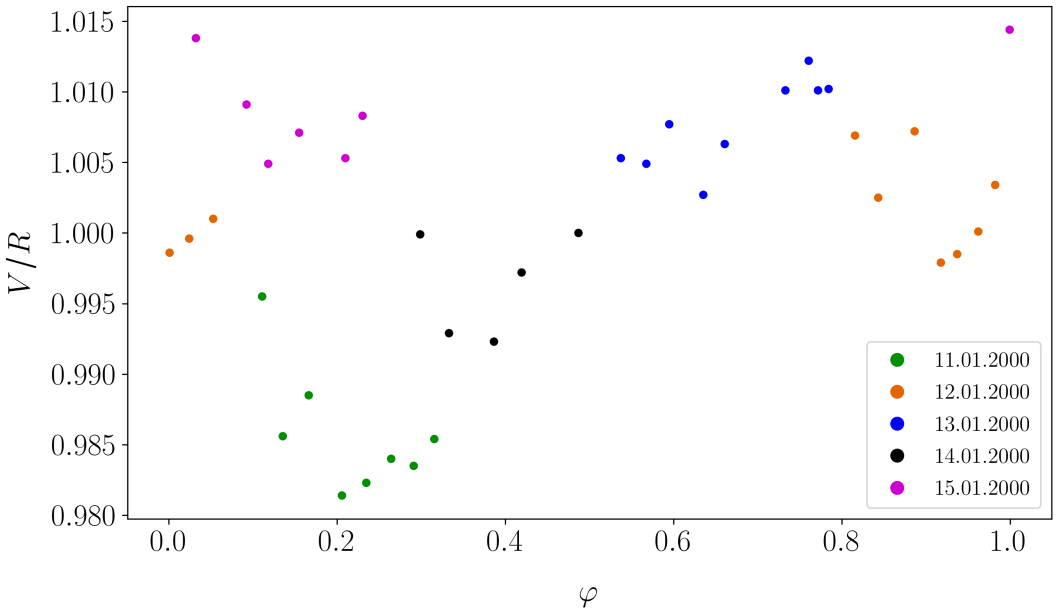

Figure 3.17: The V/R ratio in phase during five nights (FEROS spectra).

Assymetry of the helium lines

The striking feature of many absorption lines is their pronounced assymetries. Varying line profiles imply variable RVs of either wings, centres, or both. To investigate the assymetry of the helium lines He I 6678.151 Å, I used the bisector method, which provides a complete description of asymmetry in the spectral line profile. The method is described in section 3.1.3 and implemented in program `The_bisector_method`. All measured bisector velocity spans against time are in Fig. 3.18 and a few zooms for numerous data sets are in Fig. 3.19. Bisector velocity span against phase is plotted in Fig. 3.20. The phase shifting of different observational seasons arises due to changes in the period of variations in bisector velocity span with time. The figure is very similar to the plot in Fig. 3.12, but the phase is shifted about a half of an period because of the definition of BVS. As for RVs, the $O-C$ analysis can be performed using the programs `SPEL` and `efem`.

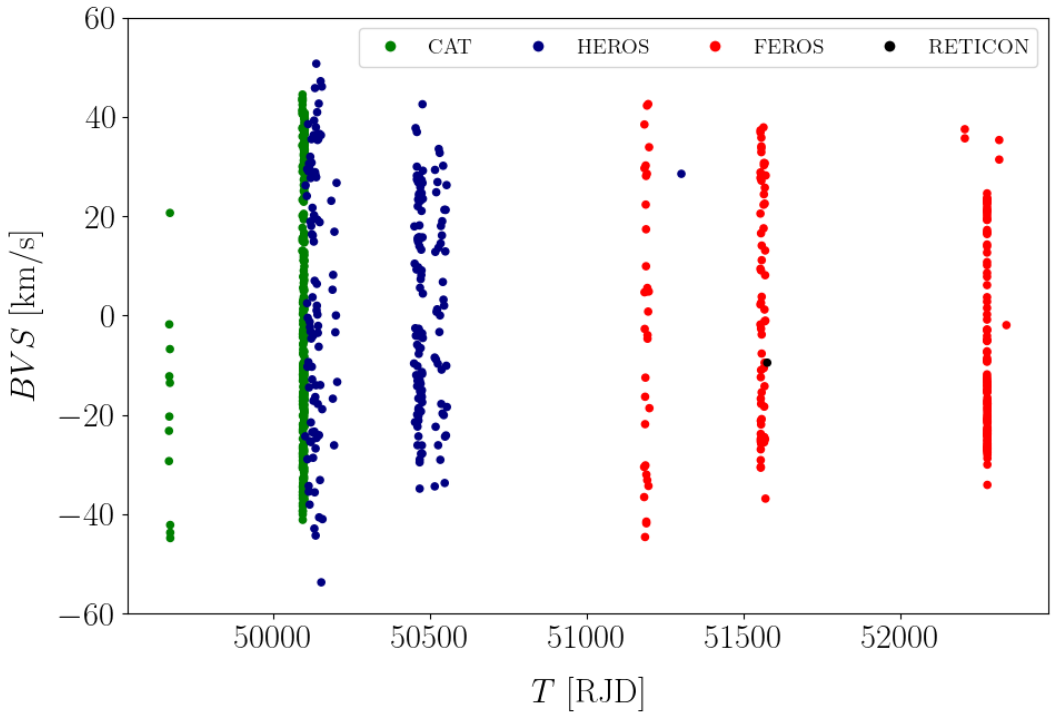

Figure 3.18: Bisector velocity span against time.

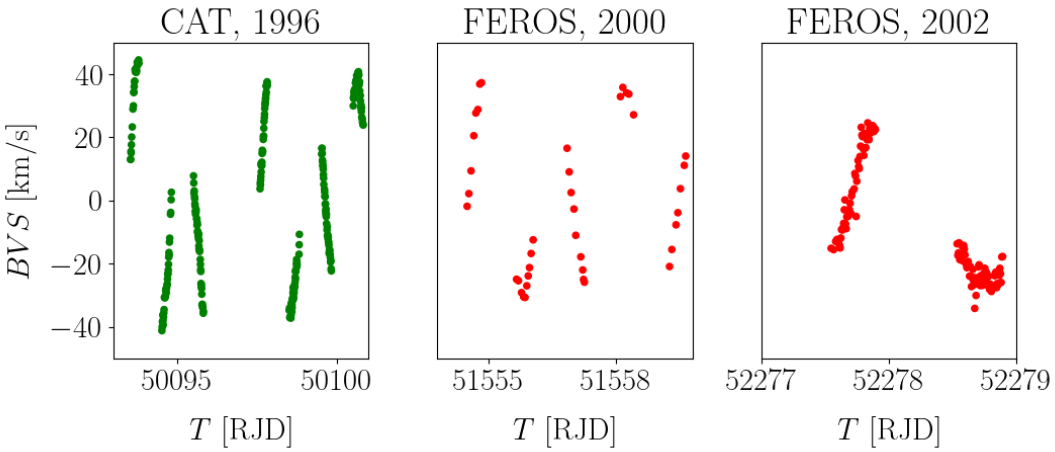

Figure 3.19: Bisector velocity span against time – numerous observations.

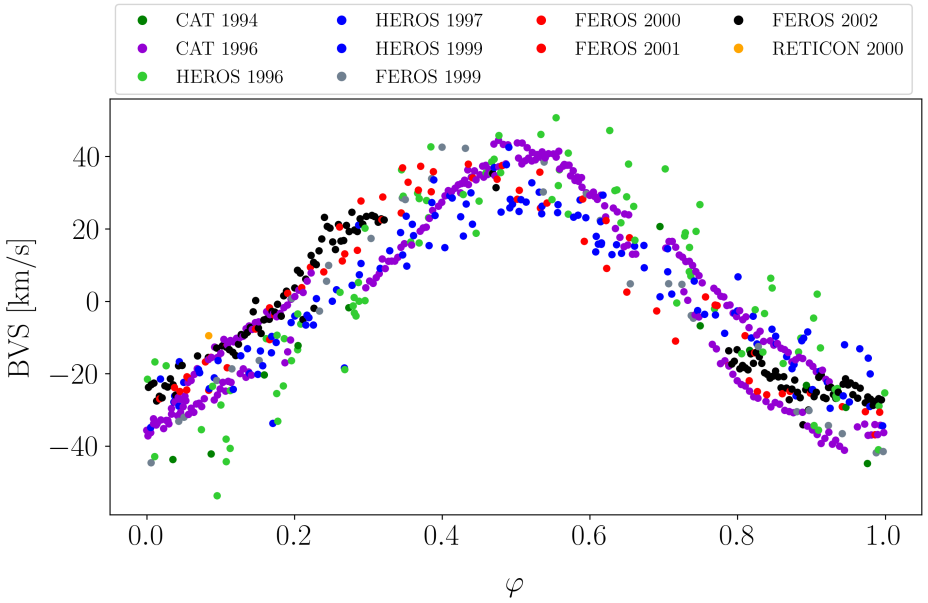

Figure 3.20: Bisector velocity span against phase.

3.3.1 Dynamical spectra

The changes with period of 1.372094 d was also verified by the python program `dynsp` kindly provided by Juraj Jonák. Figs. 3.21, 3.22, 3.23, and 3.24 depict the results for all spectra, CES spectra, HEROS spectra, and FEROS spectra, respectively. The changes are obvious in all figures. The differences are influenced by the resolution of spectra.

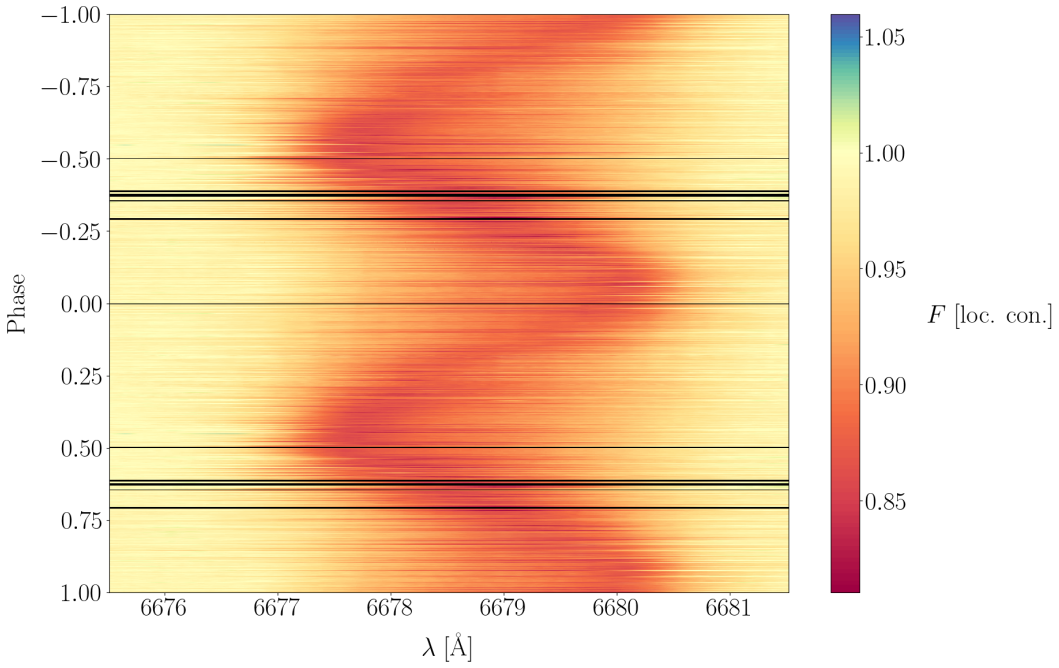

Figure 3.21: Dynamical spectrum for all spectra.

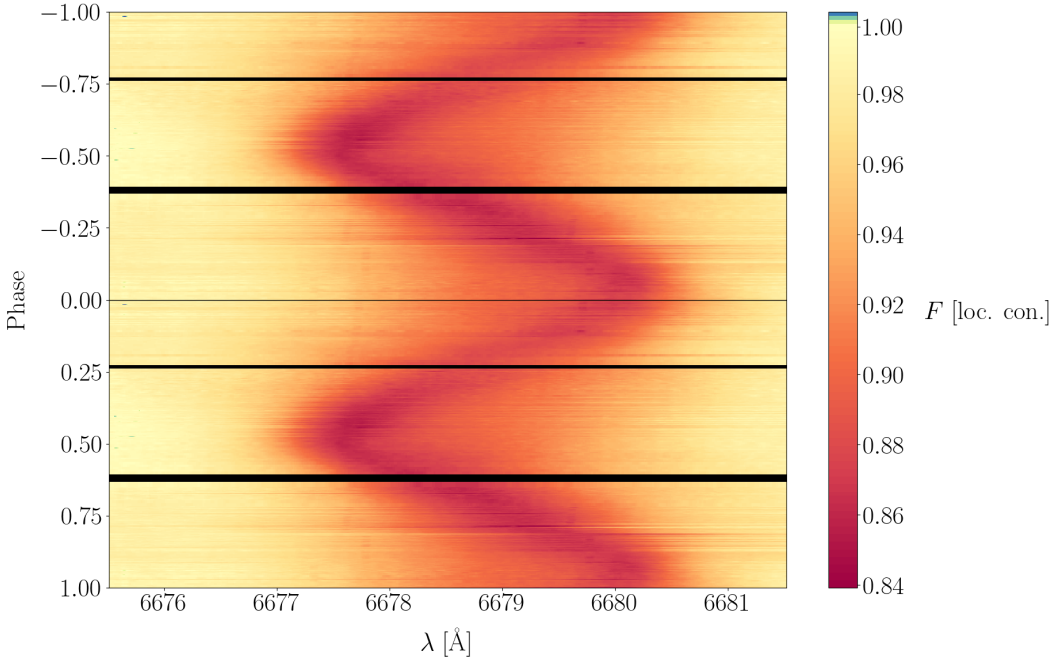

Figure 3.22: Dynamical spectrum for all CES spectra.

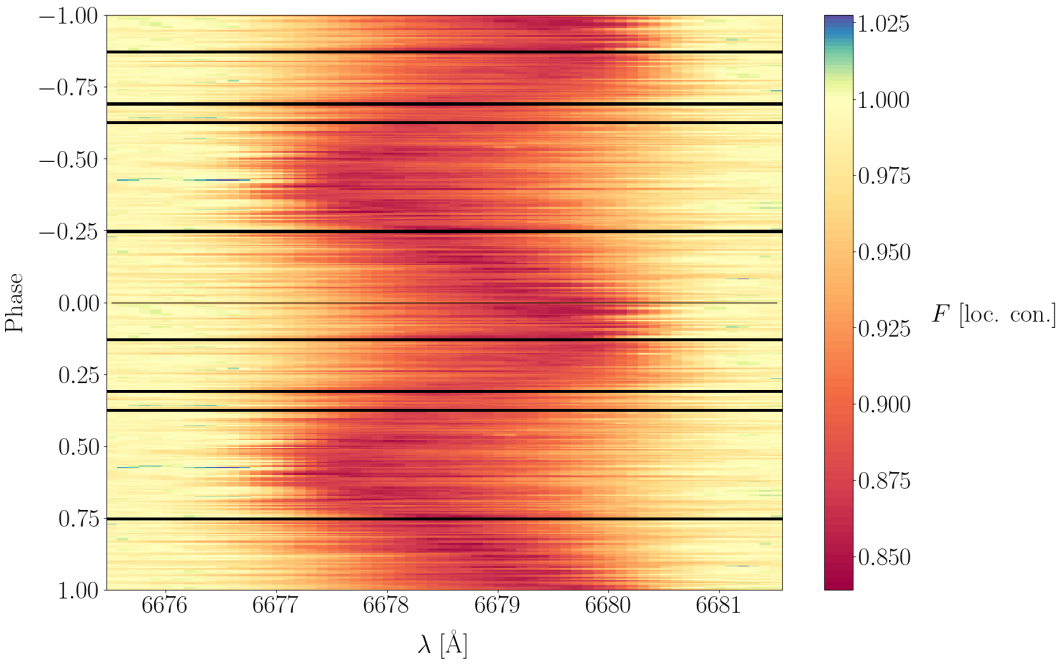

Figure 3.23: Dynamical spectrum for all HEROS spectra.

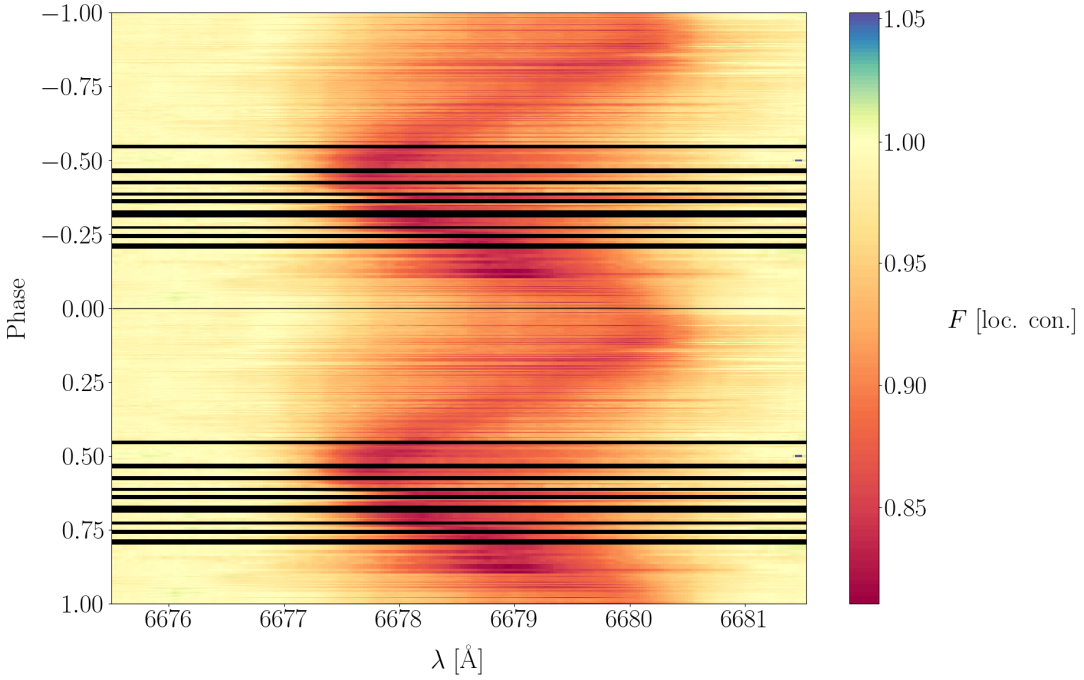

Figure 3.24: Dynamical spectrum for all FEROS spectra.

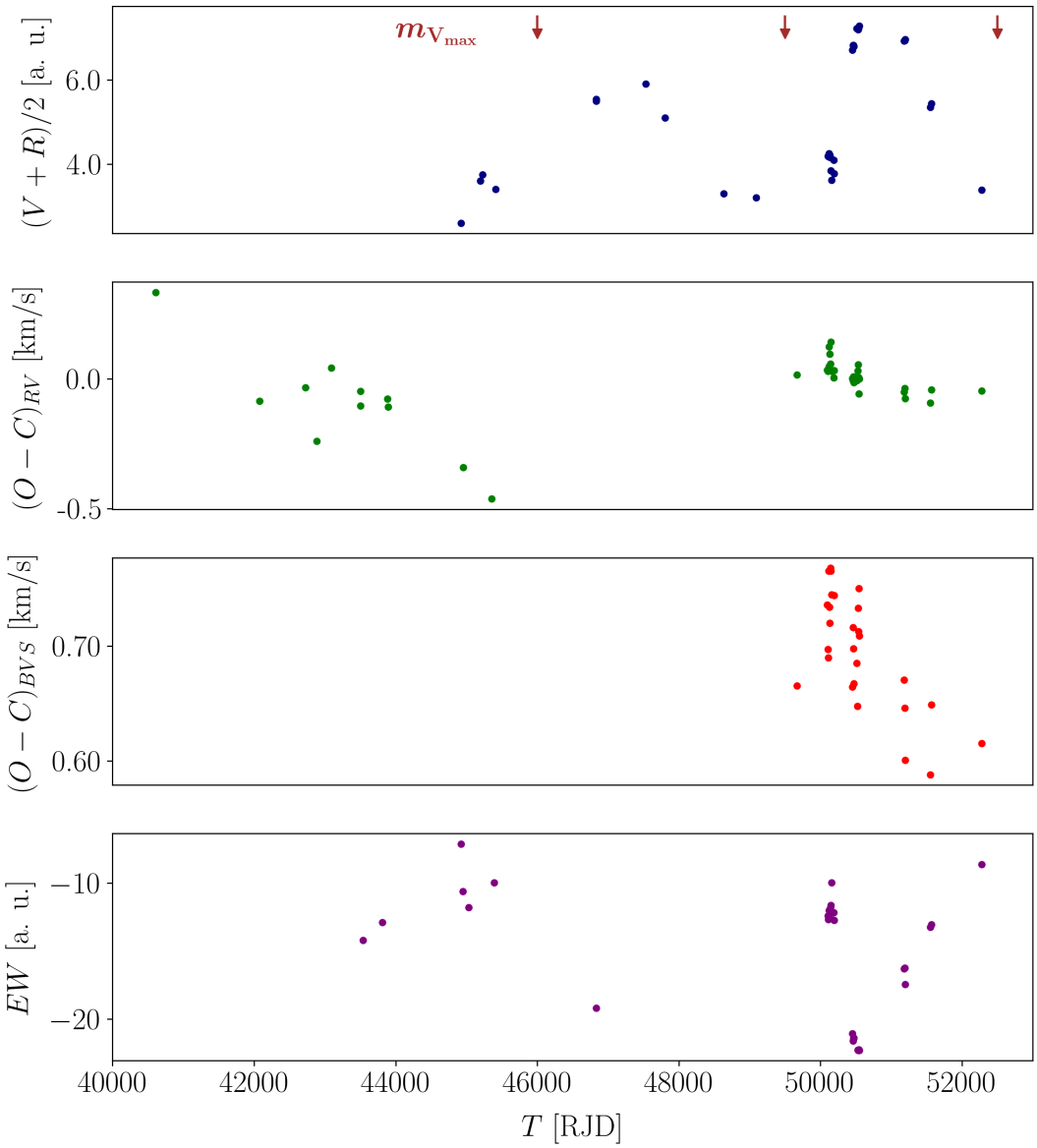

Figure 3.25: The comparison of the strength of the H_α emission line to $O-C$ determined from RV and BVS against time. $O-C$ residuals against time constructed for the local ephemeris subtracted from linear ephemeris. $T_{\mathrm{maxRV}} = \mathrm{RJD}\ 50095.8251 + 1.372094 \cdot E$. The brown arrows indicate the maxima of visual magnitude according to Ghoreyshi [2018].

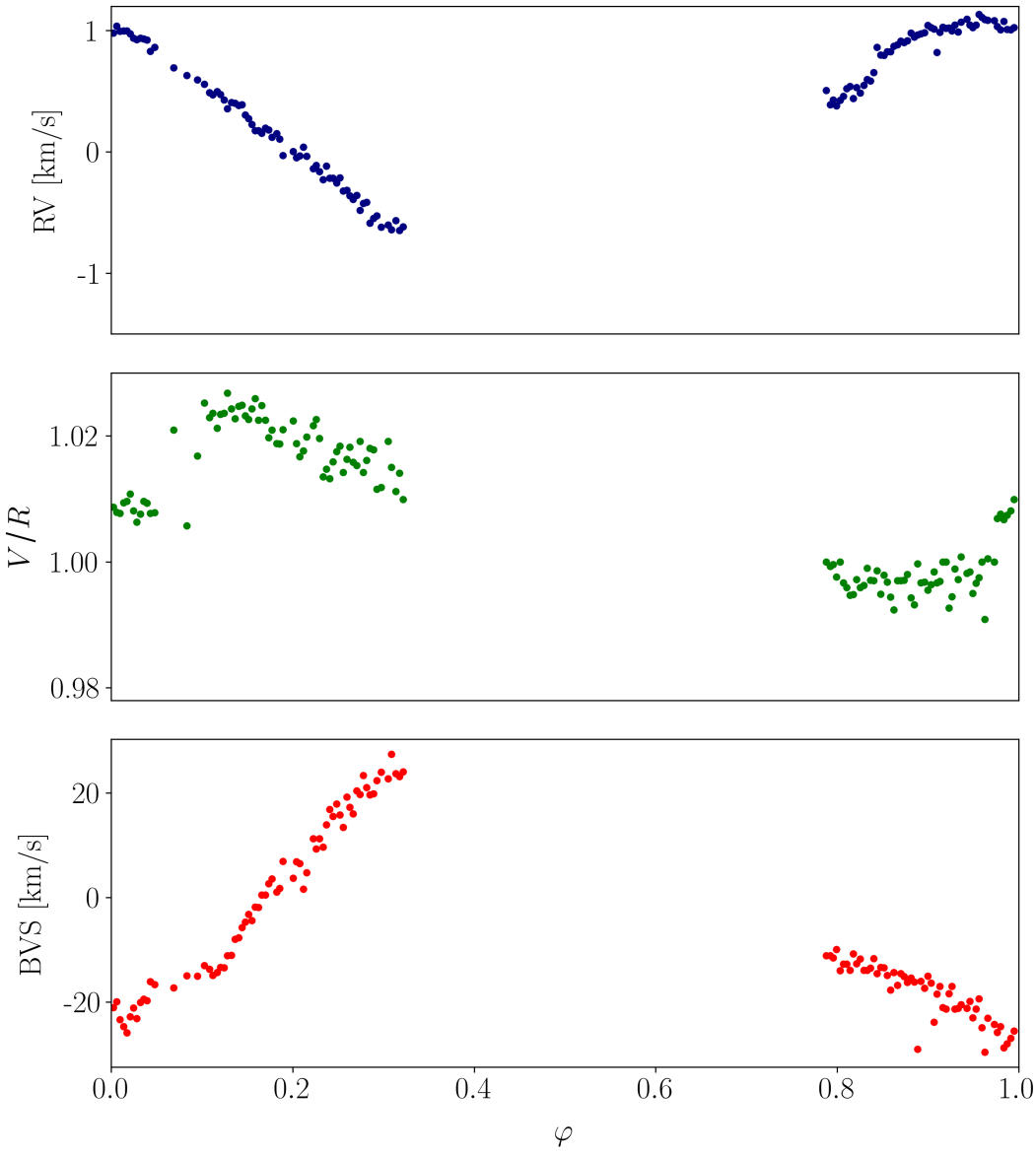

Figure 3.26: The omparison of RV, V/R, and BVS against phase determined from FEROS spectra that were obtained during two days – 3th January and 4th January, which were richly covered.

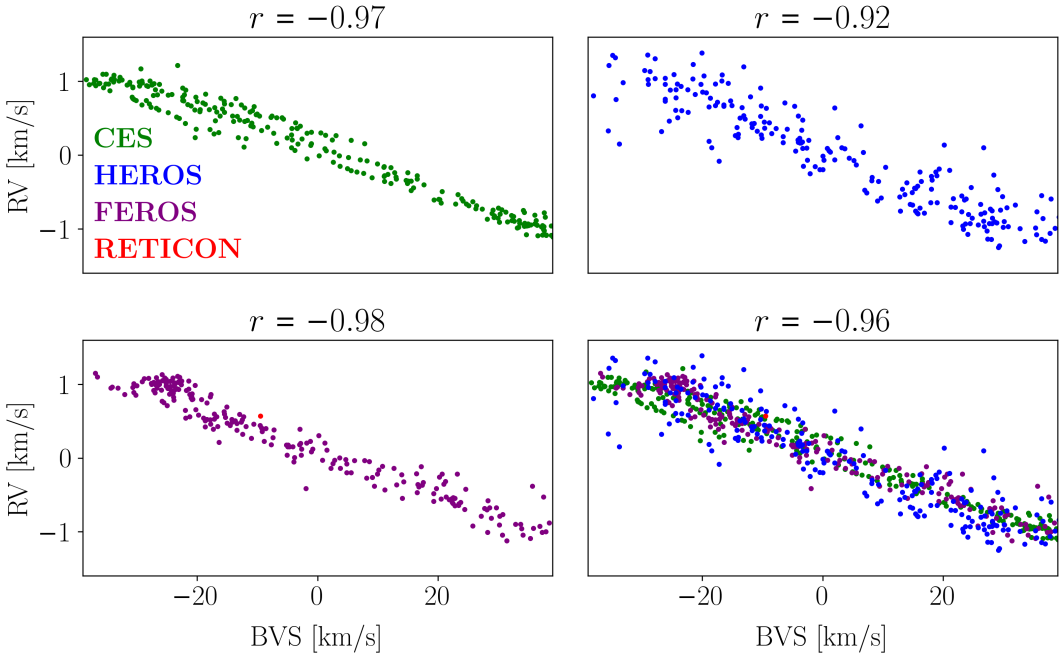

Figure 3.27: The correlation of RV with BVS for all data (left top), CES data (right top), HEROS data (left bottom), and FEROS data (right botoom).

3.4 Results and discussion

The aim was to find out whether the changes in period correlate to the extension of the circumstellar envelope. Its extension is characterised by the intensity of the emission in the H_α line arising in the corotating circumstellar envelope, while the changes of the period are characterised by $O-C$ diagrams constructed from RV and BVS. These two quantities are strongly correlated for CES and FEROS data (see Fig. 3.27). In the case of HEROS spectra, the correlation was not detected, since the resolution of HEROS data is not sufficient to determine this relationship.

Fig. 3.25 shows the comparison of the strength of the H_α line (measured in this thesis and adopted from the literature) to $O-C$ points constructed from radial velocities RV, and $O-C$ constructed from asymmetry BVS. It looks like there is a connection between these phenomena. They are shifted in phase, since the extent of the envelope starts, and then the brightness increases (emission lines are stronger). Although I have no data in the $O-C$ diagram for $46000 < T < 49000$, it is reasonable to assume there is another peak in that interval. Thus, the conjecture that the changes in period correlate with the strength of the H_α emission, which characterised its extent, seems to be proven. That means that the

period of 1.37 days is related to a corotating structure in the inner parts of the envelope, and any intrinsic changes in the exact value of the period ($\approx$ 1.37 d) depend on the presence or absence of the emission in the star's spectrum.

Fig. 3.26 compares V/R ratio, RVs and BVS in local – numerous FEROS data sets. If the RV measured at the core reaches its maximum, the violet wing is longer, and the BVS is less than zero. The relation holds vice versa.

The next result is the determination of the period of radial velocity changes from used data, namely, $(1.372094^{+0.000015}_{-0.000010})$ d. The older data sets indicate a period of $(1.371938^{+0.000044}_{-0.000092})$ d, which differs by about 0.000032 d (within the uncertainty) from the period

$$P = 1.371906 \pm 0.000013$$

d determined by Harmanec [1998], who carried out the analysis on almost the same data. The newer data sets indicate a longer period of $(1.372049^{+0.000023}_{-0.000053})$ d, which is shorter than the period determined from all data sets. The uncertainties were determined by the bootstrap method. The period of 34.675 d reported by Harmanec [1998] was not detected in this data.

The uncertainties of RVs, BVS, and V/R depends on the precision of determination of continuum. The uncertainty is larger when the S/N ratio is lower. The less uncertainty is in determination of V/R ratio, since it is a relative quantity. The uncertainties of RVs depends also on the precision of dispersion relation, on an uncertainty of zero point, on the strength on the measured line, on the number of pixels in detector.

Conclusion

In the first part of my thesis, I analysed a triple star Delta Orionis A using spectroscopic and photometric data from several artificial Earth satellites. I used the special analysis technique of disentangling realised in the program `KOREL` to detect very week spectral lines of the secondary and derived mass ratio and eccentricity. Both values were determined essentially in accord with the predictions Mayer et al. [2010]. Then, I obtained a combined solution of the light- and radial-velocity curves of the eclipsing binary using the programme `PHOEBE 1` Prša and Zwitter [2005].

In the second part, I analysed the Be star Omega Canis Majoris. I measured RVs at the core of the He I 6678 line profiles, their asymmetry quantified by bisector velocity span, and V/R ratio, equivalent width and the strength of the H_α emission line. I also constructed $O - C$ points from RVs and $O - C$ constructed from asymmetry BVS. The conjecture that the changes in period correlate to the extension of the circumstellar envelope seems to be proven.

Bibliography

H. A. Abt and S. G. Levy. Binaries among B2 - B5 IV, V absorption and emission stars. ApJS, 36:241–258, February 1978. doi: 10.1086/190498.

Helmut A. Abt. Normal and abnormal binary frequencies. ARA&A, 21(1):343–372, 1983. doi: 10.1146/annurev.aa.21.090183.002015. URL `https://doi.org/10.1146/annurev.aa.21.090183.002015`.

D. Baade. An unusually short stable period of absorption line asymmetries and V/R variations in the spectrum of the Be star 28 CMa. A&A, 105:65, January 1982a.

D. Baade. Does 28 CMa have a photometric period differing from its spectroscopic period. A&A, 110:L15–L17, June 1982b.

D. Baade. There are more absorption line profile-variable Be stars with short periods. A&A, 134:105–117, May 1984.

D. Baade, Th. Rivinius, A. Pigulski, A. C. Carciofi, Ch. Martayan, A. F. J. Moffat, G. A. Wade, W. W. Weiss, J. Grunhut, G. Handler, R. Kuschnig, A. Mehner, H. Pablo, A. Popowicz, S. Rucinski, and G. Whittaker. Short-term variability and mass loss in Be stars. I. BRITE satellite photometry of η and μ Centauri. A&A, 588:A56, April 2016. doi: 10.1051/0004-6361/201528026.

D. Ballereau and J. Chauville. Long-term and mid-term spectroscopic variations of the Be-shell star HD 184279 (V1294 Aql). II. Towards a model. A&A, 214: 285–294, April 1989.

L. A. Balona, F. Marang, P. Monderen, A. Reitermann, and F. J. Zickgraf. The short-period photometric variability of four Be stars. A&AS, 71:11–24, October 1987.

L. A. Balona, S. Štefl, and C. Aerts. Modeling of Rapid HeI 667.8 Line Profile Variations in the Be Star 28 CMa. In Paul A. Bradley and Joyce A. Guzik, editors, *A Half Century of Stellar Pulsation Interpretation*, volume 135 of *Astronomical Society of the Pacific Conference Series*, page 147, January 1998.

D. P. K. Banerjee, S. D. Rawat, and P. Janardhan. Hα observations of Be stars. A&AS, 147:229–242, December 2000. doi: 10.1051/aas:2000299.

H. Božić, J. Nemravová, and P. Harmanec. Standard UBV photometry and improved physical properties of TW Dra. *Information Bulletin on Variable Stars*, 6086:1, December 2013.

D. Briot. Non-radial pulsations in Be stars. In F. Favata, S. Aigrain, and A. Wilson, editors, *Stellar Structure and Habitable Planet Finding*, volume 538 of *ESA Special Publication*, pages 289–291, January 2004.

A. Claret. Comprehensive tables for the interpretation and modeling of the light curves of eclipsing binaries. A&AS, 131:395–400, September 1998. doi: 10.1051/aas:1998278.

A. Claret. The evolution of the theoretical bolometric albedo in close binary systems. MNRAS, 327(3):989–994, November 2001. doi: 10.1046/j.1365-8711.2001.04783.x.

D. Clarke. Does 28 Canis Majoris exhibit a double oscillation periodicity ? A&A, 232:411, June 1990.

M. F. Corcoran, J. S. Nichols, H. Pablo, T. Shenar, A. M. T. Pollock, W. L. Waldron, A. F. J. Moffat, N. D. Richardson, C. M. P. Russell, K. Hamaguchi, D. P. Huenemoerder, L. Oskinova, W.-R. Hamann, Y. Nazé, R. Ignace, N. R. Evans, J. R. Lomax, J. L. Hoffman, K. Gayley, S. P. Owocki, M. Leutenegger, T. R. Gull, K. T. Hole, J. Lauer, and R. C. Iping. A Coordinated X-Ray and Optical Campaign of the Nearest Massive Eclipsing Binary, δ Orionis Aa. I. Overview of the X-Ray Spectrum. ApJ, 809(2):132, 2015. URL `http://stacks.iop.org/0004-637X/809/i=2/a=132`.

J. Dachs and W. Wamsteker. Infrared photometry of southern Be stars. *Be Star Newsletter*, 4:2, January 1981.

J. Dachs, R. Hanuschik, D. Kaiser, D. Ballereau, P. Bouchet, R. Kiehling, J. Kozok, R. Rudolph, and W. Schlosser. Measurements of Balmer emission line profiles for southern Be stars. II. New data and radial velocities. A&AS, 63:87–141, January 1986.

J. Dachs, W. Hummel, and R. W. Hanuschik. A study of high-resolution emission-line profiles for Be stars. A&AS, 95:437–460, November 1992.

Gaspard Duchêne and Adam Kraus. Stellar Multiplicity. ARA&A, 51(1):269–310, August 2013. doi: 10.1146/annurev-astro-081710-102602.

P. B. Etzel. A Simple Synthesis Method for Solving the Elements of Well-Detached Eclipsing Systems. In Ellen B. Carling and Zdenek Kopal, editors, *Photometric and Spectroscopic Binary Systems*, volume 69 of *NATO Advanced Study Institute (ASI) Series C*, page 111, January 1981.

Mohammad Reza Ghoreyshi. A Multi-technique Study of the Dynamical Evolution of the Viscous Disk around the Be Star ω CMa. *arXiv e-prints*, art. arXiv:1811.02205, November 2018.

B. A. Gould. On the Period of the Variable R Hydrae. *Astronomische Nachrichten*, 102:341, 1882.

P. Hadrava. Eclipsing binaries-light curve solutions. *Contributions of the Astronomical Observatory Skalnate Pleso*, 20:23, January 1990.

P. Hadrava. Orbital elements of multiple spectroscopic stars. *Astronomy and Astrophysics*, 114:393, December 1995.

P. Hadrava. Relative line photometry of eclipsing binaries. *Astronomy and Astrophysics*, 122:581–584, May 1997. doi: 10.1051/aas:1997102.

P. Hadrava. FOTEL 4 - User's guide. *Publications of the Astronomical Institute of the Czechoslovak Academy of Sciences*, 92:1–14, January 2004.

R. W. Hanuschik, J. R. Kozok, and D. Kaiser. High resolution emission-line spectroscopy of Be stars. III. Balmer line profiles. A&A, 189:147–162, January 1988.

R. W. Hanuschik, W. Hummel, E. Sutorius, O. Dietle, and G. Thimm. Atlas of high-resolution emission and shell lines in Be stars. Line profiles and short-term variability. A&AS, 116:309–358, April 1996.

P. Harmanec. Review of observational facts about Be stars. *Hvar Observatory Bulletin*, 7(1):55–88, January 1983a.

P. Harmanec. Review of observational facts about Be stars. *Hvar Observatory Bulletin*, 7(1):55–88, January 1983b.

P. Harmanec. Long-term monitoring of the complex variations of Be stars. In Christiaan Sterken and Mart de Groot, editors, *The Impact of Long-Term Monitoring on Variable Star Research: Astrophysics*, volume 436 of *NATO Advanced Study Institute (ASI) Series C*, page 55, January 1994.

P. Harmanec. On the nature of the Be phenomenon. I. The case of omega Canis Majoris. A&A, 334:558–570, June 1998.

P. Harmanec. Physical Properties and Evolutionary Stage of Be Stars. In Myron A. Smith, Huib F. Henrichs, and Juan Fabregat, editors, *IAU Colloq. 175: The Be Phenomenon in Early-Type Stars*, volume 214 of *Astronomical Society of the Pacific Conference Series*, page 13, January 2000.

P. Harmanec and M. Brož. *Stavba a vývoj hvězd*. MATFYZPRESS, 2011. ISBN 978-80-7378-165-1.

P. Harmanec, P. Mayer, and M. Šlechta. The Massive Binary Delta Ori and the Problem of the Spectroscopic Detection of its Weak Secondary. In *Massive Stars: From alpha to Omega*, page 70, June 2013.

Petr Harmanec. Rapid variability of early-type stars; Proceedings of the Workshop, Hvar, Yugoslavia, September 19-23, 1983. *Hvar Observatory Bulletin*, 7(1), January 1983c.

Petr Harmanec. Stellar Masses and Radii Based on Modern Binary Data. *Bulletin of the Astronomical Institutes of Czechoslovakia*, 39:329, Dec 1988.

J. A. Hartigan. Using subsample values as typical values. *Journal of the American Statistical Association*, 64(328):1303–1317, 1969. ISSN 01621459. URL `http://www.jstor.org/stable/2286069`.

A. S. Harvey, D. J. Stickland, I. D. Howarth, and E. J. Zuiderwijk. Spectroscopic binary orbits from photoelectric radial velocities. Paper 3: delta Orionis. *The Observatory*, 107:205–210, October 1987.

James A. Harvin, Douglas R. Gies, Jr. William G. Bagnuolo, Laura R. Penny, and Michelle L. Thaller. Tomographic Separation of Composite Spectra. VIII. The Physical Properties of the Massive Compact Binary in the Triple Star System HD 36486 (δ Orionis A). *The Astrophysical Journal*, 565(2):1216, 2002. URL `http://stacks.iop.org/0004-637X/565/i=2/a=1216`.

G. Hill and S. Rucinski. *Light2: A Light-Curve Modeling Program*. Springer New York, New York, NY, 1993. ISBN 978-1-4612-2742-7.

C. Hoffmeister, G. Richter, and W. Wenzel. *Variable stars*. Berlin : Springer-Verlag, 1985, 1985. ISBN 0387134034.

J. Horn, P. Koubsky, P. Hadrava, K. Juza, S. Kriz, P. Skoda, and S. Stefl. The orbit of the spectroscopic binary ρ Aurigae. A&AS, 105:119–124, May 1994.

J. Horn, J. Kubat, P. Harmanec, P. Koubsky, P. Hadrava, V. Simon, S. Stefl, and P. Skoda. Spectroscopic orbit of the triple star 55 Ursae Majoris. A&A, 309: 521–529, May 1996.

A. Kaufer, O. Stahl, S. Tubbesing, P. Nørregaard, G. Avila, P. Francois, L. Pasquini, and A. Pizzella. Commissioning FEROS, the new high-resolution spectrograph at La-Silla. *The Messenger*, 95:8–12, March 1999.

A. F. Kholtygin, T. E. Burlakova, S. N. Fabrika, G. G. Valyavin, and M. V. Yushkin. Microvariability of line profiles in the spectra of OB stars: δOri A. *Astronomy Reports*, 50(11):887–901, November 2006. doi: 10.1134/S1063772906110035.

Dr Kieran, Kieran Carroll, Space Projects, Dr Robert, Robert Zee, Jaymie Matthews, and Asst Professor. The MOST Microsatellite Mission: Canada's First Space Telescope. In *AIAA/USU Conference on Small Satellites*, 1998. doi: 10.13140/2.1.4085.5681.

R. H. Koch and B. J. Hrivnak. A photometric study of the close binary Delta Orionis A. *The Astrophysical Journal*, 248:249–255, August 1981. doi: 10.1086/159148.

P. Koubský, P. Harmanec, M. Brož, L. Kotková, S. Yang, H. Božić, D. Sudar, Y. Frémat, D. Korčáková, V. Votruba, P. Škoda, M. Šlechta, and D. Ruždjak. Properties and nature of Be stars. 31. The binary nature, light variability, physical elements, and emission-line changes of HD 81357. A&A, 629:A105, September 2019. doi: 10.1051/0004-6361/201834597.

S. Kriz and P. Harmanec. A Hypothesis of the Binary Origin of Be Stars. *Bulletin of the Astronomical Institutes of Czechoslovakia*, 26:65, January 1975.

Glenn Ledrew. The Real Starry Sky. JRASC, 95:32, February 2001.

F. Lombard. An alternative to O — C analysis of variable star periods. *Monthly Notices of the Royal Astronomical Society*, 294(4):657–666, 03 1998. ISSN 0035-8711. doi: 10.1111/j.1365-8711.1998.01214.x. URL `https://doi.org/10.1111/j.1365-8711.1998.01214.x`.

F. Martins, D. Schaerer, and D. J. Hillier. A new calibration of stellar parameters of Galactic O stars. A&A, 436(3):1049–1065, Jun 2005.

P. F. L. Maxted. ellc: A fast, flexible light curve model for detached eclipsing binary stars and transiting exoplanets. A&A, 591:A111, June 2016. doi: 10.1051/0004-6361/201628579.

P. Mayer, P. Harmanec, M. Wolf, H. Božić, and M. Šlechta. Physical elements of the eclipsing binary δ Orionis. A&A, 520:A89, September 2010. doi: 10.1051/0004-6361/200913796.

R. E. Mennickent, N. Vogt, and C. Sterken. Long-term photometry of Be stars. I. Fading events and variations on time scales of years. A&AS, 108:237–250, November 1994.

G. Meynet, P. Eggenberger, S. Ekström, C. Georgy, J. Groh, A. Maeder, H. Saio, and T. Moriya. Four open questions in massive star evolution. *EAS Publications Series*, 63:373–383, 2013. ISSN 1638-1963. doi: 10.1051/eas/1363042. URL `http://dx.doi.org/10.1051/eas/1363042`.

Maxwell Moe and Rosanne Di Stefano. Mind Your Ps and Qs: The Interrelation between Period (P) and Mass-ratio (Q) Distributions of Binary Stars. ApJS, 230(2):15, Jun 2017. doi: 10.3847/1538-4365/aa6fb6.

Yaël Nazé, Gregor Rauw, and Constantin Cazorla. π Aquarii is another γ Cassiopeiae object. A&A, 602:L5, June 2017. doi: 10.1051/0004-6361/201731135.

Burt Nelson and Walter D. Davis. Eclipsing-Binary Solutions by Sequential Optimization of the Parameters. ApJ, 174:617, June 1972. doi: 10.1086/151524.

J. A. Nemravová, P. Harmanec, M. Brož, D. Vokrouhlický, D. Mourard, C. A. Hummel, C. Cameron, J. M. Matthews, C. T. Bolton, H. Božić, R. Chini, T. Dembsky, S. Engle, C. Farrington, J. H. Grunhut, D. B. Guenther, E. F. Guinan, D. Korčáková, P. Koubský, R. Kříček, R. Kuschnig, P. Mayer, G. P. McCook, A. F. J. Moffat, N. Nardetto, A. Prša, J. Ribeiro, J. Rowe, S. Rucinski, P. Škoda, M. Šlechta, I. Tallon-Bosc, V. Votruba, W. W. Weiss, M. Wolf, P. Zasche, and R. T. Zavala. ξTauri: a unique laboratory to study the dynamic interaction in a compact hierarchical quadruple system. A&A, 594:A55, October 2016. doi: 10.1051/0004-6361/201628860.

J. Nichols, D. P. Huenemoerder, M. F. Corcoran, W. Waldron, Y. Nazé, A. M. T. Pollock, A. F. J. Moffat, J. Lauer, T. Shenar, C. M. P. Russell, N. D. Richardson, H. Pablo, N. R. Evans, K. Hamaguchi, T. Gull, W.-R. Hamann, L. Oskinova, R. Ignace, Jennifer L. Hoffman, K. T. Hole, and J. R. Lomax. A Coordinated X-Ray and Optical Campaign of the Nearest Massive Eclipsing Binary, δ Orionis Aa. II. X-Ray Variability. *The Astrophysical Journal*, 809(2):133, 2015. URL `http://stacks.iop.org/0004-637X/809/i=2/a=133`.

A. Oplištilová. Analýza a řešení světelných křivek hmotné trojhvězdy δ orionis. Bachelor Thesis, 6 2019.

A. Oplištilová, P. Harmanec, P. Mayer, P. Zasche, M. Šlechta, H. Pablo, A. Pigulski, and BRITE TEAM, editors. *Improved model of Delta Orionis*, volume 50, 03 2020. doi: 10.31577/caosp.2020.50.2.585.

H. Pablo, G. N. Whittaker, A. Popowicz, S. M. Mochnacki, R. Kuschnig, C. C. Grant, A. F. J. Moffat, S. M. Rucinski, J. M. Matthews, A. Schwarzenberg-Czerny, G. Handler, W. W. Weiss, D. Baade, G. A. Wade, E. Zocłońska,

T. Ramiaramanantsoa, M. Unterberger, K. Zwintz, A. Pigulski, J. Rowe, O. Koudelka, P. Orleański, A. Pamyatnykh, C. Neiner, R. Wawrzaszek, G. Marciniszyn, P. Romano, G. Woźniak, T. Zawistowski, and R. E. Zee. The BRITE Constellation Nanosatellite Mission: Testing, Commissioning, and Operations. *Publications of the Astronomical Society of the Pacific*, 128(970):125001, 2016. URL `http://stacks.iop.org/1538-3873/128/i=970/a=125001`.

Herbert Pablo, Noel D. Richardson, Anthony F. J. Moffat, Michael Corcoran, Tomer Shenar, Omar Benvenuto, Jim Fuller, Yaël Nazé, Jennifer L. Hoffman, Anatoly Miroshnichenko, Jesús Maíz Apellániz, Nancy Evans, Thomas Eversberg, Ken Gayley, Ted Gull, Kenji Hamaguchi, Wolf-Rainer Hamann, Huib Henrichs, Tabetha Hole, Richard Ignace, Rosina Iping, Jennifer Lauer, Maurice Leutenegger, Jamie Lomax, Joy Nichols, Lida Oskinova, Stan Owocki, Andy Pollock, Christopher M. P. Russell, Wayne Waldron, Christian Buil, Thierry Garrel, Keith Graham, Bernard Heathcote, Thierry Lemoult, Dong Li, Benjamin Mauclaire, Mike Potter, Jose Ribeiro, Jaymie Matthews, Chris Cameron, David Guenther, Rainer Kuschnig, Jason Rowe, Slavek Rucinski, Dimitar Sasselov, and Werner Weiss. A Coordinated X-Ray and Optical Campaign of the Nearest Massive Eclipsing Binary, δ Orionis Aa. III. Analysis of Optical Photometric (MOST) and Spectroscopic (Ground-based) Variations. *The Astrophysical Journal*, 809(2):134, 2015. URL `http://stacks.iop.org/0004-637X/809/i=2/a=134`.

J. R. Percy, J. A. Mattei, and C. Sterken. *Variable star research: an international perspective. Proceedings.* 1992.

E. Pollmann. The Correlation between H-alpha and HeI 6678 Emission Activity in the Be Star gamma Cassiopeiae from 1995 to 2021. *The Journal of American Association of Variable Star Observer*, 49(1):77, June 2021.

A. Prša and T. Zwitter. A Computational Guide to Physics of Eclipsing Binaries. I. Demonstrations and Perspectives. *The Astrophysical Journal*, 628(1):426, 2005. URL `http://stacks.iop.org/0004-637X/628/i=1/a=426`.

A. Prša, Kyle Conroy, Martin Horvat, Herbert Pablo, Angela Kochoska, S. Bloemen, Jana Nemravova, Joseph Giammarco, K. Hambleton, and P. Degroote. Physics of eclipsing binaries. ii. the increased model precision. 09 2016.

A. Quirrenbach, K. S. Bjorkman, J. E. Bjorkman, C. A. Hummel, D. F. Buscher, J. T. Armstrong, D. Mozurkewich, N. M. Elias II, and B. L. Babler. Constraints on the geometry of circumstellar envelopes: Optical interferometric and spectropolarimetric observations of seven be stars. ApJ, 479(1):477–496, apr 1997. doi: 10.1086/303854. URL `https://doi.org/10.1086%2F303854`.

Deepak Raghavan, Harold A. McAlister, Todd J. Henry, David W. Latham, Geoffrey W. Marcy, Brian D. Mason, Douglas R. Gies, Russel J. White, and Theo A. ten Brummelaar. A Survey of Stellar Families: Multiplicity of Solar-type Stars. ApJS, 190(1):1–42, Sep 2010. doi: 10.1088/0067-0049/190/1/1.

Noel D. Richardson, Anthony F. J. Moffat, Theodore R. Gull, Don J. Lindler, Douglas R. Gies, Michael F. Corcoran, and André-Nicolas Chené. HST/STIS Ultraviolet Spectroscopy of the Components of the Massive Triple Star δ Ori A. ApJ, 808(1):88, 2015. URL `http://stacks.iop.org/0004-637X/808/i=1/a=88`.

T. Rivinius, D. Baade, S. Stefl, O. Stahl, B. Wolf, and A. Kaufer. Stellar and circumstellar activity of the Be star MU Centauri. II. Multiperiodic low-order line-profile variability. *Astronomy Astrophysics*, 336:177–190, August 1998.

Thomas Rivinius, Alex C. Carciofi, and Christophe Martayan. Classical Be stars. Rapidly rotating B stars with viscous Keplerian decretion disks. A&A Rev., 21: 69, October 2013. doi: 10.1007/s00159-013-0069-0.

S. M. Ruciński. The W UMa-type Systems as Contact Binaries. I. Two Methods of Geometrical Elements Determination. Degree of Contact. Acta Astron., 23: 79, January 1973.

T. Shenar, L. Oskinova, W. R. Hamann, M. F. Corcoran, A. F. J. Moffat, H. Pablo, N. D. Richardson, W. L. Waldron, D. P. Huenemoerder, J. Maíz Apellániz, J. S. Nichols, H. Todt, Y. Nazé, J. L. Hoffman, A. M. T. Pollock, and I. Negueruela. A Coordinated X-Ray and Optical Campaign of the Nearest Massive Eclipsing Binary, δ Orionis Aa. IV. A Multiwavelength, Non-LTE Spectroscopic Analysis. ApJ, 809(2):135, August 2015. doi: 10.1088/0004-637X/809/2/135.

Arne Slettebak, II Collins, George W., and Ryland Truax. Physical Properties of Be Star Envelopes from Balmer and Fe II Emission Lines. ApJS, 81:335, July 1992. doi: 10.1086/191696.

John Southworth. JKTEBOP: Analyzing light curves of detached eclipsing binaries, July 2012.

Christopher Stagg. A photometric survey of the bright southern Be stars. MNRAS, 227:213–240, July 1987. doi: 10.1093/mnras/227.1.213.

R. F. Stellingwerf. Period determination using phase dispersion minimization. ApJ, 224:953–960, September 1978. doi: 10.1086/156444.

Otto Struve. "The Royal Road to Success": Henry Norris Russell (1877-1957). PASP, 69(408):223, June 1957. doi: 10.1086/127052.

Ken'ichi Tanaka, Kozo Sadakane, Shin-Ya Narusawa, Hiroyuki Naito, Eiji Kambe, Jun-Ichi Katahira, and Ryuko Hirata. Dramatic Spectral and Photometric Changes of Pleione (28 Tau) between 2005 November and 2007 April. PASJ, 59:L35, August 2007. doi: 10.1093/pasj/59.4.L35.

C. G. Toner and David F. Gray. The Star Patch on the G8 Dwarf chi Bootis A. ApJ, 334:1008, November 1988. doi: 10.1086/166893.

A. van Hoof. Observations of 26, 27 and 28 CMa. *Information Bulletin on Variable Stars*, 992:1, April 1975.

H C. Vogel and J. Scheiner. Observations. *Publikationen des Astrophysikalischen Observatoriums zu Potsdam*, 100, 1892.

S. Štefl and T. Rivinius. HEROS Be Star Campaigns. In Myron A. Smith, Huib F. Henrichs, and Juan Fabregat, editors, *IAU Colloq. 175: The Be Phenomenon in Early-Type Stars*, volume 214 of *Astronomical Society of the Pacific Conference Series*, page 356, January 2000.

S. Štefl, D. Baade, T. Rivinius, O. Stahl, B. Wolf, and A. Kaufer. Circumstellar Quasi-periods Accompanying Stellar Periods of Be Stars. In Paul A. Bradley and Joyce A. Guzik, editors, *A Half Century of Stellar Pulsation Interpretation*, volume 135 of *Astronomical Society of the Pacific Conference Series*, page 348, January 1998.

S. Štefl, C. Aerts, and L. A. Balona. Simultaneous photometry and spectroscopy of the Be star 28 (omega) CMa - I. Observational evidence of the periodic components of rapid variability. MNRAS, 305(3):505–518, May 1999. doi: 10.1046/j.1365-8711.1999.02324.x.

S. Štefl, D. Baade, T. Rivinius, S. Otero, O. Stahl, A. Budovičová, A. Kaufer, and M. Maintz. Stellar and circumstellar activity of the Be star omega CMa. I. Line and continuum emission in 1996-2002. A&A, 402:253–265, April 2003a. doi: 10.1051/0004-6361:20030224.

S. Štefl, D. Baade, Th. Rivinius, O. Stahl, A. Budovičová, A. Kaufer, and M. Maintz. Stellar and circumstellar activity of the Be star omega CMa. II. Periodic line-profile variability. A&A, 411:167–180, November 2003b. doi: 10.1051/0004-6361:20031179.

S. Štefl, W. Nowotny-Schipper, and J. Reunanen. The circumstellar disk of the Be star 28 (ω) CMa. In G. Perrin and F. Malbet, editors, *EAS Publications Series*, volume 6 of *EAS Publications Series*, page 257, January 2003c. doi: 10.1051/eas:2003024.

Rainer Wichmann. Nightfall User Manual. `https://manualzz.com/doc/4158633/nightfall-user-manual`, 1998. cited: 2021-07-04.

D. B. Wood. An analytic model of eclipsing binary star systems. AJ, 76:701–710, October 1971. doi: 10.1086/111187.

S. Štefl, L. A. Balona, and C. Aerts. Simultaneous photometry and spectroscopy of the Be star 28 (omega) CMa III. Original data. *Journal of Astronomical Data*, 6(3):3, January 2000.

List of Figures

List of Tables

List of Abbreviations

BVS Bisector velocity span

CCF Cross-correlation function

ESO European Southern Observatory located on the outskirts of the Chilean Atacama Desert, 600 km north of Santiago de Chile and at an altitude of 2400 metres

HRD The Hertzsprung–Russell diagram (a scatter plot of stars showing the relationship between the stars' absolute magnitudes or luminosities versus their stellar classifications or effective temperatures)

PDM The phase dispersion minimization method

PoWR Potsdam Wolf–Rayet code (non-LTE for hot stars)

RV, RVs Radial velocity, radial velocities

loc. con. Units of local continuum

A. Attachments

A.1 Controlling file for KOREL

Script 1: korel.par – input file with settings for running KOREL.

```
2 0 2 0 0 1 0 0 0 1 0 | key(1,...,5)
o 0 1 0 1 1  5.73282 0.46744E-05
o 0 2 2 1 1   54002.74   0.5
o 0 3 1 1 1   0.073    0.010
o 0 4 1 1 1     143.    1.5
o 0 5 1 1 1     107.0  -1.0
o 0 6 0 1 1     0.41    -0.02
o 0 7 0 1 1  0.00422 0.000057
o 2 1 0 1 1  99000.    1650.0
o 2 2 1 1 1  39800.    300.
o 2 3 0 1 1  0.77      0.01
o 2 4 0 1 1  70.      -6.0
o 2 5 1 1 1  3.5      -1.0
o 2 6 0 1 1  0.50      0.09
x 0 0 0 0 0 0 0 0 0 | end of elements
1 2 1 0 0 0 0 0 0 1 0 | key(1,...,5)
o 0 1 0 0 1  5.73282   0.46744E-05
o 0 2 2 0 1  54002.74  0.5
o 0 3 0 0 1  0.073     0.010
o 0 4 0 0 1  143.      1.5
o 0 5 0 0 1  107.0    -1.0
o 0 6 1 0 1  0.41     -0.02
o 0 7 0 0 1  0.00422   0.000057
o 2 1 0 0 1  99000.    1650.0
o 2 2 0 0 1  39800.    300.
o 2 3 0 0 1  0.77      0.01
o 2 4 0 0 1  70.      -6.0
o 2 5 0 0 1  3.5      -1.0
o 2 6 0 0 1  0.50      0.09
x 0 0 0 0 0 0 0 0 0 | end of elements
1 1 1 0 0 0 0 2 1 0 | key(1,...,5)
o 0 1 0 0 1  5.73282   0.46744E-05
o 0 2 2 0 1  54002.74  0.5
o 0 3 1 0 1  0.073     0.010
o 0 4 1 0 1  143.      1.5
o 0 5 1 0 1  107.0    -1.0
o 0 6 1 0 1  0.41     -0.02
o 0 7 0 0 1  0.00422   0.000057
o 2 1 0 0 1  99000.    1650.0
o 2 2 1 0 1  39800.    300.
o 2 3 0 0 1  0.77      0.01
o 2 4 0 0 1  70.      -6.0
o 2 5 1 0 1  3.5      -1.0
o 2 6 0 0 1  0.50      0.09
x 0 0 0 0 0 0 0 0 0 | end of elements
```

A.2 The bootstrap method

Script 2: Running the program `hec27` with randomly generated inputs in `bash`.

```
#!/bin/bash
# A cycle over 50 000 samples
for j in {1..50000}; do
# Creating a file of 858 coupled pairs of time and normalized RV
# randomly chosen from 858 measurement with repetition
awk -v x=$RANDOM '{row[NR]=$0}
END {srand(x)
    for (i=1;i<=858;i++)
        print row[int(1+rand()*NR)]} ' RV_Stel0 > RV_Stel_boot
# Adding a text row at the beginning of file as hec27 required
sed -i '1s/^/Random RV_Stel\n/' RV_Stel_boot
# Running hec27 and providing control file, data file with coupled
# pairs of time and normalized RV, and the name of output file
printf "key\nRV_Stel_boot\nRV_output\n" | ./hec27
# Moving output file to another directory
mv /DATADISK/bootstrap/RV_output /DATADISK/bootstrap/results/out"$j"
done
# Navigating to the directory with all output files
cd "/DATADISK/bootstrap/results/"
# Printing all 50 000 resulting periods to a file (data for histogram)
for file in out*; do
sed -e '1,27d' "$file" | awk 'NR==1{print $1}' >> periods_all.dat
done
```

A.3 All measured quantities and information about data for ω CMa

The table below shows measured quantities and information about data. If the quantity is missing, - is used instead of the value.

Instr.	T [RJD]	RV_n [km/s]	σ_{RV_n} [km/s]	V [loc. con.]	R [loc. con.]	V/R	$\frac{1}{2}(V+R)$ [loc. con.]	BVS [km/s]	Group, T_{loc} [RJD]	Number of RV	OC_{RV} [RJD]	$\sigma_{OC_{RV}}$ [RJD]	OC_{BVS} [RJD]	$\sigma_{OC_{BVS}}$ [RJD]
1.52-m	40607.5399	-0.2703	0.0844	-	-	-	-	-		6	0.3330	0.0570	-	-
1.52-m	40607.7343	0.1081	0.0844	-	-	-	-	-	1					
1.52-m	40607.8725	-0.0811	0.0844	-	-	-	-	-						
1.52-m	40608.5558	-0.5405	0.0844	-	-	-	-	-						
1.52-m	40608.7211	-0.5946	0.0844	-	-	-	-	-						
1.52-m	40608.7523	-0.5135	0.0844	-	-	-	-	-	40607.8590					
1.0-m	42033.0080	0.4015	0.2275	-	-	-	-	-		8	-0.0855	0.0420	-	-
1.0-m	42033.9860	-0.6317	0.2275	-	-	-	-	-	2					
1.0-m	42075.7910	0.6266	0.2275	-	-	-	-	-						
1.0-m	42103.7890	-0.3760	0.2275	-	-	-	-	-						
1.0-m	42129.7420	0.1355	0.2275	-	-	-	-	-						
1.0-m	42150.7010	-0.4118	0.2275	-	-	-	-	-						
1.0-m	42425.7870	0.5448	0.2275	-	-	-	-	-						
1.0-m	42452.7610	-0.1918	0.2275	-	-	-	-	-	42075.8560					
1.0-m	42724.9110	1.0000	0.2275	-	-	-	-	-		3	-0.0345	0.0540	-	-
1.0-m	42725.9940	0.2379	0.2275	-	-	-	-	-	3					
1.0-m	42777.8540	-0.5294	0.2275	-	-	-	-	-	42724.9070					
1.0-m	42836.7440	-0.7289	0.2275	-	-	-	-	-		6	-0.2405	0.0820	-	-
1.0-m	42837.6610	0.2737	0.2275	-	-	-	-	-	4					
1.0-m	42858.6670	0.3606	0.2275	-	-	-	-	-						
1.0-m	42859.6700	0.6317	0.2275	-	-	-	-	-						
1.0-m	42886.6260	0.7698	0.2275	-	-	-	-	-						
1.0-m	42887.6180	-1.0000	0.2275	-	-	-	-	-	42886.6080					
1.52-m	43091.8174	-0.7568	0.0844	-	-	-	-	-		12	0.0416	0.0130	-	-
1.52-m	43091.8414	-0.8108	0.0844	-	-	-	-	-	5					
1.52-m	43092.8355	1.0000	0.0844	-	-	-	-	-						
1.52-m	43093.7825	0.1622	0.0844	-	-	-	-	-						
1.52-m	43094.8506	-1.0000	0.0844	-	-	-	-	-						
1.52-m	43095.7976	-0.3514	0.0844	-	-	-	-	-						
1.52-m	43095.8256	-0.2973	0.0844	-	-	-	-	-						
1.52-m	43095.8546	-0.4054	0.0844	-	-	-	-	-						
1.52-m	43095.8626	-0.4054	0.0844	-	-	-	-	-						
1.52-m	43095.8776	-0.3243	0.0844	-	-	-	-	-						
1.52-m	43096.8017	0.7838	0.0844	-	-	-	-	-						

Instr.	T [RJD]	RV_n [km/s]	σ_{RV_n} [km/s]	V [loc. con.]	R [loc. con.]	V/R	$\frac{1}{2}(V+R)$ [loc. con.]	BVS [km/s]	Group, T_{loc} [RJD]	Number of RV	OC_{RV} [RJD]	$\sigma_{OC_{RV}}$ [RJD]	OC_{BVS} [RJD]	$\sigma_{OC_{BVS}}$ [RJD]
1.52-m	43096.8737	0.5405	0.0844	-	-	-	-	-	43092.7040					
1.23-m	43499.5584	-0.5319	0.2797	-	-	-	-	-		8	-0.1042	0.043	-	-
1.23-m	43500.5494	-0.3617	0.2797	-	-	-	-	-	6					
1.23-m	43500.6284	-0.4043	0.2797	-	-	-	-	-						
1.23-m	43501.5115	0.2340	0.2797	-	-	-	-	-						
1.23-m	43501.6395	0.4468	0.2797	-	-	-	-	-						
1.23-m	43502.5255	0.0638	0.2797	-	-	-	-	-						
1.23-m	43502.6215	0.7872	0.2797	-	-	-	-	-						
1.23-m	43503.4845	-1.0000	0.2797	-	-	-	-	-	43502.8140					
1.23-m	43504.4955	0.4468	0.2797	-	-	-	-	-		6	-0.0474	0.039	-	-
1.23-m	43505.5125	0.5745	0.2797	-	-	-	-	-	7					
1.23-m	43505.6196	0.5745	0.2797	-	-	-	-	-						
1.23-m	43508.5166	0.7447	0.2797	-	-	-	-	-						
1.23-m	43509.5896	1.0000	0.2797	-	-	-	-	-						
1.23-m	43510.5886	-0.6596	0.2797	-	-	-	-	-	43505.6150					
1.52-m	43884.5347	0.0270	0.0844	-	-	-	-	-		26	-0.0771	0.0092	-	-
1.52-m	43884.8587	-0.8649	0.0844	-	-	-	-	-	8					
1.52-m	43885.5637	0.5946	0.0844	-	-	-	-	-						
1.52-m	43885.8618	0.3514	0.0844	-	-	-	-	-						
1.52-m	43886.5198	-0.6757	0.0844	-	-	-	-	-						
1.52-m	43886.5618	-0.5946	0.0844	-	-	-	-	-						
1.52-m	43886.6028	-0.5135	0.0844	-	-	-	-	-						
1.52-m	43886.8048	0.2432	0.0844	-	-	-	-	-						
1.52-m	43886.8678	0.4324	0.0844	-	-	-	-	-						
1.52-m	43887.5278	-0.8108	0.0844	-	-	-	-	-						
1.52-m	43887.5858	-0.9459	0.0844	-	-	-	-	-						
1.52-m	43887.6118	-0.9730	0.0844	-	-	-	-	-						
1.52-m	43887.7868	-0.9189	0.0844	-	-	-	-	-						
1.52-m	43887.8288	-0.8108	0.0844	-	-	-	-	-						
1.52-m	43887.8818	-0.6486	0.0844	-	-	-	-	-						
1.52-m	43888.5188	0.5676	0.0844	-	-	-	-	-						
1.52-m	43888.5758	0.3784	0.0844	-	-	-	-	-						
1.52-m	43888.6168	0.4054	0.0844	-	-	-	-	-						
1.52-m	43888.7948	-0.2432	0.0844	-	-	-	-	-						

Instr.	T [RJD]	RV_n [km/s]	σ_{RV_n} [km/s]	V [loc. con.]	R [loc. con.]	V/R	$\frac{1}{2}(V+R)$ [loc. con.]	BVS [km/s]	Group, T_{loc} [RJD]	Number of RV	OC_{RV} [RJD]	$\sigma_{OC_{RV}}$ [RJD]	OC_{BVS} [RJD]	$\sigma_{OC_{BVS}}$ [RJD]
1.52-m	43888.8298	-0.3784	0.0844	-	-	-	-	-						
1.52-m	43888.8828	-0.5946	0.0844	-	-	-	-	-						
1.52-m	43889.5218	0.2162	0.0844	-	-	-	-	-						
1.52-m	43889.5888	0.3243	0.0844	-	-	-	-	-						
1.52-m	43889.7828	0.6757	0.0844	-	-	-	-	-						
1.52-m	43889.8348	0.5946	0.0844	-	-	-	-	-						
1.52-m	43889.8848	0.7027	0.0844	-	-	-	-	-	43885.6551					
1.52-m	43890.5388	-1.0000	0.0844	-	-	-	-	-		18	-0.1083	0.0078	-	-
1.52-m	43890.5668	-0.7838	0.0844	-	-	-	-	-	9					
1.52-m	43890.6168	-0.7027	0.0844	-	-	-	-	-						
1.52-m	43890.7938	0.0000	0.0844	-	-	-	-	-						
1.52-m	43890.8308	0.1081	0.0844	-	-	-	-	-						
1.52-m	43890.8858	0.1892	0.0844	-	-	-	-	-						
1.52-m	43892.5748	0.6757	0.0844	-	-	-	-	-						
1.52-m	43892.5958	0.7838	0.0844	-	-	-	-	-						
1.52-m	43892.6208	0.5676	0.0844	-	-	-	-	-						
1.52-m	43892.8088	0.0000	0.0844	-	-	-	-	-						
1.52-m	43892.8298	-0.0541	0.0844	-	-	-	-	-						
1.52-m	43892.8688	-0.1892	0.0844	-	-	-	-	-						
1.52-m	43894.5257	-0.9730	0.0844	-	-	-	-	-						
1.52-m	43894.6187	-0.8378	0.0844	-	-	-	-	-						
1.52-m	43894.8027	-0.3243	0.0844	-	-	-	-	-						
1.52-m	43894.8377	-0.2162	0.0844	-	-	-	-	-						
1.52-m	43895.6017	-0.2432	0.0844	-	-	-	-	-						
1.52-m	43895.7987	-0.8378	0.0844	-	-	-	-	-	43892.4844					
1.52-m	44951.6621	0.0946	0.0844	-	-	-	-	-		17	-0.3418	0.0270	-	-
1.52-m	44951.7441	-0.1135	0.0844	-	-	-	-	-	10					
1.52-m	44951.8021	-0.1162	0.0844	-	-	-	-	-						
1.52-m	44951.8661	-0.0297	0.0844	-	-	-	-	-						
1.52-m	44952.6671	-0.0270	0.0844	-	-	-	-	-						
1.52-m	44952.7421	0.0568	0.0844	-	-	-	-	-						
1.52-m	44953.6972	-0.5811	0.0844	-	-	-	-	-						
1.52-m	44953.8392	-0.3000	0.0844	-	-	-	-	-						
1.52-m	44953.8692	-0.2270	0.0844	-	-	-	-	-						

Instr.	T [RJD]	RV_n [km/s]	σ_{RV_n} [km/s]	V [loc. con.]	R [loc. con.]	V/R	$\frac{1}{2}(V+R)$ [loc. con.]	BVS [km/s]	Group, T_{loc} [RJD]	Number of RV	OC_{RV} [RJD]	$\sigma_{OC_{RV}}$ [RJD]	OC_{BVS} [RJD]	$\sigma_{OC_{BVS}}$ [RJD]
1.52-m	44954.6532	-0.3189	0.0844	-	-	-	-	-						
1.52-m	44954.6612	-0.3676	0.0844	-	-	-	-	-						
1.52-m	44954.7762	-0.3757	0.0844	-	-	-	-	-						
1.52-m	44954.8512	-0.4730	0.0844	-	-	-	-	-						
1.52-m	44955.6822	0.2622	0.0844	-	-	-	-	-						
1.52-m	44955.7483	0.2568	0.0844	-	-	-	-	-						
1.52-m	44955.8393	0.2108	0.0844	-	-	-	-	-						
1.52-m	44955.8663	0.0703	0.0844	-	-	-	-	-	44956.9950					
1.4-m	45244.8850	-0.5185	0.0448	-	-	-	-	-		5	-0.15344	0.0720	-	-
1.4-m	45245.8060	0.0795	0.0448	-	-	-	-	-	11					
1.4-m	45246.8600	0.9843	0.0448	-	-	-	-	-						
1.4-m	45351.7850	0.1691	0.0448	-	-	-	-	-						
1.4-m	45351.8200	0.1691	0.0448	-	-	-	-	-	45246.6950					
1.4-m	45352.7040	-0.8589	0.0448	-	-	-	-	-		15	-0.4628	0.0160	-	-
1.4-m	45353.5870	0.2094	0.0448	-	-	-	-	-	12					
1.4-m	45353.7330	-0.0190	0.0448	-	-	-	-	-						
1.4-m	45353.7970	-0.3124	0.0448	-	-	-	-	-						
1.4-m	45354.5540	0.2654	0.0448	-	-	-	-	-						
1.4-m	45354.7120	0.5655	0.0448	-	-	-	-	-						
1.4-m	45354.8130	1.0000	0.0448	-	-	-	-	-						
1.4-m	45355.5820	-0.9239	0.0448	-	-	-	-	-						
1.4-m	45355.7410	-0.3303	0.0448	-	-	-	-	-						
1.4-m	45355.8380	0.0482	0.0448	-	-	-	-	-						
1.4-m	45356.5590	-0.3483	0.0448	-	-	-	-	-						
1.4-m	45356.7030	-0.8275	0.0448	-	-	-	-	-						
1.4-m	45356.8240	-1.0000	0.0448	-	-	-	-	-						
1.4-m	45357.5400	0.4401	0.0448	-	-	-	-	-						
1.4-m	45357.7290	0.5588	0.0448	-	-	-	-	-	45354.7810					
CES	49667.8048	0.9899	0.0009	-	-	-	-	-29.3424		11	0.0156	0.0066	0.6652	0.0150
CES	49667.8782	0.8883	0.0002	-	-	-	-	-23.2479	13					
CES	49668.7284	-0.0176	0.0066	-	-	-	-	-1.8002						
CES	49668.8227	0.2471	0.0023	-	-	-	-	-12.2529						
CES	49668.8854	0.4340	0.0010	-	-	-	-	-20.3654						
CES	49670.7279	0.4649	0.0014	-	-	-	-	-13.5835						

Instr.	T [RJD]	$\mathrm{RV_n}$ [km/s]	$\sigma_{\mathrm{RV_n}}$ [km/s]	V [loc. con.]	R [loc. con.]	V/R	$\frac{1}{2}(V+R)$ [loc. con.]	BVS [km/s]	Group, T_{loc} [RJD]	Number of RV	OC_{RV} [RJD]	$\sigma_{OC_{\mathrm{RV}}}$ [RJD]	OC_{BVS} [RJD]	$\sigma_{OC_{\mathrm{BVS}}}$ [RJD]
CES	49670.8197	0.2105	0.0164	-	-	-	-	-6.7886						
CES	49670.8945	-0.2199	0.0005	-	-	-	-	20.6380						
CES	49671.7283	0.8639	0.0002	-	-	-	-	-42.2023						
CES	49671.7994	0.9436	0.0150	-	-	-	-	-43.7415						
CES	49671.8811	1.0000	0.0016	-	-	-	-	-44.8454	49667.7477					
CES	50093.5444	-0.2714	0.0173	-	-	-	-	13.0300		264	0.0334	0.0023	0.7359	0.0023
CES	50093.5506	-0.2819	0.0017	-	-	-	-	12.9855	14					
CES	50093.5592	-0.3123	0.0124	-	-	-	-	15.5226						
CES	50093.5662	-0.3027	0.0066	-	-	-	-	15.0514						
CES	50093.5738	-0.3746	0.0070	-	-	-	-	17.6484						
CES	50093.5822	-0.4161	0.0203	-	-	-	-	20.0907						
CES	50093.6004	-0.4863	0.0058	-	-	-	-	23.2883						
CES	50093.6210	-0.6268	0.0343	-	-	-	-	28.9538						
CES	50093.6363	-0.6586	0.0240	-	-	-	-	29.9741						
CES	50093.6452	-0.7857	0.0173	-	-	-	-	34.1597						
CES	50093.6528	-0.7617	0.0038	-	-	-	-	34.3136						
CES	50093.6606	-0.7757	0.0001	-	-	-	-	36.0423						
CES	50093.6683	-0.7701	0.0068	-	-	-	-	37.6011						
CES	50093.6771	-0.7556	0.0070	-	-	-	-	37.7927						
CES	50093.6874	-0.8343	0.0220	-	-	-	-	41.4499						
CES	50093.6973	-0.8142	0.0110	-	-	-	-	40.7041						
CES	50093.7184	-0.8152	0.0026	-	-	-	-	41.2645						
CES	50093.7276	-0.8359	0.0101	-	-	-	-	40.5358						
CES	50093.7366	-0.8376	0.0044	-	-	-	-	41.0955						
CES	50093.7462	-0.8325	0.0052	-	-	-	-	42.4232						
CES	50093.7554	-0.8273	0.0003	-	-	-	-	43.7101						
CES	50093.7645	-0.8385	0.0009	-	-	-	-	43.7389						
CES	50093.7819	-0.8472	0.0001	-	-	-	-	43.2143						
CES	50093.7905	-0.8465	0.0112	-	-	-	-	43.3209						
CES	50093.7994	-0.8665	0.0012	-	-	-	-	44.4839						
CES	50093.8080	-0.8495	0.0112	-	-	-	-	43.4189						
CES	50094.5288	0.8996	0.0019	-	-	-	-	-41.1759						
CES	50094.5378	0.8924	0.0010	-	-	-	-	-40.0622						

Instr.	T [RJD]	$\mathrm{RV_n}$ [km/s]	$\sigma_{\mathrm{RV_n}}$ [km/s]	V [loc. con.]	R [loc. con.]	V/R	$\frac{1}{2}(V+R)$ [loc. con.]	BVS [km/s]	Group, T_{loc} [RJD]	Number of RV	OC_{RV} [RJD]	$\sigma_{OC_{\mathrm{RV}}}$ [RJD]	OC_{BVS} [RJD]	$\sigma_{OC_{\mathrm{BVS}}}$ [RJD]
CES	50094.5451	0.8789	0.0003	-	-	-	-	-38.3924						
CES	50094.5512	0.8738	0.0042	-	-	-	-	-39.5059						
CES	50094.5578	0.8551	0.0003	-	-	-	-	-36.1949						
CES	50094.5651	0.8231	0.0003	-	-	-	-	-37.8888						
CES	50094.5721	0.8380	0.0001	-	-	-	-	-39.3093						
CES	50094.5795	0.8094	0.0010	-	-	-	-	-36.8251						
CES	50094.5883	0.7437	0.0009	-	-	-	-	-35.5784						
CES	50094.5975	0.7330	0.0145	-	-	-	-	-34.5120						
CES	50094.6067	0.7344	0.0276	-	-	-	-	-30.6830						
CES	50094.6237	0.6654	0.0010	-	-	-	-	-30.8031						
CES	50094.6313	0.6353	0.0023	-	-	-	-	-30.4927						
CES	50094.6397	0.6110	0.0054	-	-	-	-	-30.1582						
CES	50094.6491	0.6082	0.0087	-	-	-	-	-28.4621						
CES	50094.6575	0.5893	0.0024	-	-	-	-	-27.9778						
CES	50094.6655	0.5727	0.0021	-	-	-	-	-29.2065						
CES	50094.6746	0.5683	0.0140	-	-	-	-	-27.6866						
CES	50094.6895	0.5262	0.0001	-	-	-	-	-26.7921						
CES	50094.6974	0.5118	0.0007	-	-	-	-	-26.4002						
CES	50094.7051	0.4630	0.0086	-	-	-	-	-24.8425						
CES	50094.7131	0.4115	0.0051	-	-	-	-	-23.4251						
CES	50094.7206	0.3953	0.0003	-	-	-	-	-22.9969						
CES	50094.7280	0.3470	0.0024	-	-	-	-	-21.9697						
CES	50094.7361	0.3195	0.0049	-	-	-	-	-20.1839						
CES	50094.7434	0.2733	0.0045	-	-	-	-	-17.9093						
CES	50094.7509	0.2089	0.0009	-	-	-	-	-16.4559						
CES	50094.7591	0.1830	0.0080	-	-	-	-	-17.2425						
CES	50094.7667	0.1213	0.0012	-	-	-	-	-13.1634						
CES	50094.7743	0.1158	0.0068	-	-	-	-	-11.9172						
CES	50094.7992	0.0177	0.0007	-	-	-	-	-4.3483						
CES	50094.8063	-0.0289	0.0035	-	-	-	-	-3.7699						
CES	50094.8199	-0.1227	0.0052	-	-	-	-	0.2583						
CES	50094.8271	-0.1510	0.0275	-	-	-	-	2.6133						
CES	50095.5196	0.0668	0.0009	-	-	-	-	7.8116						

Instr.	T [RJD]	$\mathrm{RV_n}$ [km/s]	$\sigma_{\mathrm{RV_n}}$ [km/s]	V [loc. con.]	R [loc. con.]	V/R	$\frac{1}{2}(V+R)$ [loc. con.]	BVS [km/s]	Group, T_{loc} [RJD]	Number of RV	OC_{RV} [RJD]	$\sigma_{OC_{\mathrm{RV}}}$ [RJD]	OC_{BVS} [RJD]	$\sigma_{OC_{\mathrm{BVS}}}$ [RJD]
CES	50095.5270	0.0917	0.0014	-	-	-	-	5.5566						
CES	50095.5345	0.0962	0.0012	-	-	-	-	2.4196						
CES	50095.5426	0.1395	0.0066	-	-	-	-	3.0573						
CES	50095.5499	0.1484	0.0049	-	-	-	-	1.2935						
CES	50095.5569	0.1739	0.0007	-	-	-	-	0.5429						
CES	50095.5637	0.1739	0.0066	-	-	-	-	-1.0643						
CES	50095.5702	0.1899	0.0107	-	-	-	-	-1.7720						
CES	50095.5772	0.2327	0.0003	-	-	-	-	-3.3745						
CES	50095.5836	0.2185	0.0028	-	-	-	-	-4.2960						
CES	50095.5900	0.2451	0.0051	-	-	-	-	-3.4373						
CES	50095.5963	0.2492	0.0054	-	-	-	-	-3.6997						
CES	50095.6023	0.2758	0.0007	-	-	-	-	-2.8879						
CES	50095.6172	0.2866	0.0184	-	-	-	-	-5.6943						
CES	50095.6233	0.3179	0.0226	-	-	-	-	-5.9134						
CES	50095.6290	0.3395	0.0009	-	-	-	-	-7.7896						
CES	50095.6348	0.3223	0.0042	-	-	-	-	-6.8355						
CES	50095.6405	0.7736	0.0007	-	-	-	-	-7.5825						
CES	50095.6462	0.7701	0.0010	-	-	-	-	-9.6922						
CES	50095.6524	0.5242	0.0115	-	-	-	-	-10.0557						
CES	50095.6582	0.5302	0.0040	-	-	-	-	-10.2353						
CES	50095.6638	0.5573	0.0003	-	-	-	-	-11.2384						
CES	50095.6695	0.5732	0.0001	-	-	-	-	-10.8545						
CES	50095.6753	0.6054	0.0009	-	-	-	-	-12.1155						
CES	50095.6818	0.6042	0.0163	-	-	-	-	-10.5445						
CES	50095.6875	0.6282	0.0355	-	-	-	-	-14.3895						
CES	50095.6933	0.6521	0.0007	-	-	-	-	-15.4954						
CES	50095.6989	0.6521	0.0114	-	-	-	-	-12.6658						
CES	50095.7047	0.7038	0.0163	-	-	-	-	-15.5471						
CES	50095.7104	0.7006	0.0212	-	-	-	-	-16.1139						
CES	50095.7312	0.8082	0.0009	-	-	-	-	-18.6303						
CES	50095.7369	0.8660	0.0203	-	-	-	-	-20.2209						
CES	50095.7426	0.8061	0.0003	-	-	-	-	-21.9014						
CES	50095.7483	0.8511	0.0138	-	-	-	-	-22.4318						

Instr.	T [RJD]	$\mathrm{RV_n}$ [km/s]	$\sigma_{\mathrm{RV_n}}$ [km/s]	V [loc. con.]	R [loc. con.]	V/R	$\frac{1}{2}(V+R)$ [loc. con.]	BVS [km/s]	Group, T_{loc} [RJD]	Number of RV	OC_{RV} [RJD]	$\sigma_{OC_{\mathrm{RV}}}$ [RJD]	OC_{BVS} [RJD]	$\sigma_{OC_{\mathrm{BVS}}}$ [RJD]
CES	50095.7541	0.8824	0.0009	-	-	-	-	-26.2517						
CES	50095.7606	0.8793	0.0010	-	-	-	-	-27.1865						
CES	50095.7667	0.8728	0.0070	-	-	-	-	-26.5863						
CES	50095.7727	0.9209	0.0001	-	-	-	-	-27.8472						
CES	50095.7791	0.9067	0.0009	-	-	-	-	-29.6341						
CES	50095.7858	0.9195	0.0003	-	-	-	-	-32.9848						
CES	50095.7989	0.9538	0.0107	-	-	-	-	-32.8103						
CES	50095.8057	0.9608	0.0196	-	-	-	-	-33.7807						
CES	50095.8124	0.9888	0.0003	-	-	-	-	-33.8472						
CES	50095.8251	0.9967	0.0024	-	-	-	-	-35.6678						
CES	50095.8319	1.0000	0.0002	-	-	-	-	-35.0947						
CES	50097.6042	-0.0332	0.0114	-	-	-	-	3.7119						
CES	50097.6113	-0.1104	0.0187	-	-	-	-	5.5703						
CES	50097.6179	-0.1125	0.0058	-	-	-	-	4.9317						
CES	50097.6236	-0.1601	0.0017	-	-	-	-	6.5234						
CES	50097.6292	-0.1710	0.0182	-	-	-	-	7.6171						
CES	50097.6348	-0.1879	0.0072	-	-	-	-	11.6753						
CES	50097.6404	-0.2149	0.0154	-	-	-	-	9.0242						
CES	50097.6465	-0.2150	0.0010	-	-	-	-	11.0310						
CES	50097.6523	-0.2143	0.0066	-	-	-	-	11.0792						
CES	50097.6581	-0.2756	0.0019	-	-	-	-	11.0831						
CES	50097.6637	-0.2919	0.0001	-	-	-	-	12.1288						
CES	50097.6695	-0.2985	0.0003	-	-	-	-	14.8927						
CES	50097.6759	-0.3528	0.0007	-	-	-	-	15.8950						
CES	50097.6893	-0.3867	0.0009	-	-	-	-	15.5245						
CES	50097.7052	-0.5001	0.0003	-	-	-	-	19.3374						
CES	50097.7109	-0.4938	0.0007	-	-	-	-	20.2535						
CES	50097.7166	-0.5284	0.0035	-	-	-	-	20.4629						
CES	50097.7224	-0.5526	0.0009	-	-	-	-	22.8893						
CES	50097.7283	-0.5638	0.0003	-	-	-	-	25.0663						
CES	50097.7393	-0.6000	0.0007	-	-	-	-	26.2497						
CES	50097.7454	-0.6105	0.0021	-	-	-	-	27.3333						
CES	50097.7514	-0.6269	0.0063	-	-	-	-	29.1143						

Instr.	T [RJD]	$\mathrm{RV_n}$ [km/s]	$\sigma_{\mathrm{RV_n}}$ [km/s]	V [loc. con.]	R [loc. con.]	V/R	$\frac{1}{2}(V+R)$ [loc. con.]	BVS [km/s]	Group, T_{loc} [RJD]	Number of RV	OC_{RV} [RJD]	$\sigma_{OC_{\mathrm{RV}}}$ [RJD]	OC_{BVS} [RJD]	$\sigma_{OC_{\mathrm{BVS}}}$ [RJD]
CES	50097.7575	-0.6143	0.0001	-	-	-	-	30.5679						
CES	50097.7635	-0.6665	0.0010	-	-	-	-	30.2607						
CES	50097.7701	-0.6455	0.0007	-	-	-	-	31.2210						
CES	50097.7760	-0.7008	0.0142	-	-	-	-	32.1710						
CES	50097.7818	-0.7064	0.0108	-	-	-	-	32.4974						
CES	50097.7877	-0.7433	0.0001	-	-	-	-	33.4426						
CES	50097.7937	-0.7183	0.0012	-	-	-	-	36.2798						
CES	50097.8002	-0.7235	0.0009	-	-	-	-	34.2726						
CES	50097.8061	-0.7710	0.0117	-	-	-	-	36.0291						
CES	50097.8213	-0.8059	0.0009	-	-	-	-	37.3210						
CES	50097.8271	-0.8073	0.0003	-	-	-	-	37.5534						
CES	50097.8329	-0.7939	0.0003	-	-	-	-	36.4112						
CES	50098.5176	0.9332	0.0003	-	-	-	-	-34.7240						
CES	50098.5311	0.9269	0.0052	-	-	-	-	-33.9481						
CES	50098.5374	0.9388	0.0001	-	-	-	-	-37.0610						
CES	50098.5437	0.9314	0.0003	-	-	-	-	-36.9477						
CES	50098.5500	0.9374	0.0009	-	-	-	-	-34.0790						
CES	50098.5553	0.9307	0.0009	-	-	-	-	-36.8438						
CES	50098.5604	0.9351	0.0009	-	-	-	-	-34.2810						
CES	50098.5665	0.9349	0.0206	-	-	-	-	-36.3030						
CES	50098.5716	0.9197	0.0126	-	-	-	-	-37.2082						
CES	50098.5767	0.8866	0.0003	-	-	-	-	-36.3088						
CES	50098.5819	0.9263	0.0205	-	-	-	-	-32.4807						
CES	50098.5870	0.9442	0.0001	-	-	-	-	-34.1982						
CES	50098.6007	0.9088	0.0255	-	-	-	-	-35.1902						
CES	50098.6056	0.9104	0.0159	-	-	-	-	-32.9188						
CES	50098.6105	0.9069	0.0003	-	-	-	-	-33.8842						
CES	50098.6154	0.9031	0.0007	-	-	-	-	-31.2006						
CES	50098.6268	0.8677	0.0007	-	-	-	-	-31.6268						
CES	50098.6322	0.9083	0.0287	-	-	-	-	-30.7165						
CES	50098.6370	0.9039	0.0110	-	-	-	-	-29.1633						
CES	50098.6420	0.8691	0.0003	-	-	-	-	-27.4842						
CES	50098.6469	0.8815	0.0007	-	-	-	-	-31.2797						

Instr.	T [RJD]	$\mathrm{RV_n}$ [km/s]	$\sigma_{\mathrm{RV_n}}$ [km/s]	V [loc. con.]	R [loc. con.]	V/R	$\frac{1}{2}(V+R)$ [loc. con.]	BVS [km/s]	Group, T_{loc} [RJD]	Number of RV	OC_{RV} [RJD]	$\sigma_{OC_{\mathrm{RV}}}$ [RJD]	OC_{BVS} [RJD]	$\sigma_{OC_{\mathrm{BVS}}}$ [RJD]
CES	50098.6518	0.8530	0.0014	-	-	-	-	-29.5631						
CES	50098.6568	0.8686	0.0003	-	-	-	-	-30.6989						
CES	50098.6617	0.8609	0.0010	-	-	-	-	-28.3873						
CES	50098.6665	0.8530	0.0009	-	-	-	-	-28.1910						
CES	50098.6714	0.8695	0.0210	-	-	-	-	-29.1123						
CES	50098.6763	0.8154	0.0021	-	-	-	-	-26.9297						
CES	50098.6947	0.7428	0.0003	-	-	-	-	-27.2857						
CES	50098.7007	0.7753	0.0159	-	-	-	-	-25.8979						
CES	50098.7057	0.6835	0.0348	-	-	-	-	-24.2348						
CES	50098.7107	0.6875	0.0380	-	-	-	-	-22.4122						
CES	50098.7157	0.7482	0.0005	-	-	-	-	-24.8379						
CES	50098.7207	0.7276	0.0236	-	-	-	-	-22.1299						
CES	50098.7260	0.5911	0.0010	-	-	-	-	-22.4117						
CES	50098.7429	0.6131	0.0385	-	-	-	-	-19.9959						
CES	50098.7487	0.5804	0.0567	-	-	-	-	-18.6740						
CES	50098.7537	0.5486	0.0343	-	-	-	-	-21.0171						
CES	50098.7587	0.5062	0.0229	-	-	-	-	-19.5540						
CES	50098.7638	0.5708	0.0003	-	-	-	-	-20.4224						
CES	50098.8261	0.3722	0.0122	-	-	-	-	-16.9984						
CES	50098.8312	0.3414	0.0003	-	-	-	-	-13.9867						
CES	50098.8365	0.3351	0.0304	-	-	-	-	-10.7136						
CES	50099.5336	-0.2182	0.0009	-	-	-	-	14.6825						
CES	50099.5397	-0.2306	0.0135	-	-	-	-	16.5124						
CES	50099.5457	-0.1934	0.0108	-	-	-	-	16.5302						
CES	50099.5521	-0.1787	0.0003	-	-	-	-	14.9232						
CES	50099.5587	-0.1323	0.0010	-	-	-	-	12.7710						
CES	50099.5648	-0.1216	0.0009	-	-	-	-	12.1723						
CES	50099.5708	-0.1080	0.0024	-	-	-	-	10.9627						
CES	50099.5774	-0.0924	0.0012	-	-	-	-	11.0410						
CES	50099.5835	-0.0616	0.0072	-	-	-	-	9.8985						
CES	50099.5895	-0.0397	0.0007	-	-	-	-	8.1925						
CES	50099.5954	-0.0324	0.0031	-	-	-	-	7.0792						
CES	50099.6013	-0.0084	0.0065	-	-	-	-	5.0785						

Instr.	T [RJD]	$\mathrm{RV_n}$ [km/s]	$\sigma_{\mathrm{RV_n}}$ [km/s]	V [loc. con.]	R [loc. con.]	V/R	$\frac{1}{2}(V+R)$ [loc. con.]	BVS [km/s]	Group, T_{loc} [RJD]	Number of RV	OC_{RV} [RJD]	$\sigma_{OC_{\mathrm{RV}}}$ [RJD]	OC_{BVS} [RJD]	$\sigma_{OC_{\mathrm{BVS}}}$ [RJD]
CES	50099.6230	0.0320	0.0030	-	-	-	-	3.5692						
CES	50099.6296	0.0658	0.0016	-	-	-	-	2.7025						
CES	50099.6359	0.0971	0.0038	-	-	-	-	1.3833						
CES	50099.6415	0.1134	0.0065	-	-	-	-	1.1912						
CES	50099.6472	0.1393	0.0017	-	-	-	-	-1.1811						
CES	50099.6530	0.1465	0.0007	-	-	-	-	-1.0311						
CES	50099.6588	0.1647	0.0007	-	-	-	-	-3.2819						
CES	50099.6651	0.2016	0.0072	-	-	-	-	-4.2368						
CES	50099.6709	0.1914	0.0009	-	-	-	-	-2.6188						
CES	50099.6767	0.2304	0.0010	-	-	-	-	-5.0992						
CES	50099.6825	0.2467	0.0142	-	-	-	-	-4.3248						
CES	50099.6883	0.2637	0.0007	-	-	-	-	-7.2912						
CES	50099.7027	0.3179	0.0009	-	-	-	-	-9.3202						
CES	50099.7089	0.1444	0.0024	-	-	-	-	-8.2992						
CES	50099.7154	0.1792	0.0012	-	-	-	-	-11.1055						
CES	50099.7277	0.0800	0.0003	-	-	-	-	-10.9296						
CES	50099.7344	0.3594	0.0082	-	-	-	-	-12.1274						
CES	50099.7410	0.3673	0.0084	-	-	-	-	-11.6914						
CES	50099.7477	0.3662	0.0257	-	-	-	-	-12.9817						
CES	50099.7543	0.4346	0.0066	-	-	-	-	-13.3710						
CES	50099.7611	0.4203	0.0080	-	-	-	-	-14.1669						
CES	50099.7679	0.4469	0.0198	-	-	-	-	-16.7533						
CES	50099.7746	0.4427	0.0166	-	-	-	-	-16.1904						
CES	50099.7814	0.4521	0.0096	-	-	-	-	-15.5029						
CES	50099.7880	0.4899	0.0010	-	-	-	-	-15.8383						
CES	50099.8005	0.4971	0.0065	-	-	-	-	-17.0834						
CES	50099.8069	0.5011	0.0007	-	-	-	-	-18.0138						
CES	50099.8133	0.5370	0.0075	-	-	-	-	-19.4826						
CES	50099.8247	0.5395	0.0010	-	-	-	-	-19.0572						
CES	50099.8311	0.5617	0.0003	-	-	-	-	-21.5961						
CES	50099.8373	0.6054	0.0003	-	-	-	-	-22.2687						
CES	50100.5245	-0.7883	0.0003	-	-	-	-	29.9492						
CES	50100.5316	-0.8231	0.0005	-	-	-	-	32.6288						

Instr.	T [RJD]	$\mathrm{RV_n}$ [km/s]	$\sigma_{\mathrm{RV_n}}$ [km/s]	V [loc. con.]	R [loc. con.]	V/R	$\frac{1}{2}(V+R)$ [loc. con.]	BVS [km/s]	Group, T_{loc} [RJD]	Number of RV	OC_{RV} [RJD]	$\sigma_{OC_{\mathrm{RV}}}$ [RJD]	OC_{BVS} [RJD]	$\sigma_{OC_{\mathrm{BVS}}}$ [RJD]
CES	50100.5391	-0.8143	0.0010	-	-	-	-	32.2233						
CES	50100.5462	-0.8327	0.0056	-	-	-	-	34.3523						
CES	50100.5532	-0.8178	0.0023	-	-	-	-	33.5275						
CES	50100.5606	-0.8556	0.0007	-	-	-	-	34.9451						
CES	50100.5675	-0.8465	0.0079	-	-	-	-	34.2769						
CES	50100.5744	-0.8616	0.0007	-	-	-	-	35.0007						
CES	50100.5812	-0.8684	0.0010	-	-	-	-	35.3445						
CES	50100.5882	-0.8700	0.0084	-	-	-	-	34.7071						
CES	50100.5954	-0.9025	0.0100	-	-	-	-	37.1511						
CES	50100.6019	-0.9125	0.0129	-	-	-	-	37.5062						
CES	50100.6086	-0.9386	0.0010	-	-	-	-	37.9635						
CES	50100.6322	-0.9799	0.0007	-	-	-	-	39.5472						
CES	50100.6384	-0.9906	0.0007	-	-	-	-	37.9416						
CES	50100.6445	-0.9767	0.0128	-	-	-	-	38.7950						
CES	50100.6507	-0.9904	0.0002	-	-	-	-	39.5357						
CES	50100.6568	-1.0000	0.0031	-	-	-	-	38.7540						
CES	50100.6635	-0.9888	0.0217	-	-	-	-	39.0654						
CES	50100.6696	-0.9795	0.0005	-	-	-	-	40.4519						
CES	50100.6756	-0.9549	0.0001	-	-	-	-	39.6085						
CES	50100.6817	-0.9918	0.0007	-	-	-	-	39.6139						
CES	50100.6878	-0.9871	0.0001	-	-	-	-	40.7564						
CES	50100.7021	-0.9890	0.0058	-	-	-	-	39.8171						
CES	50100.7086	-0.9543	0.0009	-	-	-	-	36.5305						
CES	50100.7152	-0.9871	0.0007	-	-	-	-	37.3313						
CES	50100.7221	-0.9536	0.0007	-	-	-	-	37.5837						
CES	50100.7288	-0.9482	0.0003	-	-	-	-	34.6461						
CES	50100.7370	-0.8731	0.0219	-	-	-	-	33.3714						
CES	50100.7435	-0.8838	0.0098	-	-	-	-	33.1356						
CES	50100.7501	-0.8051	0.0273	-	-	-	-	31.4923						
CES	50100.7645	-0.7773	0.0003	-	-	-	-	29.2559						
CES	50100.7713	-0.7402	0.0425	-	-	-	-	30.1591						
CES	50100.7786	-0.6989	0.0177	-	-	-	-	28.1397						
CES	50100.7853	-0.7092	0.0504	-	-	-	-	29.3005						

Instr.	T [RJD]	RV_n [km/s]	σ_{RV_n} [km/s]	V [loc. con.]	R [loc. con.]	V/R	$\frac{1}{2}(V+R)$ [loc. con.]	BVS [km/s]	Group, T_{loc} [RJD]	Number of RV	OC_{RV} [RJD]	$\sigma_{OC_{RV}}$ [RJD]	OC_{BVS} [RJD]	$\sigma_{OC_{BVS}}$ [RJD]
CES	50100.7922	-0.6411	0.0003	-	-	-	-	26.3714						
CES	50100.8083	-0.5906	0.0012	-	-	-	-	25.7422						
CES	50100.8156	-0.5953	0.0114	-	-	-	-	24.6866						
CES	50100.8292	-0.5535	0.0001	-	-	-	-	24.1081						
CES	50100.8368	-0.5528	0.0007	-	-	-	-	23.8731	50095.8585					
HER	50102.5924	0.9936	0.0085	4.2599	4.2184	1.0098	4.2392	-24.3500		7	0.0290	0.0230	0.6971	0.0210
HER	50103.5903	-0.2619	0.0503	4.2895	4.2474	1.0099	4.2685	26.2010	15					
HER	50107.5850	-0.7105	0.0284	4.2100	4.2286	0.9956	4.2193	24.0477						
HER	50108.5331	0.3862	0.0260	4.1477	4.1112	1.0089	4.1295	2.4639						
HER	50108.7620	-0.4443	0.0036	4.0770	4.1060	0.9929	4.0915	29.4701						
HER	50109.5345	1.0000	0.0203	4.2227	4.2153	1.0018	4.2190	-28.9559						
HER	50109.7681	0.6568	0.0798	4.1677	4.1673	1.0001	4.1675	-10.3495	50109.5750					
HER	50110.5308	-0.0175	0.0114	4.2333	4.3158	0.9809	4.2746	-0.4837		12	0.0397	0.0190	0.6896	0.0190
HER	50110.7612	0.3432	0.0028	4.2339	4.2743	0.9905	4.2541	-10.2051	16					
HER	50111.5591	-0.5612	0.0003	4.1330	4.1542	0.9949	4.1436	38.5269						
HER	50112.5324	0.5732	0.0005	4.1417	4.0986	1.0105	4.1202	-9.3932						
HER	50112.7668	-0.1982	0.0002	4.0075	3.9844	1.0058	3.9960	29.0310						
HER	50113.5301	0.6861	0.0005	4.2147	4.2147	1.0000	4.2147	-34.3473						
HER	50113.7639	0.9461	0.0416	4.2263	4.2263	1.0000	4.2263	-35.4844						
HER	50114.5321	-0.3918	0.0003	4.1205	4.1211	0.9999	4.1208	30.5647						
HER	50114.7677	0.3084	0.0014	4.2167	4.2356	0.9955	4.2262	-14.5037						
HER	50115.5377	-0.1793	0.0003	4.1887	4.1755	1.0032	4.1821	29.8429						
HER	50116.5540	0.8189	0.0635	4.2169	4.2146	1.0005	4.2158	-38.1040						
HER	50116.7901	-0.0049	0.0005	4.2016	4.1876	1.0033	4.1946	-1.2902	50113.7020					
HER	50117.5370	0.2187	0.0014	4.3353	4.3135	1.0051	4.3244	-2.3536		14	0.0472	0.0170	0.7653	0.013
HER	50117.7777	0.7159	0.0009	4.3331	4.3337	0.9999	4.3334	-25.3268	17					
HER	50118.5433	-0.6275	0.1214	4.3608	4.3686	0.9982	4.3647	31.9526						
HER	50118.7793	-0.1100	0.0408	4.2295	4.2556	0.9939	4.2426	18.9102						
HER	50119.5365	-0.0525	0.0001	4.2156	4.2552	0.9907	4.2354	-3.2487						
HER	50119.7682	-0.6431	0.0009	4.1670	4.2123	0.9892	4.1897	27.6593						
HER	50120.5242	0.7806	0.0401	4.2525	4.2890	0.9915	4.2708	-21.5553						
HER	50120.7643	0.3897	0.0016	4.1485	4.1862	0.9910	4.1674	-25.5124						
HER	50121.5222	-0.2211	0.0520	4.3082	4.3621	0.9876	4.3352	18.0286						

Instr.	T [RJD]	$\mathrm{RV_n}$ [km/s]	$\sigma_{\mathrm{RV_n}}$ [km/s]	V [loc. con.]	R [loc. con.]	V/R	$\frac{1}{2}(V+R)$ [loc. con.]	BVS [km/s]	Group, T_{loc} [RJD]	Number of RV	OC_{RV} [RJD]	$\sigma_{OC_{\mathrm{RV}}}$ [RJD]	OC_{BVS} [RJD]	$\sigma_{OC_{\mathrm{BVS}}}$ [RJD]
HER	50121.7618	0.5388	0.0002	4.2196	4.2469	0.9936	4.2333	-4.6608						
HER	50122.5253	-0.7612	0.0007	4.2651	4.2651	1.0000	4.2651	35.4893						
HER	50122.7685	-0.6885	0.0012	4.2835	4.3629	0.9818	4.3232	30.7606						
HER	50123.5226	0.7196	0.0007	4.1327	4.1291	1.0009	4.1309	-10.3423						
HER	50123.7575	-0.2291	0.0002	4.0550	4.1283	0.9822	4.0917	16.3552	50120.5700					
HER	50124.5187	0.4148	0.0101	4.3382	4.3485	0.9976	4.3433	-12.8956		13	0.1230	0.0120	0.7339	0.0230
HER	50124.7613	0.8271	0.0354	4.1904	4.1904	1.0000	4.1904	-23.5137	18					
HER	50125.5201	-0.7508	0.1576	4.1778	4.1778	1.0000	4.1778	21.6740						
HER	50125.8011	0.1051	0.0003	4.2551	4.2551	1.0000	4.2551	3.6559						
HER	50126.5173	-0.1332	0.0094	3.9448	3.9291	1.0040	3.9370	16.1018						
HER	50126.7641	-0.7102	0.0012	4.0459	4.0459	1.0000	4.0459	28.0888						
HER	50127.5211	0.9076	0.0217	4.2481	4.2481	1.0000	4.2481	-28.6775						
HER	50127.7721	0.3970	0.0262	4.0628	4.0935	0.9925	4.0782	-4.0850						
HER	50128.5657	-0.0120	0.0182	4.2490	4.2490	1.0000	4.2490	-17.1957						
HER	50129.5221	-0.8906	0.0012	4.2860	4.2860	1.0000	4.2860	36.3145						
HER	50129.7638	-0.5080	0.0441	4.1221	4.1221	1.0000	4.1221	14.8652						
HER	50130.5330	0.1245	0.0042	4.1614	4.1551	1.0015	4.1583	20.1736						
HER	50130.7729	-0.7161	0.0269	4.1076	4.1076	1.0000	4.1076	39.2437	50124.7620					
HER	50131.5144	0.7277	0.0751	4.2363	4.2363	1.0000	4.2363	-42.9301		14	0.0955	0.0200	0.4773	0.0091
HER	50131.7534	0.5879	0.0375	4.1282	4.1282	1.0000	4.1282	-23.4065	19					
HER	50132.5104	-0.4157	0.0193	4.2326	4.2326	1.0000	4.2326	6.9750						
HER	50132.7477	0.2126	0.0553	4.2054	4.2054	1.0000	4.2054	-35.6290						
HER	50133.5260	-0.7104	0.0001	4.0733	4.0733	1.0000	4.0733	45.7853						
HER	50133.7633	-0.6492	0.0413	4.1619	4.1619	1.0000	4.1619	28.8532						
HER	50134.5127	0.3670	0.0917	4.2384	4.2397	0.9997	4.2391	-16.4297						
HER	50134.7500	-0.2489	0.0114	4.1406	4.1406	1.0000	4.1406	28.3481						
HER	50135.5257	0.2478	0.0338	4.3268	4.3268	1.0000	4.3268	-26.8017						
HER	50135.7636	0.6760	0.0095	4.2788	4.2788	1.0000	4.2788	-44.3330						
HER	50136.5110	-0.6434	0.0765	4.1819	4.1819	1.0000	4.1819	37.8938						
HER	50136.7606	0.0080	0.0269	4.2374	4.2374	1.0000	4.2374	-14.0620						
HER	50137.5078	-0.5061	0.0727	4.2718	4.2718	1.0000	4.2718	27.8311						
HER	50137.7485	-0.7478	0.0661	4.2619	4.2619	1.0000	4.2619	50.6957	50131.5950					
HER	50138.5153	0.6112	0.0744	4.2718	4.2718	1.0000	4.2718	-24.6859		11	0.0577	0.0190	0.5251	0.0260
									20					

Instr.	T [RJD]	RV_n [km/s]	σ_{RV_n} [km/s]	V [loc. con.]	R [loc. con.]	V/R	$\frac{1}{2}(V+R)$ [loc. con.]	BVS [km/s]	Group, T_{loc} [RJD]	Number of RV	OC_{RV} [RJD]	$\sigma_{OC_{RV}}$ [RJD]	OC_{BVS} [RJD]	$\sigma_{OC_{BVS}}$ [RJD]
HER	50138.7454	-0.1271	0.0021	4.3141	4.3141	1.0000	4.3141	1.0187						
HER	50139.5194	0.0416	0.0241	4.1472	4.1472	1.0000	4.1472	6.3502						
HER	50139.6057	0.2400	0.0184	4.1086	4.1086	1.0000	4.1086	1.9610						
HER	50140.5153	-0.7549	0.0675	4.2681	4.2681	1.0000	4.2681	40.9253						
HER	50140.7527	-0.3675	0.0114	4.2521	4.2591	0.9984	4.2556	19.2980						
HER	50141.5098	-0.2301	0.0036	4.0675	4.0675	1.0000	4.0675	0.1631						
HER	50141.7458	-0.8956	0.0014	4.1128	4.1128	1.0000	4.1128	35.3304						
HER	50142.5124	0.4766	0.0005	4.0430	4.0430	1.0000	4.0430	-17.8292						
HER	50142.7569	0.1400	0.0082	3.8722	3.8722	1.0000	3.8722	-3.5185						
HER	50143.5312	-0.3798	0.0085	4.2108	4.2108	1.0000	4.2108	-2.0997	50142.5340					
HER	50144.5060	-0.8751	0.0009	3.8549	3.8549	1.0000	3.8549	35.5276		9	0.1415	0.0280	0.5244	0.0330
HER	50145.5067	0.2662	0.0441	3.8915	3.8915	1.0000	3.8915	-6.3079	21					
HER	50145.7484	-0.6108	0.0019	3.7673	3.7673	1.0000	3.7673	42.6586						
HER	50146.5037	0.0926	0.0368	4.0741	4.0741	1.0000	4.0741	-24.1129						
HER	50146.7476	0.3578	0.0005	4.0354	4.0354	1.0000	4.0354	-40.6693						
HER	50147.5559	-0.7653	0.0023	3.7746	3.7746	1.0000	3.7746	36.5639						
HER	50148.5767	-0.3902	0.0010	3.6800	3.6800	1.0000	3.6800	18.7759						
HER	50149.5803	0.4228	0.0305	3.8632	3.8632	1.0000	3.8632	-33.1635						
HER	50150.5478	-0.1016	0.0924	3.6242	3.6242	1.0000	3.6242	-14.0310	50146.7340					
HER	50151.5691	-1.0000	0.0007	3.7705	3.7705	1.0000	3.7705	47.1714		6	0.0297	0.0270	0.7654	0.040
HER	50152.5544	-0.7007	0.0023	3.5974	3.5974	1.0000	3.5974	36.3108	22					
HER	50153.5839	0.5555	0.0184	3.4883	3.4883	1.0000	3.4883	-53.7508						
HER	50155.5575	-0.9318	0.0023	3.5999	3.5999	1.0000	3.5999	46.0847						
HER	50156.5652	-0.1247	0.0498	3.6525	3.6525	1.0000	3.6525	-18.8867						
HER	50157.5567	0.5598	0.0012	3.5959	3.5959	1.0000	3.5959	-41.0307	50157.5990					
HER	50185.5348	-0.7808	0.0158	4.1090	4.1090	1.0000	4.1090	23.0822		4	0.0046	0.0080	0.7440	0.0270
HER	50189.5208	-0.3186	0.0047	4.0274	4.0274	1.0000	4.0274	5.1709	23					
HER	50190.5148	0.8321	0.1393	4.0613	4.0613	1.0000	4.0613	-16.7696						
HER	50191.5076	-0.1988	0.0172	4.1942	4.1942	1.0000	4.1942	8.1635	50190.5041					
HER	50194.5244	0.5503	0.0002	4.0635	4.0635	1.0000	4.0635	-26.1575		6	0.0322	0.0260	0.5267	0.0370
HER	50195.5229	-0.4325	0.0886	3.7664	3.7664	1.0000	3.7664	16.8508	24					
HER	50198.5079	0.0753	0.0227	3.7393	3.7393	1.0000	3.7393	-3.3972						
HER	50200.4988	-0.0411	0.0243	3.5749	3.5749	1.0000	3.5749	-0.0027						

Instr.	T [RJD]	RV_n [km/s]	σ_{RV_n} [km/s]	V [loc. con.]	R [loc. con.]	V/R	$\frac{1}{2}(V+R)$ [loc. con.]	BVS [km/s]	Group, T_{loc} [RJD]	Number of RV	OC_{RV} [RJD]	$\sigma_{OC_{RV}}$ [RJD]	OC_{BVS} [RJD]	$\sigma_{OC_{BVS}}$ [RJD]
HER	50202.5041	0.0210	0.0017	3.7457	3.7457	1.0000	3.7457	26.6966						
HER	50204.5009	0.3167	0.0208	3.7405	3.7405	1.0000	3.7405	-13.3991	50194.6480					
HER	50449.6218	0.4690	0.0002	6.4256	6.4256	1.0000	6.4256	-9.6767		7	0.0017	0.0260	0.6645	0.0230
HER	50450.6605	-0.3141	0.0624	6.7251	6.7251	1.0000	6.7251	17.9254	25					
HER	50451.5956	0.0806	0.0050	7.0980	7.0980	1.0000	7.0980	10.4261						
HER	50452.5951	1.0000	0.0130	6.6555	6.6555	1.0000	6.6555	-21.4977						
HER	50453.5931	0.1820	0.0092	6.6797	6.6797	1.0000	6.6797	-2.5832						
HER	50454.6099	-0.6780	0.1286	6.6646	6.6646	1.0000	6.6646	37.7223						
HER	50455.5888	0.3222	0.0013	6.6729	6.6729	1.0000	6.6729	-4.0922	50452.5710					
HER	50456.6102	0.6181	0.0002	6.7647	6.7647	1.0000	6.7647	-12.0236		28	-0.0068	0.0099	0.7159	0.0140
HER	50457.6102	-0.0658	0.0013	6.7256	6.7256	1.0000	6.7256	9.2462	26					
HER	50458.6603	-0.4414	0.0013	6.7692	6.7692	1.0000	6.7692	29.9511						
HER	50458.7036	-0.5886	0.0486	6.8071	6.8071	1.0000	6.8071	36.9403						
HER	50458.7333	-0.5511	0.0010	6.8065	6.8065	1.0000	6.8065	28.1508						
HER	50458.7628	-0.6778	0.1057	6.8665	6.8665	1.0000	6.8665	27.3899						
HER	50459.6211	0.6438	0.0228	6.7562	6.7562	1.0000	6.7562	-19.9772						
HER	50459.6617	0.5067	0.0044	6.7837	6.7837	1.0000	6.7837	-14.2462						
HER	50459.6983	0.3449	0.0067	6.8227	6.8227	1.0000	6.8227	-5.9009						
HER	50459.7278	0.2307	0.0011	6.8240	6.8240	1.0000	6.8240	-3.8587						
HER	50460.6506	0.4204	0.0745	6.8183	6.8183	1.0000	6.8183	-10.2109						
HER	50460.6945	0.5712	0.0586	6.7912	6.7912	1.0000	6.7912	-22.3898						
HER	50460.7241	0.6953	0.0002	6.8707	6.8707	1.0000	6.8707	-26.1474						
HER	50460.7548	0.7866	0.0021	6.8444	6.8444	1.0000	6.8444	-13.1374						
HER	50461.6072	-0.5362	0.0011	6.7920	6.7920	1.0000	6.7920	27.9763						
HER	50461.6455	-0.4240	0.0015	6.8375	6.8375	1.0000	6.8375	21.9761						
HER	50461.6750	-0.3298	0.0040	6.8608	6.8608	1.0000	6.8608	15.6122						
HER	50461.7085	-0.2102	0.0383	6.8679	6.8679	1.0000	6.8679	15.2104						
HER	50462.6574	-0.2559	0.0004	6.8332	6.8332	1.0000	6.8332	9.7025						
HER	50462.6988	-0.3099	0.0180	6.8425	6.8425	1.0000	6.8425	15.3719						
HER	50462.7281	-0.3484	0.0061	6.8356	6.8356	1.0000	6.8356	14.8076						
HER	50462.7575	-0.4437	0.0207	6.8239	6.8239	1.0000	6.8239	23.3450						
HER	50462.8538	-0.6418	0.0748	6.8189	6.8189	1.0000	6.8189	26.8098						
HER	50463.6069	0.8415	0.0021	6.7895	6.7895	1.0000	6.7895	-16.7113						

Instr.	T [RJD]	RV_n [km/s]	σ_{RV_n} [km/s]	V [loc. con.]	R [loc. con.]	V/R	$\frac{1}{2}(V+R)$ [loc. con.]	BVS [km/s]	Group, T_{loc} [RJD]	Number of RV	OC_{RV} [RJD]	$\sigma_{OC_{RV}}$ [RJD]	OC_{BVS} [RJD]	$\sigma_{OC_{BVS}}$ [RJD]
HER	50463.6425	0.4845	0.0010	6.8499	6.8499	1.0000	6.8499	-18.8768						
HER	50463.6718	0.5674	0.0013	6.8626	6.8626	1.0000	6.8626	-21.1644						
HER	50463.7071	0.6053	0.0804	6.8766	6.8766	1.0000	6.8766	-24.3532						
HER	50463.7528	0.6395	0.0056	6.7884	6.7884	1.0000	6.7884	-20.2100	50460.7950					
HER	50464.6437	0.0877	0.0433	6.8494	6.8494	1.0000	6.8494	-2.6824		26	0.0087	0.0160	0.6976	0.0084
HER	50464.6730	0.2180	0.0511	6.8985	6.8985	1.0000	6.8985	-4.1488	27					
HER	50464.7080	0.2739	0.0605	6.8974	6.8974	1.0000	6.8974	-7.7393						
HER	50464.7452	0.4608	0.0017	6.8705	6.8705	1.0000	6.8705	-18.6444						
HER	50465.6137	-0.8118	0.0033	6.8633	6.8633	1.0000	6.8633	28.0685						
HER	50465.6522	-0.6721	0.1371	6.7177	6.7177	1.0000	6.7177	24.1704						
HER	50465.6818	-0.7217	0.1095	6.8428	6.8428	1.0000	6.8428	24.4797						
HER	50465.7115	-0.5748	0.0010	6.8338	6.8338	1.0000	6.8338	23.2147						
HER	50465.7574	-0.4141	0.0149	6.8450	6.8450	1.0000	6.8450	15.7762						
HER	50466.6002	0.2494	0.0569	6.7855	6.7855	1.0000	6.7855	-6.5762						
HER	50466.7420	-0.2975	0.0691	6.8537	6.8537	1.0000	6.8537	13.9509						
HER	50466.7862	-0.2690	0.0620	6.7658	6.7658	1.0000	6.7658	18.1287						
HER	50467.5602	0.7121	0.0563	6.8478	6.8478	1.0000	6.8478	-29.5807						
HER	50467.6700	0.7188	0.0021	6.8438	6.8438	1.0000	6.8438	-34.8895						
HER	50467.7224	0.7090	0.1227	6.7725	6.7725	1.0000	6.7725	-29.0113						
HER	50467.8498	0.2676	0.0002	6.7850	6.7850	1.0000	6.7850	-13.1162						
HER	50468.5863	-0.3216	0.0657	6.7854	6.7854	1.0000	6.7854	15.4165						
HER	50468.6798	-0.0972	0.0038	6.8996	6.8996	1.0000	6.8996	5.5666						
HER	50468.7566	0.0392	0.0333	6.8479	6.8479	1.0000	6.8479	-3.3344						
HER	50468.8515	0.3827	0.0008	6.8098	6.8098	1.0000	6.8098	-15.2964						
HER	50469.5704	-0.5586	0.0025	6.7866	6.7866	1.0000	6.7866	23.6902						
HER	50469.7093	-0.5837	0.0006	6.8453	6.8453	1.0000	6.8453	25.7937						
HER	50469.8505	-0.5197	0.0004	6.6692	6.6692	1.0000	6.6692	23.0731						
HER	50470.6180	0.2121	0.0237	6.7464	6.7464	1.0000	6.7464	-13.7403						
HER	50470.7024	0.0517	0.0186	6.8520	6.8520	1.0000	6.8520	-6.5774						
HER	50470.8018	-0.3298	0.0001	6.7318	6.7318	1.0000	6.7318	7.3083	50467.6710					
HER	50471.5765	0.1652	0.0002	6.7735	6.7735	1.0000	6.7735	-11.7331		27	-0.0146	0.0160	0.6671	0.011
HER	50471.6577	0.4198	0.0235	6.8499	6.8499	1.0000	6.8499	-19.3311	28					
HER	50471.7473	0.5632	0.0461	6.8306	6.8306	1.0000	6.8306	-15.7270						

Instr.	T [RJD]	RV_n [km/s]	σ_{RV_n} [km/s]	V [loc. con.]	R [loc. con.]	V/R	$\frac{1}{2}(V+R)$ [loc. con.]	BVS [km/s]	Group, T_{loc} [RJD]	Number of RV	OC_{RV} [RJD]	$\sigma_{OC_{RV}}$ [RJD]	OC_{BVS} [RJD]	$\sigma_{OC_{BVS}}$ [RJD]
HER	50471.8293	0.6878	0.0013	6.7538	6.7538	1.0000	6.7538	-27.8525						
HER	50472.5802	-0.6036	0.0814	6.7905	6.7905	1.0000	6.7905	23.7648						
HER	50472.6610	-0.3507	0.0358	6.8081	6.8081	1.0000	6.8081	13.2355						
HER	50472.7468	-0.2280	0.0609	6.8220	6.8220	1.0000	6.8220	8.1365						
HER	50472.8355	-0.0471	0.0178	6.7146	6.7146	1.0000	6.7146	-3.7946						
HER	50473.5447	-0.2259	0.0203	6.6117	6.6117	1.0000	6.6117	39.2705						
HER	50473.5846	-0.3199	0.1024	6.6554	6.6554	1.0000	6.6554	9.0698						
HER	50473.6807	-0.7797	0.0010	6.8140	6.8140	1.0000	6.8140	27.2607						
HER	50473.8093	-0.5119	0.0511	6.7589	6.7589	1.0000	6.7589	24.6291						
HER	50474.5749	0.5312	0.0371	6.8437	6.8437	1.0000	6.8437	-26.1808						
HER	50474.6556	0.3055	0.0835	6.7388	6.7388	1.0000	6.7388	-16.4132						
HER	50474.6978	0.2368	0.0056	6.8125	6.8125	1.0000	6.8125	-15.0730						
HER	50474.7635	0.1106	0.0002	6.7886	6.7886	1.0000	6.7886	-11.3939						
HER	50475.5596	-0.0647	0.0002	6.8140	6.8140	1.0000	6.8140	-3.6247						
HER	50475.6569	0.1164	0.0008	6.7758	6.7758	1.0000	6.7758	-11.8014						
HER	50475.7257	0.2676	0.0001	6.8155	6.8155	1.0000	6.8155	-17.4779						
HER	50475.8285	0.4336	0.0002	6.7582	6.7582	1.0000	6.7582	-27.8418						
HER	50476.5679	-0.8815	0.0071	6.7750	6.7750	1.0000	6.7750	42.5276						
HER	50476.6593	-0.9342	0.0002	6.8917	6.8917	1.0000	6.8917	26.6782						
HER	50476.7397	-0.7716	0.0882	6.8156	6.8156	1.0000	6.8156	15.7263						
HER	50477.5686	-0.2575	0.0029	6.8425	6.8425	1.0000	6.8425	-4.5454						
HER	50477.6488	-0.4548	0.0159	6.8542	6.8542	1.0000	6.8542	4.3996						
HER	50477.7493	-0.8038	0.0015	6.8800	6.8800	1.0000	6.8800	23.4857						
HER	50477.8303	-1.0000	0.0044	6.8067	6.8067	1.0000	6.8067	29.1456	50471.7640					
HER	50515.5418	0.0441	0.0029	7.1164	7.1164	1.0000	7.1164	-8.4831		9	-0.0076	0.0410	0.4957	0.033
HER	50515.6811	0.3488	0.0009	7.2715	7.2715	1.0000	7.2715	3.9204	29					
HER	50516.5336	-0.7827	0.0005	7.2151	7.2151	1.0000	7.2151	29.3108						
HER	50517.5335	-0.4828	0.0527	7.2236	7.2236	1.0000	7.2236	12.7922						
HER	50518.4988	0.2522	0.0239	7.3290	7.3290	1.0000	7.3290	-22.4244						
HER	50519.5038	-0.1027	0.0293	7.2223	7.2223	1.0000	7.2223	-8.8662						
HER	50520.4939	-0.7603	0.0026	7.2271	7.2271	1.0000	7.2271	14.8800						
HER	50521.4895	-0.2669	0.0014	7.2435	7.2435	1.0000	7.2435	0.7137						
HER	50523.5000	-0.3132	0.0182	7.1389	7.1389	1.0000	7.1389	1.2323						

Instr.	T [RJD]	$\mathrm{RV_n}$ [km/s]	$\sigma_{\mathrm{RV_n}}$ [km/s]	V [loc. con.]	R [loc. con.]	V/R	$\frac{1}{2}(V+R)$ [loc. con.]	BVS [km/s]	Group, T_{loc} [RJD]	Number of RV	OC_{RV} [RJD]	$\sigma_{OC_{\mathrm{RV}}}$ [RJD]	OC_{BVS} [RJD]	$\sigma_{OC_{\mathrm{BVS}}}$ [RJD]
HER	50524.5120	-0.8793	0.0007	7.2552	7.2552	1.0000	7.2552	26.8581		7	0.0307	0.0450	0.6475	0.031
HER	50525.5227	-0.0342	0.0246	7.2067	7.2067	1.0000	7.2067	-9.7273	30					
HER	50526.4968	0.0761	0.0016	7.1446	7.1446	1.0000	7.1446	-26.1471						
HER	50527.4968	-0.5616	0.0425	7.2059	7.2059	1.0000	7.2059	13.6304						
HER	50528.5681	-0.7504	0.1852	7.2468	7.2468	1.0000	7.2468	33.5220						
HER	50530.4992	-0.1988	0.0543	7.1907	7.1907	1.0000	7.1907	-3.3413						
HER	50531.4944	-0.9268	0.0850	7.2823	7.2823	1.0000	7.2823	32.7256	50526.6930					
HER	50532.4958	-0.3040	0.0047	7.2071	7.2071	1.0000	7.2071	-0.0017		6	0.0552	0.0450	0.7330	0.023
HER	50533.4945	0.3935	0.0515	7.2387	7.2387	1.0000	7.2387	-29.0841	31					
HER	50534.4909	-0.5553	0.0590	7.1434	7.1434	1.0000	7.1434	14.4969						
HER	50535.4835	-0.6396	0.0019	7.1683	7.1683	1.0000	7.1683	-62.1271						
HER	50536.4828	0.1075	0.0005	7.2145	7.2145	1.0000	7.2145	-17.8293						
HER	50537.4843	-0.0881	0.0239	7.1657	7.1657	1.0000	7.1657	-13.1968	50533.5780					
HER	50538.4843	-0.6819	0.0319	7.2246	7.2246	1.0000	7.2246	16.1114		6	0.0058	0.0470	0.7125	0.035
HER	50539.4831	-0.6708	0.0012	7.2114	7.2114	1.0000	7.2114	18.9722	32					
HER	50540.4819	0.1892	0.0805	7.2336	7.2336	1.0000	7.2336	-23.9649						
HER	50541.4821	-0.3283	0.0016	7.1908	7.1908	1.0000	7.1908	6.7364						
HER	50542.4848	-0.9008	0.1039	7.2701	7.2701	1.0000	7.2701	30.1328						
HER	50543.4804	-0.2518	0.0468	7.2156	7.2156	1.0000	7.2156	3.1719	50540.3890					
HER	50544.4719	0.2069	0.0813	7.2171	7.2171	1.0000	7.2171	-20.8301		5	-0.0575	0.0530	0.7501	0.061
HER	50545.4753	-0.3757	0.0290	7.2756	7.2756	1.0000	7.2756	1.9759	33					
HER	50546.4771	-0.9462	0.0005	7.2475	7.2475	1.0000	7.2475	19.9967						
HER	50547.4784	-0.2034	0.0012	7.1843	7.1843	1.0000	7.1843	-33.7527						
HER	50548.4812	0.4003	0.0139	7.3588	7.3588	1.0000	7.3588	-81.4500	50544.4420					
HER	50549.4805	-0.3437	0.1018	7.3214	7.3214	1.0000	7.3214	-50.4246		6	0.0000	0.0410	0.7086	0.042
HER	50550.4817	-0.4018	0.0005	7.3503	7.3503	1.0000	7.3503	-11.2666	34					
HER	50551.4765	0.4572	0.1200	7.3118	7.3118	1.0000	7.3118	-34.8066						
HER	50552.4836	0.1883	0.0017	7.3916	7.3916	1.0000	7.3916	-40.8617						
HER	50553.4668	-0.4846	0.0003	7.3752	7.3752	1.0000	7.3752	26.2462						
HER	50554.4718	0.0165	0.0508	7.3526	7.3526	1.0000	7.3526	-18.4384	50551.3600					
FER	51183.7316	0.7534	0.0006	6.9954	6.8324	1.0239	6.9139	-30.5225		13	-0.0509	0.0150	0.6704	0.012
FER	51183.8158	0.9297	0.0025	7.0024	6.7880	1.0316	6.8952	-36.5894	35					
FER	51184.6340	-0.7825	0.0023	6.9177	6.8736	1.0064	6.8957	38.4519						

Instr.	T [RJD]	RV_n [km/s]	σ_{RV_n} [km/s]	V [loc. con.]	R [loc. con.]	V/R	$\frac{1}{2}(V+R)$ [loc. con.]	BVS [km/s]	Group, T_{loc} [RJD]	Number of RV	OC_{RV} [RJD]	$\sigma_{OC_{RV}}$ [RJD]	OC_{BVS} [RJD]	$\sigma_{OC_{BVS}}$ [RJD]
FER	51184.7126	-0.6064	0.0004	7.0797	7.0349	1.0064	7.0573	29.6407						
FER	51184.8900	-0.0773	0.0023	6.9211	6.7973	1.0182	6.8592	4.6601						
FER	51185.5887	-0.0373	0.0163	7.0696	7.0361	1.0048	7.0529	-2.7211						
FER	51186.6480	1.0000	0.0008	6.8983	6.8502	1.0070	6.8743	-44.6316						
FER	51186.7699	0.3639	0.0008	6.9348	6.8511	1.0122	6.8930	-21.8995						
FER	51186.8488	0.2229	0.0004	6.9247	6.8351	1.0131	6.8799	-16.3803						
FER	51187.7761	0.3103	0.0002	6.9418	6.8726	1.0101	6.9072	-12.5290						
FER	51187.8703	0.6924	0.0001	6.9060	6.7943	1.0164	6.8501	-30.2017						
FER	51188.7487	-0.7699	0.0662	6.9701	6.9071	1.0091	6.9386	30.1858						
FER	51188.8545	-0.5627	0.0006	6.9777	6.8901	1.0127	6.9339	22.3159	51183.8440					
FER	51189.7220	-0.2359	0.0184	6.9596	6.9631	0.9995	6.9613	9.9045		13	-0.0364	0.0087	0.6459	0.0048
FER	51189.8008	-0.4196	0.0035	6.9232	6.9146	1.0012	6.9189	17.3494	36					
FER	51189.8644	-0.6287	0.0522	7.0247	6.9913	1.0048	7.0080	28.0896						
FER	51190.7394	0.9480	0.0146	7.0699	6.9579	1.0161	7.0139	-41.8683						
FER	51190.7523	0.8198	0.0553	7.0809	6.9592	1.0175	7.0200	-41.5275						
FER	51190.8255	0.7136	0.0518	7.1150	7.0121	1.0147	7.0636	-32.0528						
FER	51191.7258	-0.1623	0.0080	6.8910	6.8695	1.0031	6.8803	4.8437						
FER	51192.6030	-0.6750	0.0008	6.8896	6.8672	1.0033	6.8784	28.5213						
FER	51192.7203	-1.0000	0.0008	6.8898	6.8690	1.0030	6.8794	42.2536						
FER	51193.5598	0.6295	0.0476	6.9033	6.8181	1.0125	6.8607	-33.1725						
FER	51193.8344	-0.2862	0.0006	6.9114	6.8153	1.0141	6.8634	5.5310						
FER	51194.5120	0.0437	0.0008	6.9046	6.7426	1.0240	6.8236	-3.9614						
FER	51194.5159	0.0621	0.0012	6.9724	6.8164	1.0229	6.8944	-4.6913	51190.7189					
FER	51196.5140	-0.0120	0.0367	6.9241	6.8915	1.0047	6.9078	0.7699		6	-0.0758	0.0022	0.6005	0.015
FER	51196.7932	-0.8852	0.0008	7.0227	7.0006	1.0032	7.0117	42.5619	37					
FER	51197.5110	0.7664	0.0004	6.8686	6.8579	1.0016	6.8633	-34.3417						
FER	51198.5150	-0.2161	0.0008	6.9575	6.8983	1.0086	6.9279	4.8138						
FER	51199.5180	-0.7258	0.0917	6.9960	6.9877	1.0012	6.9919	33.8789						
FER	51200.5190	0.3563	0.0128	7.0770	7.0072	1.0100	7.0421	-18.6823	51197.5400					
HER	51302.4633	-0.5465	0.0801	6.8667	6.8667	1.0000	6.8667	29.7457						
FER	51554.5892	0.2181	0.0008	5.2229	5.2465	0.9955	5.2347	-1.8266		39	-0.0936	0.0068	0.5880	0.005
FER	51554.6229	0.0550	0.0016	5.1905	5.2661	0.9856	5.2283	2.1896						
FER	51554.6652	-0.2198	0.0169	5.1784	5.2387	0.9885	5.2086	9.3905						

Instr.	T [RJD]	$\mathrm{RV_n}$ [km/s]	$\sigma_{\mathrm{RV_n}}$ [km/s]	V [loc. con.]	R [loc. con.]	V/R	$\frac{1}{2}(V+R)$ [loc. con.]	BVS [km/s]	Group, T_{loc} [RJD]	Number of RV	OC_{RV} [RJD]	$\sigma_{OC_{\mathrm{RV}}}$ [RJD]	OC_{BVS} [RJD]	$\sigma_{OC_{\mathrm{BVS}}}$ [RJD]
FER	51554.7194	-0.4497	0.0004	5.2066	5.3052	0.9814	5.2559	20.5072						
FER	51554.7591	-0.6146	0.0004	5.2244	5.3185	0.9823	5.2715	27.6911						
FER	51554.7996	-0.7163	0.0006	5.2412	5.3264	0.9840	5.2838	28.7957						
FER	51554.8364	-0.8060	0.0111	5.2711	5.3598	0.9835	5.3155	36.8566						
FER	51554.8700	-0.8503	0.0002	5.1452	5.2213	0.9854	5.1833	37.2838						
FER	51555.5561	0.7404	0.0258	5.3480	5.3116	1.0069	5.3298	-24.9058						
FER	51555.5940	0.7017	0.1041	5.3316	5.3183	1.0025	5.3249	-25.3885						
FER	51555.6533	0.8507	0.0008	5.3619	5.3237	1.0072	5.3428	-29.1396						
FER	51555.6962	0.8439	0.0074	5.3214	5.3325	0.9979	5.3270	-30.5201						
FER	51555.7228	0.8076	0.0010	5.3355	5.3434	0.9985	5.3394	-30.6689						
FER	51555.7572	0.6942	0.0138	5.3357	5.3349	1.0001	5.3353	-26.9787						
FER	51555.7847	0.5975	0.0001	5.3255	5.3076	1.0034	5.3165	-23.8494						
FER	51555.8102	0.5344	0.0004	5.1273	5.1344	0.9986	5.1309	-21.2178						
FER	51555.8422	0.4155	0.0006	5.2118	5.2141	0.9996	5.2130	-16.7614						
FER	51555.8813	0.2882	0.0183	5.3172	5.3117	1.0010	5.3145	-12.4459						
FER	51556.5461	-0.3843	0.0012	5.3767	5.3486	1.0053	5.3627	16.5369						
FER	51556.5877	-0.2153	0.0010	5.3826	5.3562	1.0049	5.3694	9.0645						
FER	51556.6251	-0.0961	0.0010	5.4063	5.3651	1.0077	5.3857	2.5191						
FER	51556.6806	0.0668	0.0021	5.3925	5.3778	1.0027	5.3851	-2.6863						
FER	51556.7156	0.1856	0.0045	5.3801	5.3462	1.0063	5.3631	-11.0087						
FER	51556.8145	0.3885	0.0239	5.3896	5.3358	1.0101	5.3627	-17.8105						
FER	51556.8525	0.5272	0.0006	5.4036	5.3385	1.0122	5.3711	-21.9702						
FER	51556.8677	0.5868	0.0017	5.4066	5.3524	1.0101	5.3795	-24.9645						
FER	51556.8850	0.6235	0.0002	5.3985	5.3442	1.0102	5.3714	-25.8390						
FER	51557.5908	-0.8085	0.0099	5.3993	5.3996	0.9999	5.3995	32.8721						
FER	51557.6378	-0.8647	0.0085	5.3654	5.4039	0.9929	5.3847	35.7889						
FER	51557.7111	-0.8979	0.0167	5.3922	5.4338	0.9923	5.4130	34.0562						
FER	51557.7562	-0.6720	0.0085	5.3816	5.3969	0.9972	5.3893	33.6958						
FER	51557.8489	-0.7616	0.0006	5.4129	5.4127	1.0000	5.4128	27.1346						
FER	51558.5521	0.6070	0.0010	5.5131	5.4349	1.0144	5.4740	-20.8788						
FER	51558.5969	0.4231	0.0001	5.5261	5.4508	1.0138	5.4885	-15.4956						
FER	51558.6795	0.0685	0.0008	5.4785	5.4293	1.0091	5.4539	-7.6878						
FER	51558.7149	-0.0794	0.0109	5.4364	5.4098	1.0049	5.4231	-3.8509						

Instr.	T [RJD]	RV_n [km/s]	σ_{RV_n} [km/s]	V [loc. con.]	R [loc. con.]	V/R	$\frac{1}{2}(V+R)$ [loc. con.]	BVS [km/s]	Group, T_{loc} [RJD]	Number of RV	OC_{RV} [RJD]	$\sigma_{OC_{RV}}$ [RJD]	OC_{BVS} [RJD]	$\sigma_{OC_{BVS}}$ [RJD]
FER	51558.7653	-0.2687	0.0167	5.4715	5.4328	1.0071	5.4522	3.7522						
FER	51558.8407	-0.4699	0.0099	5.4501	5.4216	1.0053	5.4359	11.1245						
FER	51558.8687	-0.4713	0.0004	5.4589	5.4142	1.0083	5.4366	14.0634	51555.6385					
FER	51564.5632	-0.9889	0.0082	5.5759	5.5453	1.0055	5.5606	37.8707		26	-0.0421	0.0140	0.6489	0.011
FER	51564.7758	-0.6748	0.0006	5.5068	5.5131	0.9989	5.5100	28.2340	39					
FER	51564.8191	-0.5635	0.0068	5.5018	5.5098	0.9985	5.5058	22.2859						
FER	51564.8626	-0.4115	0.0008	5.4843	5.5072	0.9958	5.4958	17.5450						
FER	51565.5662	0.1000	0.1066	5.6005	5.4775	1.0225	5.5390	-10.6079						
FER	51565.8106	-0.7072	0.0307	5.5614	5.4572	1.0191	5.5093	24.3904						
FER	51565.8425	-0.8266	0.0002	5.5687	5.4539	1.0210	5.5113	30.7013						
FER	51565.8664	-0.8493	0.0008	5.5728	5.4393	1.0245	5.5061	30.2442						
FER	51566.5186	0.4627	0.0001	5.5700	5.4876	1.0150	5.5288	-25.5557						
FER	51566.7842	0.6012	0.0064	5.5692	5.5083	1.0111	5.5388	-24.5106						
FER	51566.8251	0.3753	0.0897	5.5738	5.5273	1.0084	5.5506	-24.5962						
FER	51566.8594	0.2977	0.0837	5.5575	5.5052	1.0095	5.5314	-18.3727						
FER	51567.7481	-0.0631	0.0006	5.4945	5.4655	1.0053	5.4800	1.1834						
FER	51567.7696	-0.0136	0.0012	5.5098	5.4732	1.0067	5.4915	-1.1962						
FER	51567.8215	0.1817	0.0041	5.5120	5.4731	1.0071	5.4926	-9.5267						
FER	51567.8391	0.2348	0.0008	5.5018	5.4427	1.0109	5.4723	-14.2610						
FER	51568.5188	-0.6765	0.0004	5.4553	5.3699	1.0159	5.4126	22.5221						
FER	51568.7742	-0.6142	0.0014	5.4535	5.3844	1.0128	5.4190	30.6453						
FER	51568.8134	-0.4151	0.0472	5.4339	5.3495	1.0158	5.3917	25.7239						
FER	51569.5158	0.7214	0.0685	5.4609	5.4170	1.0081	5.4390	-24.9432						
FER	51569.7830	-0.2654	0.0157	5.4973	5.4111	1.0159	5.4542	8.0986						
FER	51569.8220	-0.3429	0.0008	5.5374	5.4495	1.0161	5.4934	13.0754						
FER	51570.5101	0.1054	0.0283	5.3252	5.3009	1.0046	5.3131	-1.0567						
FER	51570.8073	0.9410	0.0008	5.3967	5.4111	0.9973	5.4039	-36.8968						
FER	51571.5147	-0.8311	0.0460	5.3363	5.4479	0.9795	5.3921	28.1827						
RET	51576.4297	0.4849	0.0002	4.4329	4.4329	1.0000	4.4329	-9.5233	51570.7830					
FER	52206.7664	-0.4637	0.0052	3.0999	3.1236	0.9924	3.1118	61.4239		132	-0.0472	0.0028	0.6152	0.0029
FER	52206.8361	-0.2942	0.0346	3.0847	3.1378	0.9831	3.1113	35.6614	40					
FER	52277.5490	0.7533	0.0413	3.3335	3.2653	1.0209	3.2994	-15.1155						
FER	52277.5690	0.5945	0.0024	3.4347	3.4154	1.0057	3.4250	-15.5409						

Instr.	T [RJD]	$\mathrm{RV_n}$ [km/s]	$\sigma_{\mathrm{RV_n}}$ [km/s]	V [loc. con.]	R [loc. con.]	V/R	$\frac{1}{2}(V+R)$ [loc. con.]	BVS [km/s]	Group, T_{loc} [RJD]	Number of RV	OC_{RV} [RJD]	$\sigma_{OC_{\mathrm{RV}}}$ [RJD]	OC_{BVS} [RJD]	$\sigma_{OC_{\mathrm{BVS}}}$ [RJD]
FER	52277.5846	0.5614	0.0006	3.2293	3.1759	1.0168	3.2026	-12.9439						
FER	52277.5952	0.5393	0.0007	3.4181	3.3341	1.0252	3.3761	-12.3169						
FER	52277.6029	0.5094	0.0238	3.4220	3.3454	1.0229	3.3837	-12.7063						
FER	52277.6081	0.4505	0.0024	3.4296	3.3506	1.0236	3.3901	-13.3908						
FER	52277.6146	0.4523	0.0114	3.4153	3.3444	1.0212	3.3799	-14.0975						
FER	52277.6198	0.4463	0.0006	3.4289	3.3506	1.0234	3.3898	-15.0099						
FER	52277.6250	0.4164	0.0098	3.4340	3.3548	1.0236	3.3944	-11.8766						
FER	52277.6302	0.3554	0.0182	3.4339	3.3444	1.0268	3.3892	-9.1966						
FER	52277.6365	0.3733	0.0157	3.4175	3.3364	1.0243	3.3770	-9.3309						
FER	52277.6417	0.3779	0.0004	3.4286	3.3525	1.0227	3.3906	-8.6052						
FER	52277.6471	0.3466	0.0157	3.4200	3.3377	1.0247	3.3789	-7.2337						
FER	52277.6524	0.2641	0.0035	3.4087	3.3260	1.0249	3.3674	-2.9269						
FER	52277.6570	0.2484	0.0059	3.4178	3.3403	1.0232	3.3791	0.1902						
FER	52277.6621	0.2552	0.0002	3.4145	3.3392	1.0226	3.3769	-7.4180						
FER	52277.6671	0.2051	0.0088	3.4208	3.3397	1.0243	3.3803	-8.9053						
FER	52277.6722	0.1618	0.0006	3.4089	3.3227	1.0259	3.3658	-5.1647						
FER	52277.6773	0.1628	0.0007	3.4079	3.3329	1.0225	3.3704	-4.8949						
FER	52277.6823	0.1475	0.0006	3.4125	3.3300	1.0248	3.3713	-4.9850						
FER	52277.6875	0.1473	0.0035	3.4049	3.3299	1.0225	3.3674	-2.8176						
FER	52277.6926	0.1320	0.0171	3.4170	3.3510	1.0197	3.3840	-3.0049						
FER	52277.6976	0.1123	0.0002	3.4155	3.3455	1.0209	3.3805	-0.8398						
FER	52277.7045	0.1272	0.0059	3.3999	3.3371	1.0188	3.3685	-4.1378						
FER	52277.7091	0.1016	0.0046	3.3790	3.3169	1.0187	3.3480	1.4976						
FER	52277.7142	-0.0323	0.0004	3.3840	3.3145	1.0210	3.3492	2.7828						
FER	52277.7296	-0.0006	0.0007	3.3986	3.3240	1.0224	3.3613	3.6732						
FER	52277.7347	0.0307	0.0007	3.3921	3.3296	1.0188	3.3609	8.5504						
FER	52277.7398	0.0099	0.0007	3.3728	3.3173	1.0167	3.3450	7.7883						
FER	52277.7449	0.0351	0.0002	3.3724	3.3142	1.0176	3.3433	-7.4360						
FER	52277.7500	-0.0351	0.0020	3.3964	3.3303	1.0198	3.3633	6.1033						
FER	52277.7600	-0.1009	0.0101	3.3836	3.3119	1.0216	3.3478	12.6510						
FER	52277.7646	-0.1029	0.0203	3.3702	3.2957	1.0226	3.3330	10.7364						
FER	52277.7696	-0.1580	0.0006	3.3580	3.2936	1.0196	3.3258	10.1187						
FER	52277.7747	-0.1488	0.0048	3.3518	3.3073	1.0135	3.3296	13.9207						

Instr.	T [RJD]	$\mathrm{RV_n}$ [km/s]	$\sigma_{\mathrm{RV_n}}$ [km/s]	V [loc. con.]	R [loc. con.]	V/R	$\frac{1}{2}(V+R)$ [loc. con.]	BVS [km/s]	Group, T_{loc} [RJD]	Number of RV	OC_{RV} [RJD]	$\sigma_{OC_{\mathrm{RV}}}$ [RJD]	OC_{BVS} [RJD]	$\sigma_{OC_{\mathrm{BVS}}}$ [RJD]
FER	52277.7798	-0.1587	0.0289	3.3662	3.3175	1.0147	3.3419	17.2052						
FER	52277.7848	-0.2215	0.0004	3.3655	3.3215	1.0132	3.3435	23.1664						
FER	52277.7900	-0.2724	0.0006	3.3582	3.3056	1.0159	3.3319	20.6650						
FER	52277.7951	-0.2812	0.0409	3.3554	3.2977	1.0175	3.3266	20.2004						
FER	52277.8001	-0.3339	0.0087	3.3459	3.2855	1.0184	3.3157	16.3836						
FER	52277.8052	-0.3096	0.0009	3.3528	3.3057	1.0142	3.3293	14.2766						
FER	52277.8108	-0.3223	0.0164	3.3542	3.3005	1.0163	3.3274	21.1959						
FER	52277.8154	-0.3630	0.0175	3.3607	3.3005	1.0182	3.3306	16.6173						
FER	52277.8205	-0.3759	0.0028	3.3313	3.2795	1.0158	3.3054	16.7773						
FER	52277.8256	-0.3914	0.0002	3.3464	3.2960	1.0153	3.3212	20.9527						
FER	52277.8307	-0.4037	0.0018	3.3528	3.2899	1.0191	3.3214	19.2474						
FER	52277.8358	-0.4348	0.0006	3.3413	3.2944	1.0142	3.3179	24.5781						
FER	52277.8408	-0.4510	0.0225	3.3378	3.2848	1.0161	3.3113	19.6802						
FER	52277.8459	-0.4822	0.0002	3.3444	3.2852	1.0180	3.3148	19.2603						
FER	52277.8510	-0.4923	0.0223	3.3465	3.2880	1.0178	3.3172	22.7829						
FER	52277.8560	-0.5047	0.0079	3.3376	3.2997	1.0115	3.3187	21.2989						
FER	52277.8627	-0.5555	0.0002	3.3324	3.2934	1.0118	3.3129	23.4374						
FER	52277.8730	-0.5695	0.0024	3.3334	3.2710	1.0191	3.3022	23.7128						
FER	52277.8782	-0.5671	0.0096	3.3317	3.2826	1.0150	3.3072	23.3767						
FER	52277.8846	-0.5647	0.0029	3.3259	3.2889	1.0112	3.3074	21.8311						
FER	52277.8903	-0.5710	0.0197	3.3202	3.2739	1.0141	3.2970	22.7624						
FER	52277.8957	-0.5754	0.0018	3.2101	3.1785	1.0099	3.1943	22.4631						
FER	52278.5359	0.3610	0.0273	3.4636	3.4636	1.0000	3.4636	-13.6907						
FER	52278.5417	0.3571	0.0004	3.4649	3.4675	0.9993	3.4662	-17.3546						
FER	52278.5463	0.3729	0.0175	3.4714	3.4728	0.9996	3.4721	-16.5853						
FER	52278.5514	0.3623	0.0162	3.4673	3.4755	0.9976	3.4714	-13.3999						
FER	52278.5565	0.3678	0.0088	3.4847	3.4847	1.0000	3.4847	-18.6784						
FER	52278.5616	0.3825	0.0066	3.4826	3.4943	0.9967	3.4885	-17.7486						
FER	52278.5666	0.3827	0.0011	3.4800	3.4945	0.9959	3.4873	-18.3937						
FER	52278.5717	0.4076	0.0015	3.4731	3.4917	0.9947	3.4824	-18.9552						
FER	52278.5768	0.4017	0.0004	3.4675	3.4858	0.9948	3.4767	-14.5363						
FER	52278.5818	0.4490	0.0197	3.4835	3.4933	0.9972	3.4884	-17.1587						
FER	52278.5869	0.4461	0.0007	3.4726	3.4868	0.9959	3.4797	-14.1800						

Instr.	T [RJD]	RV_n [km/s]	σ_{RV_n} [km/s]	V [loc. con.]	R [loc. con.]	V/R	$\frac{1}{2}(V+R)$ [loc. con.]	BVS [km/s]	Group, T_{loc} [RJD]	Number of RV	OC_{RV} [RJD]	$\sigma_{OC_{RV}}$ [RJD]	OC_{BVS} [RJD]	$\sigma_{OC_{BVS}}$ [RJD]
FER	52278.5927	0.4730	0.0120	3.4804	3.4935	0.9963	3.4870	-15.3380						
FER	52278.5973	0.5304	0.0260	3.4932	3.4968	0.9990	3.4950	-17.1741						
FER	52278.6025	0.5397	0.0006	3.4886	3.4986	0.9971	3.4936	-19.7719						
FER	52278.6075	0.5955	0.0092	3.4839	3.4945	0.9970	3.4892	-20.2114						
FER	52278.6127	0.5922	0.0011	3.4934	3.4982	0.9986	3.4958	-21.2566						
FER	52278.6178	0.6036	0.0149	3.4914	3.5092	0.9949	3.5003	-20.7324						
FER	52278.6229	0.6909	0.0494	3.4764	3.4837	0.9979	3.4801	-19.3021						
FER	52278.6280	0.5352	0.0402	3.4775	3.4886	0.9968	3.4831	-20.9110						
FER	52278.6331	0.7215	0.0508	3.4719	3.4914	0.9944	3.4817	-23.9272						
FER	52278.6381	0.6233	0.0002	3.4658	3.4925	0.9924	3.4792	-20.8558						
FER	52278.6432	0.6835	0.0707	3.4816	3.4921	0.9970	3.4869	-23.9994						
FER	52278.6483	0.7847	0.0650	3.4829	3.4934	0.9970	3.4882	-27.2262						
FER	52278.6534	0.7718	0.0689	3.4746	3.4848	0.9971	3.4797	-24.2797						
FER	52278.6585	0.7972	0.0648	3.4623	3.4692	0.9980	3.4658	-21.7817						
FER	52278.6636	0.8145	0.0658	3.4652	3.4851	0.9943	3.4752	-25.1749						
FER	52278.6687	0.8219	0.0698	3.4699	3.4935	0.9932	3.4817	-26.6598						
FER	52278.6738	0.8989	0.0004	3.4751	3.4762	0.9997	3.4757	-34.1297						
FER	52278.6789	0.8278	0.0744	3.4768	3.4882	0.9967	3.4825	-24.4287						
FER	52278.6841	0.8751	0.1013	3.4779	3.4892	0.9968	3.4836	-30.6688						
FER	52278.6892	0.8751	0.0927	3.4591	3.4746	0.9955	3.4669	-24.5068						
FER	52278.6945	0.8379	0.0847	3.4563	3.4687	0.9964	3.4625	-26.3690						
FER	52278.6986	0.8860	0.0595	3.4489	3.4546	0.9984	3.4518	-14.3086						
FER	52278.7031	0.8191	0.0547	3.4400	3.4514	0.9967	3.4457	-21.0163						
FER	52278.7077	0.8738	0.0801	3.4545	3.4653	0.9969	3.4599	-20.3388						
FER	52278.7122	0.8897	0.0694	3.4752	3.4752	1.0000	3.4752	-26.5931						
FER	52278.7167	0.9444	0.0041	3.4751	3.4751	1.0000	3.4751	-26.8996						
FER	52278.7213	0.9527	0.0002	3.4347	3.4598	0.9927	3.4473	-23.8258						
FER	52278.7259	0.9519	0.0225	3.4278	3.4468	0.9945	3.4373	-23.7841						
FER	52278.7303	0.9781	0.0002	3.4495	3.4534	0.9989	3.4515	-25.7572						
FER	52278.7349	0.9385	0.0085	3.4335	3.4433	0.9972	3.4384	-26.8482						
FER	52278.7394	0.9976	0.0002	3.4450	3.4421	1.0008	3.4436	-25.1442						
FER	52278.7484	0.9615	0.0586	3.4173	3.4236	0.9982	3.4204	-22.9181						
FER	52278.7529	0.9716	0.0007	3.4112	3.4167	0.9984	3.4140	-19.6933						

Instr.	T [RJD]	$\mathrm{RV_n}$ [km/s]	$\sigma_{\mathrm{RV_n}}$ [km/s]	V [loc. con.]	R [loc. con.]	V/R	$\frac{1}{2}(V+R)$ [loc. con.]	BVS [km/s]	Group, T_{loc} [RJD]	Number of RV	OC_{RV} [RJD]	$\sigma_{OC_{\mathrm{RV}}}$ [RJD]	OC_{BVS} [RJD]	$\sigma_{OC_{\mathrm{BVS}}}$ [RJD]
FER	52278.7575	0.9475	0.0142	3.4020	3.4190	0.9950	3.4105	-23.1227						
FER	52278.7620	0.9414	0.0350	3.4119	3.4236	0.9966	3.4178	-22.5757						
FER	52278.7665	0.9236	0.0006	3.4116	3.4203	0.9975	3.4160	-25.8128						
FER	52278.7710	0.9799	0.0260	3.4258	3.4258	1.0000	3.4258	-23.2799						
FER	52278.7755	1.0000	0.0160	3.4015	3.4327	0.9909	3.4171	-26.7922						
FER	52278.7801	0.9873	0.0252	3.3994	3.3978	1.0005	3.3986	-24.0258						
FER	52278.7896	0.9831	0.0199	3.4436	3.4436	1.0000	3.4436	-28.0660						
FER	52278.7942	0.9691	0.0006	3.4394	3.4160	1.0069	3.4277	-26.4470						
FER	52278.7993	0.9381	0.0006	3.4245	3.3988	1.0076	3.4117	-27.0703						
FER	52278.8043	0.9687	0.0302	3.4361	3.4133	1.0067	3.4247	-28.7721						
FER	52278.8094	0.8939	0.0387	3.4473	3.4220	1.0074	3.4347	-27.6173						
FER	52278.8145	0.9361	0.0002	3.4352	3.4077	1.0081	3.4215	-26.9258						
FER	52278.8196	0.9414	0.0103	3.4332	3.3995	1.0099	3.4164	-27.2523						
FER	52278.8299	0.9112	0.0013	3.4075	3.3782	1.0087	3.3929	-23.7950						
FER	52278.8349	0.9044	0.0274	3.4023	3.3755	1.0079	3.3889	-23.0882						
FER	52278.8400	0.9156	0.0278	3.4066	3.3807	1.0077	3.3937	-22.6297						
FER	52278.8451	0.9464	0.0076	3.4083	3.3765	1.0094	3.3924	-27.5688						
FER	52278.8502	0.9269	0.0004	3.4010	3.3686	1.0096	3.3848	-26.2612						
FER	52278.8553	0.7257	0.0001	3.4084	3.3720	1.0108	3.3902	-26.7036						
FER	52278.8604	0.7511	0.0004	3.3997	3.3723	1.0081	3.3860	-23.3654						
FER	52278.8654	0.6067	0.0007	3.3960	3.3747	1.0063	3.3854	-23.7111						
FER	52278.8706	0.7883	0.0004	3.3861	3.3604	1.0076	3.3732	-21.4379						
FER	52278.8757	0.7907	0.0035	3.3898	3.3576	1.0096	3.3737	-23.1093						
FER	52278.8807	0.7382	0.0009	3.3880	3.3568	1.0093	3.3724	-25.9200						
FER	52278.8858	0.7784	0.0350	3.3889	3.3629	1.0077	3.3759	-17.8377						
FER	52278.8925	0.7322	0.0006	3.3900	3.3636	1.0078	3.3768	-17.7435						
FER	52316.5160	-1.0000	0.0017	2.8773	2.9352	0.9803	2.9063	35.3214						
FER	52316.5222	-0.9886	0.0007	2.8695	2.9364	0.9772	2.9029	31.3856						
FER	52339.5096	-0.4017	0.0050	3.1430	3.2607	0.9639	3.2019	-1.9510	52278.7779					
SPM	52206.9934	-	-	2.9718	2.9718	1.0000	2.9718	-						
SPM	52206.9946	-	-	2.9872	2.9872	1.0000	2.9872	-						
SPM	52206.9956	-	-	2.9917	2.9917	1.0000	2.9917	-						